DISSERTATION

INVESTIGATING EMISSIONS AND EVOLUTION OF REACTIVE NITROGEN IN WESTERN U.S. WILDFIRE SMOKE PLUMES

Submitted by

Jakob Lindaas

Department of Atmospheric Science

In partial fulfillment of the requirements

For the Degree of Doctor of Philosophy

Colorado State University

Fort Collins, Colorado

Summer 2020

Doctoral Committee:

Advisor: Emily Fischer

A.R. Ravishankara
Jeffrey Collett, Jr.
Shantanu Jathar

ABSTRACT

INVESTIGATING EMISSIONS AND EVOLUTION OF REACTIVE NITROGEN IN WESTERN U.S. WILDFIRE SMOKE PLUMES

Wildfires are an important source of reactive nitrogen (N_r) to the atmosphere. Large wildfires are becoming more frequent in the western U.S. and smoke from large western U.S. wildfires is becoming a proportionately larger driver of poor air quality in certain U.S. regions. N_r in smoke contributes to the production of ozone (O_3), the formation of secondary inorganic and organic aerosol, and nitrogen deposition to downwind ecosystems, with attendant negative impacts on human and ecosystem health and important consequences for the earth's radiative budget. Smoke from wildfires is difficult to sample though, since it is hard to predict exactly where fires will start and which fires will grow larger across the western U.S. Scientific aircraft are able to sample smoke where and when it occurs, making them ideal platforms from which to gather observations of gases and particles in smoke. This dissertation presents results from three analyses investigating the emissions and evolution of reactive nitrogen in wildfire smoke using data from the Western wildfires Experiment on Cloud chemistry, Aerosol absorption, and Nitrogen (WE-CAN). The WE-CAN field intensive sampled fresh smoke from 23 identified large wildfires in the western U.S. during August and September 2018. Pseudo-Lagrangian ("lawnmower pattern") sampling was accomplished for about half of these fires, meaning that the plane was able to intercept the same smoke multiple times as it was transported downwind. Additionally, mixed and older smoke from indeterminate sources was sampled in the free troposphere as well as in the California Central Valley where it mixed with anthropogenic emissions. These data represent a large increase in the number of western wildfire smoke plumes intercepted by research aircraft in a systematic fashion.

First, I present a general overview of N_r emissions from 16 wildfires using a large cross section of the suite of chemical and physical measurements made onboard the National Science Foundation/National Center for Atmospheric Research (NSF/NCAR) C-130 aircraft. I find that reduced N compounds generally make up more than half of the total measured N_r (ΣN_r) (39 - 80%, median = 66%). This was not necessarily expected since we sampled plumes from fires at their most active time of day,

with assumed burning conditions that favored emission of oxidized forms of N_r. I observe evidence of rapid chemistry in the minutes between emission and the first sampling periods in all fires via significant abundances of peroxyacetic nitric anhydride (PAN) even in these youngest plume samples. I find evidence for the influence of both combustion conditions and fuel N content influencing the ratio of the sum of measured ammonia (NH_3) plus particulate ammonium (pNH_4) and the sum of oxidized nitrogen ($\Sigma NH_x/\Sigma NO_y$). Finally, estimated emission factors (EF) from these fires can be compared with previous literature for similar fuel types, with NH_3 EFs similar to or higher than previous lab and field observations, and NO_x EFs generally lower than previous estimates.

Next I explore the evolution of NH_3 in fresh and aged smoke. Focusing on 8 pseudo-Lagrangian sampled plumes, I observe e-folding loss timescales for NH_3 with respect to gas-particle partitioning on the order of minutes to hours, similar to previous estimates in fresh smoke. I find empirical evidence for the association of NH_3 and nitric acid (HNO_3) to form ammonium nitrate (NH_4NO_3), though not all plumes contain conditions favorable to NH_4NO_3 formation. Fresh, dense plumes injected at higher altitudes (and lower temperatures) are more likely to favor NH_4NO_3 formation, a conclusion consistent with previous model simulations in the literature. Measured organic acid ions also suggest the presence of NH_4-organic salts in the plumes sampled. Finally, I also use observations collected in medium and old aged smoke to find additional evidence for the formation of NH_4NO_3 in plumes injected higher in the atmosphere with larger oxidized N to NH_3 ratios.

Lastly, I investigate the production of PAN and peroxypropionic nitric anhydride (PPN) in the same set of pseudo-Lagrangian sampled plumes. Increases in dilution-corrected PAN and PPN mixing ratios in all plumes suggest that PAN and PPN are produced in all smoke plumes sampled, with the rate of increase similar to the handful of previous observations. I then use a simple observation-based model to determine the dominant precursors of PAN and PPN in fresh smoke plumes. From the model I infer that acetaldehyde is the dominant immediate PAN precursor in large western wildfire smoke plumes, with biacetyl also serving as an important precursor. To my knowledge this is the first time these conclusions have been drawn for smoke from an observational framework and it suggests that biacetyl should be included in models of smoke plume evolution. With respect to PPN, I find that propanal is an important immediate PPN precursor in fresh wildfire smoke. Unexpectedly, I also find that at least one other immediate PPN precursor is likely needed to explain PPN production, and suggest that this precursor may be ethylglyoxal. However, very few *in situ* measurements of ethylglyoxal exist to test this hypothesis.

ACKNOWLEDGMENTS

I would like to thank each of my committee members, Ravi, Shantanu, and Jeff, for giving me great feedback throughout this process and being supportive of this push to the finish line. I enjoyed taking your classes and fielding your questions in group meetings, and I feel very lucky to have been able to spend many of my scientific formative years in such a collaborative and supportive department and university.

A ginormous thank you to my Advisor, Emily, for being about the best advisor I could have hoped for. From setting me up on a trail run with Nick on my first visit to Fort Collins to connecting me with people you know in the policy world, the thoughtfulness and energy you put in to supporting me and the rest of your students is truly inspiring.

Thank you to my parents, who taught me to love the natural world from as early on as I can remember, and who always encouraged my sister and I to ask endless questions (even when it was probably annoying!). It's somewhat curious that I ended up studying atmospheric chemistry, as it seems to be a combination of sorts of my parents specialties in biology and physics. Moreover I've even spent several years now studying nitrogen, which was also the focus of my mom's dissertation! Though we have studied it in different media (me in the atmosphere, her in plants and soil), perhaps those early trips to greenhouses and field sites when I was baby made a subconscious impact on me...

My parents were far from the only ones who encouraged me to love learning. I should also thank my sister for the incredible worlds we imagined growing up together, and thank my grandparents, aunts and uncles, and cousins, who were always ready to explore the farm, beaches, or mountains with me.

A special thank you to my partner, Abby. Especially as my quarantine buddy and one woman dissertation-writing support structure, you have been, and continue to be, an incredible person and partner. I can't wait to explore a new city with you!

I would be remiss if I didn't thank the rest of the Fischer Group: Ilana, Jake, Steve, Jared, Zitely, Kate, and Julieta. It has been such a joy to share offices and the lab with you all, and I've had much fun and learned so much from you all. A particular thank you to Ilana for taking me under your wing and teaching me the ways of aircraft instrumentation!

I was fortunate enough to be a part of two large field projects during the past several years. Thank you to all the scientists, pilots, and crew of both the WE-CAN and FIREX-AQ projects for being great

collaborative teams and teaching me so much. Thank you as well to the agencies (NSF, NOAA, and NASA) who funded these projects and my time at Colorado State. NSF, NOAA, and NASA all play such a critical role in driving earth sciences forward, and I look forward to working with all the wonderful people at each agency in the future, whether as a researcher or from a science policy perspective.

I was also fortunate to get pulled into this field during undergrad by an amazing group of people and scientists. Thank you to Archana, Leland, Bill, Roisin, Steve, and the rest of the Wofsy Group for encouraging me to apply for that summer research experience, and for taking me on as a senior thesis project and then again as a research assistant for 2 more years. Atmospheric Chemistry is a pretty neat field, and the fun I had working and learning with and from you all has clearly led me to where I am today.

Lastly, I mentioned it above, but the Faculty, Staff, and Students in the CSU Atmospheric Science Department make it an amazing place to work and learn in. Thank you in particular to Sarah for all that you do to keep us students sane and on track! It's been so much fun getting to explore Fort Collins and Colorado with many of you! The camaraderie is always contagious and the kindness and care for one another is inspiring.

TABLE OF CONTENTS

CHAPTER 1

INTRODUCTION

1.1 INTRODUCTION TO WESTERN U.S. WILDFIRES

The complex mixture of gases and particles in wildfire smoke has long been recognized as an important component of the earth system (*e.g.* Andreae et al. 1988). Biomass burning releases significant amounts of greenhouse gases (Seiler and Crutzen 1980; Urbanski 2014) as well as other trace gases that impact atmospheric chemistry on local to global scales (Boubel et al. 1969; Darley et al. 1966; Crutzen et al. 1979; Akagi et al. 2011). Smoke aerosol has important direct and indirect effects on the earth's radiative budget (Penner et al. 1992; Christopher et al. 2000) and contributes to $PM_{2.5}$ (particulate matter with diameters less than 2.5 microns), a key air pollutant harmful to human health (*e.g.* Correia et al. 2013). Recently, we are also learning much more about the gaseous hazardous air pollutants in smoke (O'Dell et al. submitted). Lastly, smoke from biomass burning has important ecosystem and biogeochemical cycling impacts through the redistribution of key elements such as nitrogen and potassium (Crutzen and Andreae 1990; Kanakidou et al. 2018).

Our understanding of these diverse impacts from wildfire smoke has expanded dramatically in the past several decades (Sokolik et al. 2019). At the same time humans continue to perturb the drivers of wildfires through land use modification and climate change (Bowman et al. 2009; Marlon et al. 2012; Keywood et al. 2013). Large wildfires are becoming more frequent in the western U.S. (Westerling 2016) and smoke from large western U.S. wildfires can impact atmospheric composition on a continental scale (Jaffe et al. 2008; Park et al. 2003, 2007). Smoke is becoming a proportionately larger driver of poor air quality in certain U.S. regions in the context of decreasing anthropogenic emissions from many sectors (McClure and Jaffe 2018; O'Dell et al. 2019), ongoing climate change (Schoennagel et al. 2017; Williams et al. 2019), and fire management practices (Kolden 2019; Schultz and Moseley 2019).

Smoke is complex and difficult to sample. A large wildfire contains a range of burning conditions at any given time. One researcher has described large wildfires as "1000 small fires all burning differently" (Jack Dibb, personal communication). Since wildfires are a natural phenomena that is difficult to plan for, atmospheric researchers have used a combination of laboratory studies (*e.g.* McMeeking et al. 2009), opportunistic field sampling (*e.g.* Liu et al. 2016), planned aircraft campaigns (*e.g.* Wofsy et al. 1992; Yokelson et al. 2009), prescribed burn sampling (*e.g.* Akagi et al. 2012b), and satellite analyses

(*e.g.* Adams et al. 2019) to study the composition and evolution of smoke. In their recent review, Sokolik et al. (2019) describe two main goals for the study of smoke emissions, evolution and atmospheric impacts: "[T]o clarify chemistry and transport to improve air quality and health and to accurately integrate and model feedback within climatic systems." This dissertation aims to use a novel aircraft dataset to explore key questions related to these goals by investigating the emissions and evolution of reactive nitrogen in wildfire smoke.

1.2 Introduction to the Western wildfires Experiment on Cloud chemistry, Aerosol absorption, and Nitrogen (WE-CAN)

The WE-CAN project deployed the National Science Foundation/National Center for Atmospheric Research (NSF/NCAR) C-130 research aircraft in summer 2018 (22 July – 13 September) to sample wildfire smoke during its first day of atmospheric evolution (`https://www.eol.ucar.edu/field_projects/we-can`). All data are available in the WE-CAN data archive (`https://data.eol.ucar.edu/master_lists/generated/we-can/`). The flight plans and aircraft payload were specifically designed to answer questions related to reactive nitrogen (N_r) in wildfire smoke plumes, as well as questions related to absorbing aerosols, cloud activation and other chemical processes in wildfire plumes. Approximately two thirds of the flight hours (134 total) were focused on sampling emissions and aging of daytime wildfire smoke. The other third of flight hours were devoted to sampling smoke-cloud mixtures. The goal of the emission and aging flight hours was to fly as close to its source as possible given safety and logistical constraints and to systematically characterize the variability in emissions for a wide set of fires burning in different ecosystems under varying environmental conditions. Flight patterns were largely consistent across fires sampled during WE-CAN, with additional sampling added to specific fires. Upon approaching a major wildfire, the aircraft first sampled upwind air to characterize upwind conditions. The aircraft then crossed the smoke plume downwind of the fire as close to the fire as possible. This transect was typically done at a single altitude, but was possible at several altitudes for a subset of fires. From here, the aircraft sampled the smoke through multiple downwind plume transects in order to characterize smoke evolution in a pseudo-Lagrangian fashion.

Pseudo-Lagrangian sampling was attempted for 12 fires during WE-CAN, but WE-CAN sampled smoke that could be traced to 23 different wildfires located in 8 different western U.S. states. The summer 2018 U.S. wildfire season was very active, the sixth-largest on record in terms of burn area. Within the U.S. 58,083 wildfires burned 8.8 million acres (Hoover and Hanson 2019). Thus the aircraft was

able to opportunistically sample many fresh smoke plumes en route to or returning from the target wildfires. The WE-CAN flights spanned the period of the day with the greatest wildfire activity and the easiest aircraft access. During the majority of the campaign, when the aircraft was based in Boise, ID, the flights typically took off between 12:00 and 14:00 Local Time (Mountain Time = UTC - 6 hours), and landed between 19:00 and 21:00 Local Time. WE-CAN sampled a mixture of fire sizes, ignition types, and fuel types. The final burn area of fires sampled during WE-CAN ranged from less than 5,000 acres (*e.g.*, Wigwam Fire) to more than 450,000 acres (Mendocino Complex Fire). Each fire was associated with the Fuel Characteristic Classification System (FCCS) fuelbeds that burned during the specific time the NSF/NCAR C-130 aircraft was sampling the smoke (Ottmar et al. 2007). The fires sampled during WE-CAN (red triangles), along with the flight tracks (grey lines), are shown in Figure 1.1.

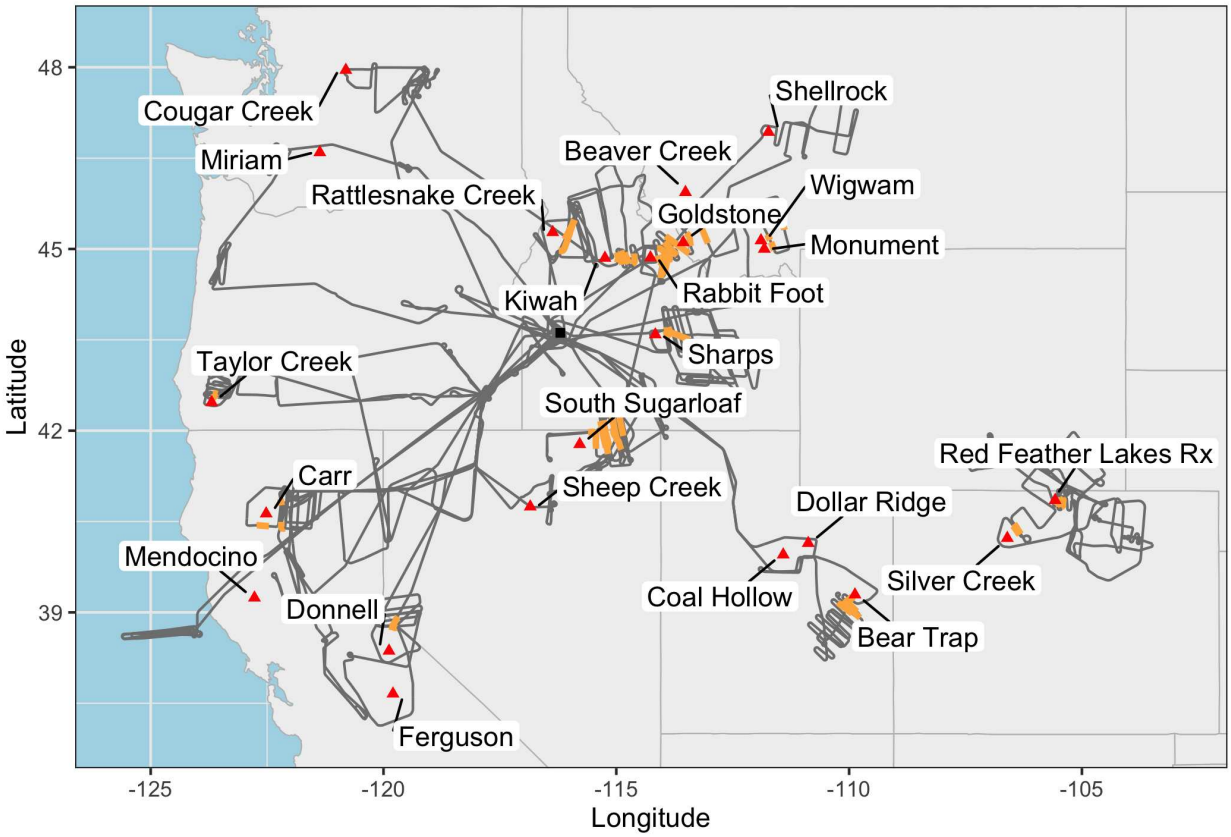

FIG. 1.1. Flight tracks during WE-CAN (grey) with fires sampled (red triangles and labels) and plume segments used in the Chapter 3 analysis highlighted in orange. The black square denotes our base of operations in Boise, ID.

1.3 INTRODUCTION TO REACTIVE NITROGEN IN SMOKE

The emissions and evolution of reactive nitrogen in wildfire smoke will be explored in the remainder of this dissertation. Reactive nitrogen (N_r = all N-compounds except N_2O and N_2) within biomass burning smoke contributes to the production of ozone (O_3) (Jaffe and Wigder 2012), the formation of secondary inorganic (Trentmann et al. 2005) and organic aerosol (Lin et al. 2016), and nitrogen (N) deposition to downwind ecosystems (Chen et al. 2014; Prenni et al. 2014). The form of N_r within smoke ranges from fully reduced (NH_3) to highly oxidized (nitric acid; HNO_3). Roughly half of the N emitted by biomass burning is thought to be molecular nitrogen (N_2), an important denitrification process in ecosystems (Kuhlbusch et al. 1991; Lobert et al. 1990). Small molecules such as NH_3, nitric oxide (NO), and isocyanic acid (HNCO) comprise the majority of the remaining N emissions, with smaller contributions from hydrogen cyanide (HCN), nitrous acid (HONO), acetonitrile (CH_3CN), and a wide variety of other N-containing volatile organic compounds (NVOCs, including amine, amide, nitrile, nitro, isocyanate, and N-heterocyclic compounds) (*e.g.* Coggon et al. 2016).

Fixed N in burning biomass is initially pyrolyzed as a handful of small N-containing compounds: NH_3, HCN, HNCO, and CH_3CN and minor amounts of other NVOCs (Glarborg et al. 2018; Lobert and Warnatz 1993; Roberts et al. 2020). Immediately following this decomposition of fuel N and subsequent volatilization, and still within the flame, some of these species are quickly oxidized by rapid radical chemistry to form the remainder of the species we consider to be primarily emitted by fires: N_2, NO, NO_2, N_2O, and HONO (Hansson et al. 2004; Ren and Zhao 2012, 2013a,b; Scharko et al. 2019; Sekimoto et al. 2018). Lab and field studies have found strong relationships between the observed forms of N_r emissions and the dominant combustion conditions, with more NO_x and HONO emissions during flaming combustion and more NH_3 and HCN emissions during smoldering combustion (Burling et al. 2010; Goode et al. 1999; McMeeking et al. 2009; Roberts et al. 2010; Yokelson et al. 1996, 1997). Flaming combustion is generally associated with higher burn temperatures and greater oxidation of initially pyrolyzed small N-compounds, with smoldering combustion characterized by lower burn temperatures and lesser oxidation. Fuel moisture and fuel geometry (or arrangement) can affect the combustion characteristics and forms and relative amount of N_r (Chen et al. 2010; McAllister 2019). Fuel N content has also been shown to be an important determinant of how much N_r is emitted, with higher fuel N generally corresponding to great N_r emissions (Burling et al. 2010; Coggon et al. 2016; Kuhlbusch et al. 1991; Lobert et al. 1990; Stockwell et al. 2014). We note that all N_r emitted by natural convection

biomass burning is derived from fuel N, as these fires do not burn hot enough to form thermal NO_x from the reaction of N_2 and O_2 (Roberts et al. 2020).

After emission, N_r compounds in smoke may undergo further oxidation or partition into existing aerosol (*e.g.* Akagi et al. 2012a). This chemistry will depend on the presence of oxidants such as OH, O_3, and the nitrate radical (NO_3), as well as gas-phase acids and bases and particulate inorganic and organic ions. The products of this N_r evolution will commonly consist of HNO_3, organic nitrates (ONs), nitro-aromatics, acyl peroxy nitrates (APNs), particulate nitrate (pNO_3), and particulate ammonium (pNH_4) (*e.g.* Alvarado et al. 2010; Liu et al. 2016). These products are important to the transport of NO_x to other, often remote, regions of the atmosphere (APNs: *e.g.* Singh et al. 1992), the termination of O_3 formation reactions (HNO_3, ONs, pNO_3: *e.g.* Alvarado et al. 2010), the formation of secondary aerosol (pNO_3, pNH_4, nitro-aromatics: *e.g.* Trentmann et al. 2005), and the deposition of reactive N to ecosystems downwind of active fires (*e.g.* Prenni et al. 2014). Atmospheric chemistry models are needed to estimate the integrated impact of wildfire smoke on the atmosphere and land surface (*e.g.* Paulot et al. 2017). However, our estimates of N_r emissions are generally underconstrained and our understanding of key N_r evolution processes is incomplete.

1.4 Overview of dissertation chapters and goals

This dissertation advances our understanding of the emissions and evolution of reactive N in wildfire smoke. My work reflects a dramatic expansion in the number of western U.S. wildfires for which N_r emissions and evolution have been quantified. This dataset also represents one of the most complete sets of *in situ* N_r species measured in smoke to date, with nearly all of the key species relevant to exploring the relative forms and distribution of reduced and oxidized N emissions, the evolution of gas-phase NH_3, and the formation mechanisms of peroxyacetic nitric anhydride (PAN) and peroxypropionic nitric anhydride (PPN) present. In the following Chapters, I have attempted to gain insight into these processes via observationally-constrained analyses. Chapter 2 describes common measurements and methods that are used across each of the analyses.

Chapter 3 is adapted from a manuscript under review for *JGR-Atmospheres*. Chapter 3 examines the drivers of the forms and distribution of N_r emissions from large (> 1000 acres) western U.S. wildfires. My analysis explores what factors control the ratio of reduced to oxidized N_r emissions, and how estimated WE-CAN emission factors compare with previous lab and field estimates. The insight into

N_r emissions from Chapter 3 sets the stage and context for the explorations of NH_3 and PAN evolution that follow in Chapters 4 and 5.

Chapter 4 is adapted from a manuscript in preparation for *JGR-Atmospheres*. Chapter 4 explores the evolution of NH_3 in the smoke sampled by WE-CAN. I provide a comprehensive observational overview of the timescales of NH_3 evolution in pseudo-Lagrangian sampled smoke plumes, and investigate the empirical evidence for the formation of NH_4NO_3 and other forms of pNH_4.

Chapter 5 is adapted from a manuscript also in preparation for *JGR-Atmospheres*. Chapter 5 provides a specific look at PAN and PPN evolution in WE-CAN plumes, and investigates the importance of various precursors using a simple observationally-constrained model.

Lastly, Chapter 6 summarizes the findings presented in the previous chapters and explores future research pathways.

CHAPTER 2

MEASUREMENTS AND COMMON METHODS

2.1 MEASUREMENT DETAILS

WE-CAN measurements include a large suite of gas-phase and particle-phase reactive N species. Instruments in the payload responsible for measured N_r species and the key carbon species used in the analysis include: the NCAR 2-channel and single-channel chemiluminescence instruments measuring NO, NO_2, and O_3; the Colorado State University (CSU) QC-TILDAS measured gas-phase NH_3; the University of Washington (UW) I-CIMS measuring HCN, HNCO, HNO_3, HONO, and gas-phase organic nitrates; the NCAR PAN-CIMS measuring PAN and PPN; the University of Montana (UM) PTR-ToF-MS measuring acetonitrile (CH_3CN) and a selection of NVOCs (amines: ethenamine, propene amine, trimethylamine, butene amine; amides: formamide and acetamide; nitriles: propane nitrile, hydroxy acetonitrile, cyanoallene isomers, pentanenitriles, 4-methylpentanenitrile, benzonitrile, furancarbonitriles; nitro species: nitromethane, nitropropanes, nitroethane, nitroethene, nitrotoluene; and N-heterocyclics: pyrrole, dihydropyrrole, pyridine, methyl pyrrole isomers, ethylnylpyrrol, methyl pyridines, vinylpyridine, dihydroxy pyridine, nitrofuran); the CSU AMS measuring $p\mathrm{NH_4}$ and $p\mathrm{NO_3}$; the CSU PILS measuring inorganic NH_4 and NO_3 ions; and the NCAR AWAS which was used to collect whole air samples and a comprehensive suite of VOCs were measured at CSU, which included measurements of seven alkyl nitrates (methyl- to pentyl-). To our knowledge, there are no published examples of *in situ* wildfire plume observations where most of the key species relevant to determining the ratio between oxidized and reduced N, or the rapid conversion of NO_x to its oxidation products (*e.g.* PANs, organic nitrates, HNO_3) have been simultaneously quantified. This is a major strength of the WE-CAN dataset. However, the WE-CAN payload did not include a measurement of total oxidized N (NO_y) or total N_r, or speciated gas-phase and particulate organic nitrates. Roberts et al. (2020) used a similar set of gas-phase measurements in the lab and compared the sum N_r (without particulate N) to a measurement of total N_r. They estimated that the sum of individual gas-phase N_r compounds captured between 75-95% of the total N_r emitted, with the remainder expected to be particle bound N). In lieu of a total NO_y or N_r measurement, in our analysis we will use the sum of measured species, ΣNO_y (= $NO_x + p\mathrm{NO_3}$ + PANs + HNO_3 + HONO + ONs) and ΣN_r (= sum of all measured N).

[2]Adapted from two manuscripts, one in review, and another in preparation, both for *JGR Atmospheres*, June 2020

We also use data from several other instruments measured other chemical species or physical atmospheric properties. These include the NCAR QC-TILDAS measuring CO and nitrous oxide (N_2O); the NCAR Picarro measuring CO_2, CO, and CH_4; the NCAR Trace Organic Gas Analyser (TOGA) measuring VOCs; and the HIAPER Atmospheric Radiation Package (HARP) measuring actinic flux for the estimation of photolysis rate coefficients.

In the following sections we describe the instruments listed above. My specific role during WECAN was to help make the NH_3 measurement, along with Dr. Ilana Pollack. I also assisted in operating the PAN-CIMS on several flights and helped run calibrations and zeros for the NCAR QC-TILDAS and Picarro instruments in flight.

2.1.1 NCAR NO_x/O_3

NO and NO_2 were measured with the NCAR 2-channel chemiluminescence instrument; the NCAR single-channel chemiluminescence instrument for measuring O_3 was integrated with this system. The instruments shared an inlet, pumping system, data acquisition system, and power supplies. NO is measured via its chemiluminescent reaction with a flow of reagent O_3, generated on board Ridley and Grahek (1990). Photons from excited NO_2 are counted with a dry-ice-cooled photomultiplier tube to provide the primary signal. NO_2 is measured in a separate sample flow as an increase in NO following photolysis of NO_2 by "400 nm" light-emitting diodes (LEDs, model LZP-00UA00, bin code U5, with actual peak wavelengths of 390-395 nm and a spectral width of ~10 nm). Interference from HONO on the NO_2 measurement is expected to be small given the factor of 40-150 larger NO_2 cross sections in the LED wavelength range. O_3 is measured similarly via the reaction of ambient O_3 with a flow of reagent NO from an on-board gas cylinder (Ridley et al. 1992). The NO and NO_2 channels are periodically calibrated in flight using two flows from a compressed gas calibration standard of NO in N_2, one of which has O_3 added in order to convert NO to NO_2 for the calibration of the NO_2 conversion efficiency by the LEDs. The O_3 channel was calibrated periodically on non-flight days using a Thermo Scientific Primary Standard, Model 49i, factory calibrated in April 2018. Data are reported at 1 Hz, though the time response of the NO_x channels is somewhat slower than this. At mixing ratios above 1 ppbv the uncertainties are 6% for NO, 12% for NO_2, and 5% for O_3 and the upper bound on mixing ratio dependant precision is 100 pptv for NO, 140 pptv for NO_2, and 0.2 ppbv for O_3.

2.1.2 CSU NH_3

NH_3 was measured using a compact, single-channel, closed-path quantum-cascade tunable infrared laser direct absorption spectrometer (QC-TILDAS). In order to improve accuracy and time response, the commercially available instrument (from Aerodyne Research Inc.) was augmented with 1) a heated PFA aircraft inlet, 2) an inertial inlet that separates particles with aerodynamic diameters greater than 300 nm from the sample stream, 3) a continuous flow of passivant (1H,1H-perflurooctylamine: a stronger base than NH_3) which coats inlet surfaces and improves NH_3 transmission, and 4) a custom-designed, vibrationally isolated plate. This system is described in detail by Pollack et al. (2019) and descriptions of the commercially available QC-TILDAS have been previously published (McManus et al. 1995, 2007, 2010; Zahniser et al. 1995). During WE-CAN the NH_3 QC-TILDAS collected NH_3 mixing ratio measurements at 10Hz and were averaged to 1Hz, with a 3σ detection limit of ±200 pptv, an uncertainty of ±12% of the measured mixing ratio plus the detection limit, and a response time of ∼1 second corresponding to 90% signal recovery.

2.1.3 UW I-CIMS

Gas-phase HCN, HNCO, HNO_3, HONO, and gas-phase organic nitrates were sampled by the UW high-resolution chemical ionization time-of-flight mass spectrometer using iodide-adduct ionization (I^--CIMS; Lee et al. 2014, 2018). Ambient air was sampled at 20 lpm through a straight ∼50 cm length of 0.75 in OD PTFE Teflon tubing. The air was then subsampled at 2 slpm into a custom ion-molecule reaction (IMR) inlet designed to minimize the influence of walls on the measurements while characterizing the remaining wall effects, as described in Palm et al. (2019). The mass spectrometer simultaneously measured hundreds of molecular formulas, including inorganic and oxidized organic molecules, at 2 Hz time resolution and with a mass resolving power of approximately 5000. Water vapor was continuously added to the IMR in order to maintain relatively constant water vapor concentrations and minimize the effects of water vapor dependence on the ionization process. The IMR background signal was measured for 6 s each 1 min by overflowing the IMR with clean N_2 gas. The background signal from the inlet tubing was also measured for 15 s every 15 mins. HCN, HNCO, HNO_3, and HONO were each calibrated in the laboratory before and/or after WE-CAN deployment. Calibration factors and details specific to the WE-CAN deployment can be found in Peng et al. (2020), but in general are similar to those reported previously (Lee et al. 2014, 2018). For these species, accuracy is estimated to be 30% and detection limits, propagated from the standard deviation of one second data, are 112 pptv for HCN, 70.4 pptv for HNCO, 20.5 pptv for HNO_3 and 13.5 pptv for HONO. Gas-phase multifunctional

organic nitrates (ONs) are also detected by the I-CIMS, with ONs defined as any species containing N, two or more carbon atoms, and three or more oxygen atoms. Individual ONs and isomers cannot be separated or directly calibrated. While the I-CIMS does not provide specific information on molecular structure or functional groups, the nature of iodide-adduct ionization means the detected compounds are most likely multifunctional organic nitrates, peroxy nitrates, and/or peroxyacyl nitrates (Lee et al. 2016). Multifunctional oxidized amines are also theoretically possible but are not expected. Thus for simplicity, we refer to this group of measured compounds as gas phase ONs. Therefore, an estimate of ΣONs is made by assigning a calibration factor of 5 normalized counts per second (ncps) per pptv of analyte for all organic nitrates detected and summing over all ONs. This calibration factor is an estimate of the average sensitivity for this group of compounds, and is based on the range of sensitivities of calibrated gases during WE-CAN. This ΣONs calculation has large uncertainties, estimated here as a factor of 2 on the absolute mixing ratio (200% error). Gas-phase nitrophenolic species are not included in the ΣONs, but are a small fraction (< 1%) of total gas-phase ON mass. Most nitrophenolic compounds are expected to be in the particle phase and would therefore be detected by the AMS. To avoid double-counting PAN and PPN and since the PAN-CIMS is more sensitive and precise, we removed their corresponding molecular formulas from the I-CIMS ΣONs calculation.

2.1.4 NCAR PAN-CIMS

PAN and PPN were measured with a thermal dissociation chemical ionization mass spectrometer (CIMS) (Slusher et al. 2004; Zheng et al. 2011). PANs in ambient air are decomposed in the instrument inlet at 150°C into NO_2 and the parent peroxy acyl radicals. The latter react with Iodine ions produced from CF_3I in a static ionizer cartridge in the flow tube controlled to a pressure of 20 torr. The produced acylate ions are then detected in a quadrupole mass spectrometer. Calibration is performed continuously by adding a known amount of isotopically labeled C^{13}-PAN to the aircraft inlet. Accuracy is 12% or 25 pptv (whichever is greater) for PAN and PPN and precision is 20 pptv on average across the flights.

2.1.5 UM PTR-ToF-MS

VOC measurements were made using a proton-transfer-reaction time-of-flight mass spectrometer (PTR-ToF-MS 4000, Ionicon Analytik, Innsbruck, Austria). In brief, ambient air is continuously pumped through the PTR-ToF-MS drift-tube, where VOCs with a proton affinity higher than that of water (>165.2 kcal/mol) are ionized via proton-transfer reaction with H_3O^+ ions, then subsequently separated and detected by a time-of-flight mass spectrometer (with a mass resolving power up to 4000). During WE-CAN, PTR-ToF-MS measured ion m/z from 15-400 at 2 or 5 Hz frequency. Ambient air was

drawn to the instrument at 10-15 lpm via ~3 m of 1/4" O.D. PFA tubing maintained at ~55°C, and then subsampled by the instrument though ~100 cm of 1/16" O.D PEEK tubing maintained at 60°C. The residence time from outside of the aircraft to the drift-tube is less than 2 seconds. Instrument background was checked approximately every hour during a flight by measuring VOC-free air generated from a heated catalytic converter (375°C, platinum bead, 1% wt. Pt, Sigma Aldrich). Calibrations were typically performed 3 times per flight by the dynamic dilution of certified gas standard mixtures containing 25 distinct VOCs (Apel-Riemer Environmental Inc., Miami, FL). For ions not directly calibrated by the gas standard, sensitivities were estimated using the method described by Sekimoto et al. (2017). Measurement uncertainties for the 25 directly calibrated VOCs are ~15%, and for the rest are estimated to be better than 50% (Wade Permar, personal communication). Detection limits are species specific and generally range 50-250 pptv for directly calibrated VOCs (Yuan et al. 2017).

2.1.6 CSU AMS

Chemically-resolved submicron non-refractory aerosol mass was measured using a high-resolution time-of-flight aerosol mass spectrometer (HR-TOF-AMS; Aerodyne, Inc.) (DeCarlo et al. 2006) equipped with a pressure controlled inlet (Bahreini et al. 2008). Operation of this instrument and data processing during WE-CAN is described in Garofalo et al. (2019). Briefly, in the HR-TOF-AMS, particles are focused through an aerodynamic lens to a tungsten vaporizer (standard vaporizer) at 600°C; the resulting gases are ionized by 70 eV electron ionization, and subsequently extracted and analyzed by time-of-flight mass spectrometry. During WE-CAN, the HR-TOF-AMS was operated in standard mass spectrometry mode with 5 s time resolution (2.5 s open and 2.5 s closed) in V-mode (m/δm ~2100). Accuracy (2σ) for the HR-AMS is estimated to be 35% for inorganic species (Bahreini et al. 2009). At low concentrations, precision is the same as the detection limit - better than 0.1 ug sm^{-3} for pNO_3 and pNH_4 at 5s time resolution. At high concentrations, precision is 0.5-3% of pNO_3 and pNH_4 mass. We note that due to the nature of electron ionization, organic nitrates, if present, will fragment to NO_x^+ ions in the AMS, and thus may contribute to reported pNO_3 (Farmer et al. 2010). Determination of the relative contribution of organic nitrates to the pNO_3 signal for this dataset is currently underway. We use the notation pNO_3 here to indicate that both inorganic and organic N-containing species may contribute to this signal. Similarly, reduced N-containing organics such as amines and amides may contribute to the observed pNH_4 signal and the reported pNH_4 should be considered an upper bound for sub-micron particulate ammonium (NH_4^+).

2.1.7 NCAR $CO/N_2O/CO_2/CH_4$

CO and N_2O were measured with a commercial Mini-TILDAS tunable diode laser infrared absorption spectrometer (Aerodyne Research) (Lebegue et al. 2016). To optimize measurement accuracy, the spectrometer optical bench was continuously purged with synthetic zero grade air from which CO had been scrubbed to contain less than 1 ppbv. N_2O was quantified in the purge gas and typically found to contain less than 0.3 ppbv. This constant N_2O purge gas concentration at cabin pressure was included in spectral fit calculations to better reproduce spectral background. The WE-CAN data set has a precision of 0.1 ppbv with a 2s temporal resolution and an accuracy of ±0.6 ppbv for CO and ±1 ppbv for N_2O. A Picarro G-2401-m analyzer was used for the measurement of CO_2 and CH_4, which also provided an additional, but lower precision, measurement of CO. Stated 1σ precision for the Picarro is 30 ppbv, 20 ppbv, and 2 ppbv for CO, CO_2 and CH_4, respectively. Accuracy for the Picarro CO_2 measurements is 0.05 ppmv. Calibration was done by overflowing the inlet with a known mixture of the measured gases in ultrazero air at regular intervals during flight.

2.1.8 CSU Particle-into-Liquid Sampler (PILS)

Two minute integrated inorganic particulate NO_3^- and NH_4^+ were determined using a Particle-into-Liquid Sampler (PILS) with fraction collector system. The operation of the PILS system and off-line analysis of the liquid samples by ion chromatography were conducted similar to during the WINTER (Wintertime Investigation of Transport, Emissions, and Reactivity) Campaign (Sullivan et al. 2019). Accuracy is estimated to be 10% and precision is 0.4 ug m^{-3}.

2.1.9 Whole air samples

During WE-CAN the NCAR community requestable Advanced Whole Air Sampler (AWAS) system (Andrews et al. 2016) (`www.eol.ucar.edu/instruments/advanced-whole-air-sampler`) was operated by CSU. The AWAS collects canister samples for off-line analysis of VOCs. For WE-CAN up to 46 canister samples could be collected per flight triggered by an on-board operator. Typically a background sample was collected upwind of the fire and 1-3 samples per plume crossing. This included (as possible) a sample when transitioning into the smoke, at the peak of the smoke, and when exiting the smoke. Following each flight the canisters were shipped to CSU to be analyzed for a total of 61 individual VOCs (C_1-C_{10} NMHCs, C_1-C_5 alkyl nitrates and oxygenated VOCs) using a five-channel GC (gas chromatograph) system equipped with three flame ionization detectors (FIDs), one electron capture detector (ECD) and one mass spectrometer. More details on the instrument and analysis methods can be found in Russo et al. (2010), Zhou et al. (2010), and Benedict et al. (2019). The measurement

precision is based on repeated analysis of two calibrated whole air standards that ranged from 1%-8% for the NMHCS (non-methane hydrocarbons) and 3%-5% for the alkyl nitrates (Russo et al. 2010). The accuracy of the alkyl nitrates is 10-20% and the detection limit is 0.01 pptv.

2.1.10 NCAR Trace Organic Gas Analyzer (TOGA)

TOGA measured a wide range of VOCs including C_3-C_{10} non-methane hydrocarbons (NMHCs) and C_1-C_4 oxygenated VOCs (oVOCs). TOGA is a fast online mass spectrometer gas chromatograph (Apel et al. 2003, 2015) that had a sample collection time of 28 s every 100 s for the first 11.5 research flights before transitioning to a 33 s sampling time out of every 105 s for the remainder of the research flights.

2.1.11 NCAR HIAPER Atmospheric Radiation Package (HARP)

HARP measures spectrally-resolved actinic flux with a full sky field of view. Two hemispheric light collectors, located above and below the body of the C-130, are each connected by fiber optics to a monolithic solid state spectrograph with a CCD detector (Shetter and Müller 1999). The wavelength range is 280nm - 680 nm with an effective 1.8 nm FWHM (Full Width at Half Maximum) resolution. Response time is > 1Hz, with an accuracy of 4-6% and a precision of ∼1%. Periodic calibration for absolute power via NIST traceable standard lamps was done in the field, and laboratory calibrations were performed before and after the field deployment. The photochemistry portion of the NCAR Tropospheric Ultraviolet and Visible (TUV) radiation model (Madronich 1987) is used to process the measured flux spectra, with cross sections and quantum yields based on recommended JPL and IUPAC values. Default TUV v5.3.2 reaction settings are used for most photolysis rate coefficient calculations during WE-CAN. A combination of quasi-Gaussian uncertainties in actinic flux mixed with uncertainties in the cross-sections, quantum yields and NIST light sources yield total uncertainties in the 10 - 20 % for most reactions.

TABLE 2.1. Key measurement details and contact information for all measurements used in Chapters 3, 4, and 5.

Measurement	Technique	Detection Limit, Uncertainty	Potential Interferences	PI, Institution, Contact, Reference
NO	chemi-luminescence	100 pptv, 6%		Andy Weinheimer, NCAR, wein@ucar.edu, (Ridley and Grahek 1990)
NO_2	chemi-luminescence	140 pptv, 12%	HONO, expected to be small	Andy Weinheimer, NCAR, wein@ucar.edu, (Ridley and Grahek 1990)
O_3	chemi-luminescence	200 pptv, 6%		Andy Weinheimer, NCAR, wein@ucar.edu, (Ridley et al. 1992)
NH_3	QC-TILDAS	200 pptv, 12%		Ilana Pollack, Colorado State, ipollack@rams.colostate.edu, (Pollack et al. 2019)
HCN	I-CIMS	112 pptv, 30%		Joel Thornton, U. Washington, joelt@uw.edu, (Lee et al. 2014)
HNCO	I-CIMS	70.4 pptv, 30%		Joel Thornton, U. Washington, joelt@uw.edu, (Lee et al. 2014)

TABLE 2.1. Key measurement details and contact information for all measurements used in Chapters 3, 4, and 5.

Measurement	Technique	Detection Limit, Uncertainty	Potential Interferences	PI, Institution, Contact, Reference
HONO	I-CIMS	13.5 pptv, 30%		Joel Thornton, U. Washington, joelt@uw.edu, (Lee et al. 2014)
HNO_3	I-CIMS	20.5 pptv, 30%		Joel Thornton, U. Washington, joelt@uw.edu, (Lee et al. 2014)
organic nitrates	I-CIMS	NA, 200%		Joel Thornton, U. Washington, joelt@uw.edu, (Lee et al. 2014)
PAN	thermal dissociation I-CIMS	20 pptv, 12%		Frank Flocke, NCAR, ffl@ucar.edu, (Zheng et al. 2011)
PPN	thermal dissociation I-CIMS	20 pptv, 12%		Frank Flocke, NCAR, ffl@ucar.edu, (Zheng et al. 2011)

TABLE 2.1. Key measurement details and contact information for all measurements used in Chapters 3, 4, and 5.

Measurement	Technique	Detection Limit, Uncertainty	Potential Interferences	PI, Institution, Contact, Reference
$p\mathrm{NH_4}$	HR-ToF-AMS	<0.1 μg m^{-3}, 35%	includes possible inorganic and organic contributions	Delphine Farmer, Colorado State, delphine.farmer@colostate.edu, (Bahreini et al. 2009)
$p\mathrm{NO_3}$	HR-ToF-AMS	<0.1 μg m^{-3}, 35%	includes possible inorganic and organic contributions	Delphine Farmer, Colorado State, delphine.farmer@colostate.edu, (Bahreini et al. 2009)
$\mathrm{N_2O}$	QC-TILDAS	100 pptv, 1 ppbv	spectral interference from purge gas accounted for	Teresa Campos, NCAR, campos@ucar.edu, (Lebegue et al. 2016)
CO	QC-TILDAS	100 pptv, 0.6 ppbv	purge gas scrubbed to CO < 1 ppbv	Teresa Campos, NCAR, campos@ucar.edu, (Lebegue et al. 2016)

TABLE 2.1. Key measurement details and contact information for all measurements used in Chapters 3, 4, and 5.

Measurement	Technique	Detection Limit, Uncertainty	Potential Interferences	PI, Institution, Contact, Reference
CO	PICARRO G-2401-m	30 pptv, NA		Teresa Campos, NCAR, campos@ucar.edu
CO_2	PICARRO G-2401-m	20 pptv, 0.05 ppmv		Teresa Campos, NCAR, campos@ucar.edu
CH_4	PICARRO G-2401-m	2 pptv, NA		Teresa Campos, NCAR, campos@ucar.edu
NO_3^-	PILS	0.4 μg m^{-3}, 10%		Amy Sullivan, Colorado State, Amy.Sullivan@colostate.edu, (Sullivan et al. 2019)
NH_4^+	PILS	0.4 μg m^{-3}, 10%		Amy Sullivan, Colorado State, Amy.Sullivan@colostate.edu, (Sullivan et al. 2019)
alkyl nitrates	WAS and GC-MS	0.1 pptv, 10-20%		Jeff Collett, Colorado State, Jeffrey.Collett@colostate.edu , (Russo et al. 2010)

TABLE 2.1. Key measurement details and contact information for all measurements used in Chapters 3, 4, and 5.

Measurement	Technique	Detection Limit, Uncertainty	Potential Interferences	PI, Institution, Contact, Reference
actinic flux	spectrograph with CCD	~1%, 4-6%		Sam Hall, NCAR, halls@ucar.edu, (Shetter and Müller 1999)
acetonitrile	PTR-ToF-MS	0.07 ppb, 15%		Lu Hu, U. Montana, lu.hu@mso.umt.edu, (Sekimoto et al. 2017)
ethenamine	PTR-ToF-MS	NA, 50%		Lu Hu, U. Montana, lu.hu@mso.umt.edu, (Sekimoto et al. 2017)
propene amine	PTR-ToF-MS	NA, 50%		Lu Hu, U. Montana, lu.hu@mso.umt.edu, (Sekimoto et al. 2017)
trimethylamine	PTR-ToF-MS	NA, 50%		Lu Hu, U. Montana, lu.hu@mso.umt.edu, (Sekimoto et al. 2017)
butene amine	PTR-ToF-MS	NA, 50%		Lu Hu, U. Montana, lu.hu@mso.umt.edu, (Sekimoto et al. 2017)

TABLE 2.1. Key measurement details and contact information for all measurements used in Chapters 3, 4, and 5.

Measurement	Technique	Detection Limit, Uncertainty	Potential Interferences	PI, Institution, Contact, Reference
formamide	PTR-ToF-MS	NA, 50%		Lu Hu, U. Montana, lu.hu@mso.umt.edu, (Sekimoto et al. 2017)
acetamide	PTR-ToF-MS	NA, 50%		Lu Hu, U. Montana, lu.hu@mso.umt.edu, (Sekimoto et al. 2017)
propane nitrile	PTR-ToF-MS	NA, 50%		Lu Hu, U. Montana, lu.hu@mso.umt.edu, (Sekimoto et al. 2017)
hydroxy acetonitrile + methyl isocyanate	PTR-ToF-MS	NA, 40%		Lu Hu, U. Montana, lu.hu@mso.umt.edu, (Sekimoto et al. 2017)
cyanoallene isomers	PTR-ToF-MS	NA, 50%		Lu Hu, U. Montana, lu.hu@mso.umt.edu, (Sekimoto et al. 2017)

TABLE 2.1. Key measurement details and contact information for all measurements used in Chapters 3, 4, and 5.

Measurement	Technique	Detection Limit, Uncertainty	Potential Interferences	PI, Institution, Contact, Reference
pentanenitriles	PTR-ToF-MS	NA, 50%		Lu Hu, U. Montana, lu.hu@mso.umt.edu, (Sekimoto et al. 2017)
4-methyl pentanenitrile	PTR-ToF-MS	NA, 50%		Lu Hu, U. Montana, lu.hu@mso.umt.edu, (Sekimoto et al. 2017)
benzonitrile	PTR-ToF-MS	NA, 50%		Lu Hu, U. Montana, lu.hu@mso.umt.edu, (Sekimoto et al. 2017)
furancarbonitriles	PTR-ToF-MS	NA, 50%		Lu Hu, U. Montana, lu.hu@mso.umt.edu, (Sekimoto et al. 2017)
nitromethane	PTR-ToF-MS	NA, 50%		Lu Hu, U. Montana, lu.hu@mso.umt.edu, (Sekimoto et al. 2017)
nitropropanes	PTR-ToF-MS	NA, 50%		Lu Hu, U. Montana, lu.hu@mso.umt.edu, (Sekimoto et al. 2017)

TABLE 2.1. Key measurement details and contact information for all measurements used in Chapters 3, 4, and 5.

Measurement	Technique	Detection Limit, Uncertainty	Potential Interferences	PI, Institution, Contact, Reference
nitroethane or ethane nitrite	PTR-ToF-MS	NA, 50%		Lu Hu, U. Montana, lu.hu@mso.umt.edu, (Sekimoto et al. 2017)
nitroethene	PTR-ToF-MS	NA, 50%		Lu Hu, U. Montana, lu.hu@mso.umt.edu, (Sekimoto et al. 2017)
nitrotoluene	PTR-ToF-MS	NA, 50%		Lu Hu, U. Montana, lu.hu@mso.umt.edu, (Sekimoto et al. 2017)
pyrrole + butene nitrile isomers	PTR-ToF-MS	NA, 40%		Lu Hu, U. Montana, lu.hu@mso.umt.edu, (Sekimoto et al. 2017)
dihydropyrrole + butane nitrile	PTR-ToF-MS	NA, 40%		Lu Hu, U. Montana, lu.hu@mso.umt.edu, (Sekimoto et al. 2017)

TABLE 2.1. Key measurement details and contact information for all measurements used in Chapters 3, 4, and 5.

Measurement	Technique	Detection Limit, Uncertainty	Potential Interferences	PI, Institution, Contact, Reference
methyl pyrrole isomers	PTR-ToF-MS	NA, 40%		Lu Hu, U. Montana, lu.hu@mso.umt.edu, (Sekimoto et al. 2017)
ethylnylpyrrol	PTR-ToF-MS	NA, 50%		Lu Hu, U. Montana, lu.hu@mso.umt.edu, (Sekimoto et al. 2017)
methyl pyridines	PTR-ToF-MS	NA, 50%		Lu Hu, U. Montana, lu.hu@mso.umt.edu, (Sekimoto et al. 2017)
vinylpyridine	PTR-ToF-MS	NA, 50%		Lu Hu, U. Montana, lu.hu@mso.umt.edu, (Sekimoto et al. 2017)
dihydroxy pyridine	PTR-ToF-MS	NA, 40%	methyl maleimide	Lu Hu, U. Montana, lu.hu@mso.umt.edu, (Sekimoto et al. 2017)
nitrofuran	PTR-ToF-MS	NA, 50%		Lu Hu, U. Montana, lu.hu@mso.umt.edu, (Sekimoto et al. 2017)

TABLE 2.1. Key measurement details and contact information for all measurements used in Chapters 3, 4, and 5.

Measurement	Technique	Detection Limit, Uncertainty	Potential Interferences	PI, Institution, Contact, Reference
acetaldehyde	PTR-ToF-MS	0.2 ppb, 15%		Lu Hu, U. Montana, lu.hu@mso.umt.edu, (Sekimoto et al. 2017)
2,3butanedione (biacetyl)	PTR-ToF-MS	NA, 50%	methyl acrylate, maybe ethylglyoxal?	Lu Hu, U. Montana, lu.hu@mso.umt.edu, (Sekimoto et al. 2017)
propanal	PTR-ToF-MS	0.13 ppb, 15%	acetone	Lu Hu, U. Montana, lu.hu@mso.umt.edu, (Sekimoto et al. 2017)
methylglyoxal	PTR-ToF-MS	NA, 40%	acrylic acid	Lu Hu, U. Montana, lu.hu@mso.umt.edu, (Sekimoto et al. 2017)

2.2 COMMON METHODS

2.2.1 Plume Transect Criteria

A plume transect is defined as an individual flight segment that perpendicularly transects a smoke plume with background air present on both sides. Start and end times for plume transects were visually identified when the time series of CO, HCN, and NH_3 all concurrently and sharply deviated from their average background mixing ratios. If one or more of these measurements was missing (e.g., during a calibration) additional tracers were employed such as PAN and NO_2. CO and HCN are considered to

be conservative tracers on the timescales of interest here (0 - 5 hours of physical transport) given their lifetimes of ~10 days and ~3 months, respectively, during summer (Holloway et al. 2000; Li et al. 2000). Plume transects attributed to a single fire are grouped for further analysis.

2.2.2 Modified combustion efficiency

A large wildfire contains a range of burning conditions at any given time. The mixture of processes in a single wildfire can result in a smoke plume that may have a flaming combustion signature, or a smoldering one (Yokelson et al. 1997), or emissions dominated by pyrolysis and flame oxidation at different temperatures (Roberts et al. 2020; Sekimoto et al. 2018). The combustion temperature is a complex function of fuel moisture, type, geometry and other environmental factors such as turbulence (*e.g.* McAllister 2019) and will affect both the form of initially volatilized N as well as the oxidation pathways of N_r in the radical-driven flame chemistry. The most common metric used to describe the integrated burn condition is the modified combustion efficiency (MCE) (*e.g.* Yokelson et al. 1996), calculated as the ratio of background-corrected carbon dioxide (CO_2) to the sum of background-corrected CO_2 and background-corrected carbon monoxide (CO), shown in Equation 2.1. MCE values close to 1 indicate flaming combustion whereas MCE values closer to 0.8 indicate smoldering combustion, and values in between represent a mixture of combustion processes.

$$\mathrm{MCE} = \frac{\Delta \mathrm{CO_2}}{\Delta \mathrm{CO_2} + \Delta \mathrm{CO}} \tag{2.1}$$

2.2.3 Normalized Excess Mixing Ratio (NEMR) Calculations

In comparing abundances of a species of interest between different smoke plumes, it is useful to normalize the measurements by dividing by the abundances of a conserved tracer. This conserved tracer accounts for dilution, and is typically CO, or HCN. This ratio is called the normalized excess mixing ratio (NEMR) of species X. Problems arise in the interpretation of NEMRs when the composition of background air is changing (Yokelson et al. 2013a). There can be large (i.e. orders of magnitude) variability in NEMRs for a given fire even in a controlled setting (Gilman et al. 2015). Two methods are commonly used to calculate NEMRs in wildfire smoke plumes: the integration method, and the slope method (Yokelson et al. 2013b). Both approaches assume that different parts of the plume segment are not coming from different parts of the fire, which might be burning at different stages. Briefly, the integration method subtracts the background of X from the time series of X, and the background of CO from the timeseries of CO, then divides the sum of ΔX by the sum of ΔCO to calculate the NEMR.

To use this approach, each measurement can be interpolated onto the same timebase, so long as each measurement is fast enough to capture the variability well across the plume transect. One strength of this method is that it integrates across all the mass in a given plume transect, while requiring the identification or estimation of a background for each species. The slope method calculates the NEMR by finding the slope of an orthogonal least squares fit to the relationship between CO and species X. This approach assumes the data are perfectly time-aligned, and does not need a separate background estimate, but it is sensitive to the chemistry in the most dense parts of the plume driving the overall NEMR. The intercept of the fit can be used to estimate a background if desired.

In the following Chapters, we use the integration method for calculating nearly all NEMRs, in order to enable a more robust total mass conversion of NEMR to EFs. The only exception is the NEMR of CO_2, where the slope method allows for a more robust calculation of MCE from the CO_2/CO ratio. To estimate the background for each perpendicular plume transect, we average 15 seconds of measurements before and after entering and exiting the plume, respectively. Most of the observations used in our analysis were collected at 1-Hz or higher. In these cases, only data points with valid measurements of both species X and CO are used in calculating ΔX and ΔCO. AMS data was reported on a 5-second timebase, and these data are merged with the 1 second data, and converted into ambient mixing ratio equivalent from standard mass concentration units.

2.2.4 Uncertainties

Uncertainty in NEMRs and emission factors (EF: described in Chapter 3.1) is propagated from the reported precision and accuracy of each measurement, summed in quadrature. In cases where multiple NEMRs or EFs are averaged the uncertainty reported is the root square sum of the standard deviation and the propagated uncertainties from each individual estimate.

2.2.5 Physical and Chemical Age Estimates

We estimate the physical age of a plume by dividing the distance between the fire emission source and each downwind plume transect by the plume wind speed. The distance is measured from the centroid of the active burn area on that day to the center of the plume transect, and wind speed is estimated as the average wind speed across all downwind plume transects sampled for that fire. If a smoke plume from a given fire was sampled again ($i.e.$ the smoke plume was followed downwind and then the aircraft returned to the fire and repeated the pattern), a separate average wind speed was calculated from the second set of passes and used to estimate the physical age of the transects in that pseudo-Lagrangian pattern. Estimated physical ages could deviate from the true plume age at each transect due to several

factors including variable wind speeds along the aircraft and plume trajectories, uncertainties in the active burn location, and differences in atmospheric friction and entrainment. We estimate the uncertainty in our calculations of physical age using the 1σ standard deviation in the mean wind speed across each set of plume transects. Uncertainty in the fire location at the specific time of sampling is not available. To assess the efficacy of attempted pseudo-Lagrangian sampling efforts, an estimated emission time (t_0) was calculated for each plume transect by subtracting the estimated physical age from the time the plume transect occurred. Most sets of plume transects contained transects all with estimated t_0 within 2 hours. Fires with pseudo-Lagrangian sampling patterns with sets of transects containing t_0 differences > 2 hours were excluded from this analysis in order to limit the possible influence of time-varying emissions and evolution on our analysis. We also excluded plume intercepts that were not connected to the intended pseudo-Lagrangian sampling efforts (i.e. sampled smoke from other fires nearby or from portions of the plume not entrained in the mean atmospheric flow). See the SI for a full list of plume transect start and stop times. Since the lifetime of both HCN and CO are much greater than the elapsed sampling time, we would expect HCN NEMRs to remain constant with plume physical age in a true Lagrangian sampling system. In the 8 pseudo-Lagrangian sampling cases identified, HCN NEMRs were confirmed to remain constant within propagated error with estimated physical plume age (Figure A1).

We also assigned a broader set of smoke plume intercepts an approximate chemical age following O'Dell et al. (in preparation). Briefly, smoke-influenced data were identified using co-elevated CO > 85 ppbv, HCN > 275 pptv, and CH_3CN > 200 pptv. Smoke-influenced data were assigned an approximate chemical age using three VOCs with different 2nd-order reaction rate constants for loss via reaction with OH: 2-methylfuran (k_{OH} = 7.31 x 10^{-11} cm^3 molecule^{-1} s^{-1}, Aschmann et al. 2011), acrolein (k_{OH} = 1.96 x 10^{-11} cm^3 molecule^{-1} s^{-1}, Atkinson 1986; NIST Chemical Kinetics Database), and acrylonitrile (k_{OH} = 4.04 x 10^{-12} cm^3 molecule^{-1} s^{-1}, Harris et al. 1981; NIST Chemical Kinetics Database). Based on which of these three VOCs is above background abundances in a plume, O'Dell et al. (in preparation) grouped smoke samples into three bins. Young smoke has an estimated age of < 1 day, the medium smoke group includes smoke plumes with estimated ages of 1-3 days, and all smoke with estimated chemical ages > 3 days is categorized as old smoke. While this method likely captures the general progression of chemical aging in smoke, there are limitations: the binning of smoke samples is impacted by the age tracer dilution as well as chemistry, and the age assignments do depend on an assumed constant smoke OH concentration.

CHAPTER 3

EMISSIONS OF REACTIVE NITROGEN FROM WESTERN U.S. WILDFIRES DURING SUMMER 2018[1]

3.1 INTRODUCTION

As a reminder from the Introduction, reactive nitrogen (N_r = all N-compounds except N_2O and N_2) is emitted in many forms by wildfires, ranging from fully reduced (ammonia; NH_3) to highly oxidized (nitric acid; HNO_3). Biomass burning initially pyrolyzes fixed N as a handful of small N-containing compounds: NH_3, HCN, HNCO, and CH_3CN and minor amounts of other N-containing volatile organic compounds (NVOCs, including amine, amide, nitrile, nitro, isocyanate, and N-heterocyclic compounds) (Glarborg et al. 2018; Lobert and Warnatz 1993; Roberts et al. 2020). While still within the flame, some of these species are quickly oxidized by rapid radical chemistry to form the remainder of the species we consider to be primarily emitted by fires: N_2, NO, NO_2, N_2O, and HONO (Hansson et al. 2004; Ren and Zhao 2012, 2013a,b; Scharko et al. 2019; Sekimoto et al. 2018). The form of N_r emission has been shown to vary both with combustion conditions and with fuel N content (*e.g.* Burling et al. 2010; Coggon et al. 2016; Roberts et al. 2020). Flaming combustion is generally associated with higher burn temperatures and greater oxidation of initially pyrolyzed small N-compounds, with smoldering combustion characterized by lower burn temperatures and lesser oxidation, and higher fuel N content is typically correlated with higher overall N_r emissions.

During summer 2018, the Western Wildfires Experiment for Cloud Chemistry, Aerosol Absorption, and Nitrogen (WE-CAN: `https://www.eol.ucar.edu/field_projects/we-can`) field campaign sampled more than 20 major wildfires throughout the western U.S. The National Science Foundation/National Center for Atmospheric Research (NSF/NCAR) C-130 research aircraft was outfitted with a large suite of trace gas, aerosol, and remote sensing instrumentation and flew 19 research flights from bases in Boise, ID, and Broomfield, CO. The WE-CAN payload included a comprehensive set of N_r trace gas and aerosol measurements optimized for sampling wildfire smoke. Daytime flights included sampling during periods of rapid fire growth, and many smoke plumes were sampled within one hour of estimated emission. The number and diversity of large fires (> 1000 acres) sampled so close to emission represent one of the most comprehensive sets of *in situ* wildfire emission data collected to date. Close-by "emissions" transects were typically followed by pseudo-Lagrangian sampling

[1] Adapted from a manuscript in review in *JGR Atmospheres*, June 2020

downwind, enabling the aging of fresh smoke to be linked to various physical and chemical evolution processes. For the purposes of this emissions-focused analysis, we define 26 unique sampling periods within 80 minutes estimated physical age of emission. These "emissions transects" correspond to 16 individual fires, of which several were sampled over different days or multiple discrete times within one day (defined as transects greater than 30 minutes apart). In this Chapter I focus on empirical estimation of N_r emissions from the wildfires sampled by WE-CAN. We explore variability in the dominant forms of N_r between fires, and relate our observations to fuel and combustion differences. I also compare our emission estimates to previous work, in particular lab burns of specific fuels, to investigate the applicability of emission factors (EFs) across diverse fires.

3.2 Methods specific to this analysis

3.2.1 Fuels Classification

Wildland fuels that burned during each of the WE-CAN flights were characterized and summarized using the Fuel Characteristic Classification System (FCCS). FCCS defines a fuel bed as the inherent physical characteristics of aboveground biomass and classifies wildland fuel characteristics at 30-m resolution to predict surface fire behavior and available fuel for consumption and emissions estimation . We used FCCS maps generated from LANDFIRE 2014 (Rollins, 2009) in combination with incident specific perimeter mapping to estimate the fuels burned during each research flight. Specifically, we acquired daily infrared (IR) fire perimeters for each wildfire bracketing the times of each research flight. The primary sources for incident specific spatial heat perimeter data included the National Interagency Fire Center (NIFC) FTP Server (`https://ftp.nifc.gov/public/incident_specific_data/`) and the Geospatial Multi-Agency Coordination (GeoMAC) funded by the Geosciences and Environmental Change Center (USGS) (`https://rmgsc.cr.usgs.gov/outgoing/GeoMAC/`). We assigned a rating system for data quality that relates the match quality between the timing of the heat perimeter data and the times of the research flights. Once we vetted the daily perimeter data, we were able to use ArcGIS to summarize the wildland fuels that burned during each research flight. Fuels were summarized in descending order from most to least abundant wildland vegetation types. The X and Y field centroid of the burn area was identified for each flight using the Geometry tool in ArcGIS, and used as the fire location coordinates for further analysis.

LANDFIRE 2014 incorporates landscape change and disturbances, such as wildland fire, fuel and vegetation treatments, insects and disease, storm damage, and invasive plants that occurred in 2013

and 2014. As such, this layer does not represent elements of landscape change from 2014 to 2018. This is one of the larger potential sources of error in this analysis. We also focused exclusively on mapping the best available heat perimeters to bracket each research flight. This is a good metric for measuring new actively burning areas, but does little to estimate contributions from smoldering material from the day(s) preceding the research flights. In some forest types, smoldering combustion may be a large contribution to emissions that we simply do not capture well in this analysis. The use of satellite data may be able to improve the capacity to identify both smoldering and flaming contributions to emissions.

3.2.2 Plume criteria

For this analysis, we use plume transects with estimated physical ages < 80 minutes as "emission transects". The youngest smoke sampled was ~20 minutes old, while navigation and safety constraints limited the ability of the NSF/NCAR C-130 to fly within an hour of emission on several large fires. Normalized excess mixing ratios (NEMRs) and emission factors (EFs) calculated from plume transects sampled within a period of 30 minutes are averaged and assumed to represent one emissions pass for that fire. If another set of plume transects on the same fire was sampled > 30 minutes later in flight time, then they are averaged and considered a separate emissions pass. Extending the threshold to 100 minutes only adds a single sampling period, and lowering it to 60 minutes reduces the number of sampling periods by 25%. Our main conclusions do not change in either case. These "emissions transects" correspond to 16 individual fires, of which several were sampled over different days or multiple discrete times within one day (defined as transects greater than 30 minutes apart).

3.2.3 Normalized Excess Mixing Ratio (NEMR)

As a reminder from Chapter 2, the NEMR enables comparison of abundances between and within plumes (Yokelson et al., 2013). By accounting for dilution through normalizing a given measurement by a conserved tracer such as CO, we can investigate changes in abundances due to chemical production or consumption, as well as differences in emissions and aging between plumes. Here, we calculate the NEMR of species X for a given plume transect by calculating the integrated ΔX ($= \Sigma(X_{measured} - X_{background})$) and the integrated ΔCO ($= \Sigma(CO_{measured} - CO_{background})$) and dividing ΔX by ΔCO. Backgrounds for CO and the species X are calculated as the mean of 15 seconds of measurements before and after a given plume transect's start and end times, respectively.

Amendments to these methods were made for AWAS data, and for PILS data, measuring continuously on a 2 minute average timebase. Automated whole air sampler (AWAS) data were *in situ* snapshot measurements, with a canister fill time of 2-5 seconds. AWAS canisters were typically filled outside the

plume and then once as close to the middle of the plume as the C-130 traversed the cross section of the smoke plume. Here we use samples from the closest pass to each fire to calculate the normalized excess mixing ratio of methyl- to pentyl- nitrates. We average CO within the sampling time of the AWAS and use the AWAS measurement outside each plume that is closest in time to the in plume measurement as a background. The Alkyl nitrate NEMRs were then calculated for each plume pass as the difference in the in plume sample minus the background sample, divided by the difference in average CO mixing ratios during each respective AWAS sampling period.

The CSU PILS measured continuously on a 2 minute average timebase, meaning that some measurements included both in plume and out of plume sampling. We identified all PILS measurements that overlapped both partially and in full with plume transects, and used each of these measurements to calculate an NEMR. After converting the reported PILS measurement from standard mass concentration to equivalent parts per billion by volume mixing ratio, we assumed the background abundance of both NH_4 and NO_3 ions to be zero. We averaged the CO measurement over the PILS sample time, and after subtracting the background identified for that transect as the mean CO below the first percentile, we divide the PILS ion mixing ratio by the excess CO to estimate a NEMR. Assuming a background of 0 for the measured PILS ions means these estimates will be an upper bound on the PILS data-derived NH_4 and NO_3 ion NEMRs.

For all measurements, if data are missing during a specific plume transect then the NEMR for that species on that transect is not included in our analysis. Figures A2 and A3 show visually which NEMRs are missing for each fires and in Figure 3.1 we replace these missing NEMR values with the average NEMR across all emissions transects. This enables a more representative comparison of ΣN_r measured and its distribution. No substitution of average NEMRs for missing values are presented elsewhere in the Chapter.

3.2.4 Emission Factor (EF) Calculations

In the lab, it is possible to measure the mass of a species of interest emitted per mass of fuel burned. This quantity is called an emission factor (EF) in units of grams X per kilogram fuel or biomass, and is widely used as an input to estimate emissions in emission inventories. To calculate an EF based on our field measurements, we follow the total carbon mass balance method outlined in Liu et al. (2017). This method assumes that all of the volatilized carbon is detected, following Yokelson et al. (1999) and Liu et al. (2017). Equation 3.1 summarizes the calculation:

$$\mathrm{EF}_X = \frac{\Delta X}{\Delta \mathrm{CO}} \times \frac{1}{\sum \frac{n\Delta \mathrm{C}}{\Delta \mathrm{CO}}} \times \frac{\mathrm{MW}_X}{\mathrm{MW}_C} \times \%\mathrm{C \text{ in fuel}} \times 1000 \text{ g/kg} \tag{3.1}$$

Here the NEMR of species X is divided by the sum of NEMR of all carbon species measured (with n equaling the number of carbon atoms in each species) and then converted to mass by multiplying by the ratio of the molecular weight of X and the atomic weight of C, the estimated percentage of carbon in biomass, and the unit conversion from kilograms (kg) to grams. In this analysis we assume the mass of carbon in one kg biomass is 0.457 kg, or 45.7% based on the analysis of Santín et al. (2015). We also assume total VOCs and black carbon make up < 3% of total carbon in smoke (following Yokelson et al. 1999), simplifying the sum of carbon NEMRs to Equation 3.2:

$$\sum \frac{n\Delta \mathrm{C}}{\Delta \mathrm{CO}} = \frac{1 * \Delta \mathrm{CO_2}}{\Delta \mathrm{CO}} + \frac{1 * \Delta \mathrm{CO}}{\Delta \mathrm{CO}} + \frac{1 * \Delta \mathrm{CH_4}}{\Delta \mathrm{CO}} \tag{3.2}$$

This assumption will mean that presented values could be an overestimate of the true EF by a few percent. This is small compared to the observed variability and uncertainty associated with our EF estimates.

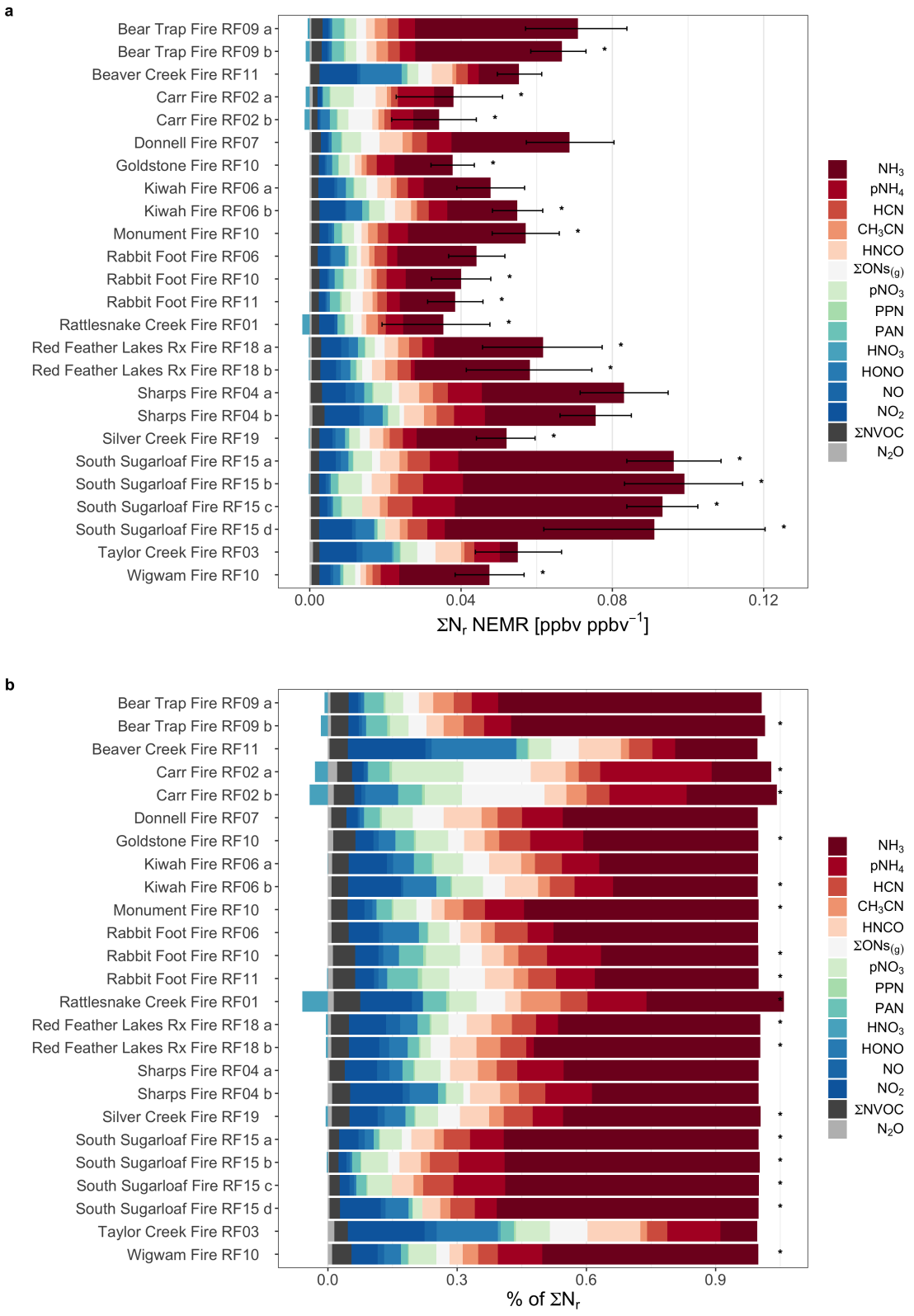
a
Bear Trap Fire RF09 a
Bear Trap Fire RF09 b
Beaver Creek Fire RF11
Carr Fire RF02 a
Carr Fire RF02 b
Donnell Fire RF07
Goldstone Fire RF10
Kiwah Fire RF06 a
Kiwah Fire RF06 b
Monument Fire RF10
Rabbit Foot Fire RF06
Rabbit Foot Fire RF10
Rabbit Foot Fire RF11
Rattlesnake Creek Fire RF01
Red Feather Lakes Rx Fire RF18 a
Red Feather Lakes Rx Fire RF18 b
Sharps Fire RF04 a
Sharps Fire RF04 b
Silver Creek Fire RF19
South Sugarloaf Fire RF15 a
South Sugarloaf Fire RF15 b
South Sugarloaf Fire RF15 c
South Sugarloaf Fire RF15 d
Taylor Creek Fire RF03
Wigwam Fire RF10
0.00
0.04
0.08
0.12
ΣNr NEMR [ppbv ppbv−1]
NH3
pNH4
HCN
CH3CN
HNCO
ΣONs(g)
pNO3
PPN
PAN
HNO3
HONO
NO
NO2
ΣNVOC
N2O
b
0.0
0.3
0.6
0.9
% of ΣNr

FIG. 3.1. a) Normalized excess mixing ratios (NEMRs) of measured N_r species for emission transects of WE-CAN fires. Asterisks indicate one or more NEMR estimates are missing and were filled using the mean NEMR for that species across the rest of the emission transects (see Table A1 for which species are missing for each fire). b) Fractional contribution to total measured reactive nitrogen (ΣN_r) measured in young smoke plumes during WE-CAN. Sums greater than one during some emission transects reflect small negative NEMRs for HNO_3 as described in the text. $p$$NH_4$ and $p$$NO_3$ data are from the AMS.

3.3 RESULTS AND DISCUSSION

3.3.1 ΣN_r Partitioning

Figure 3.1a shows that the total measured excess mixing ratio of ΣN_r relative to CO varies between 0.033 - 0.099 ppbv/ppbv, or 3.3 - 9.9% of CO in emission transects. Warm colors here indicate measured reduced N_r species, whereas the cooler green and blue colors denote oxidized N_r species. The total ΣN_r NEMR varies by a factor of three between fires, much larger than the variability within emission transects of the same fire (separated by at least 30 minutes). However, it's important to recognize the total observed ΣN_r is a lower bound estimate, since there are minor missing measurements of N_r species likely to be present in smoke. The star above specific emission transects indicates that a NEMR for at least one species was missing and was filled in using the average of the NEMR for that species from the other emission transects. N_r species with the largest emission transect enhancements include gas-phase NH_3, NO_2, and HONO, as well as $p$$NH_4$ and $p$$NO_3$. NEMRs for seven alkyl nitrates from methyl- up to pentyl-nitrate were also calculated from the AWAS data (method described in Section 3.2.3), but together contribute less than 1% of the total measured ΣN_r, thus are not shown in Figure 3.1. Figure A1 in the appendix shows the same composite ΣN_r replacing the AMS ions with those measured by the PILS. PILS measurements of NO_3^- and NH_4^+ are generally smaller than AMS measurements of total $p$$NO_3$ and $p$$NH_4$, and offer an estimate of the inorganic aerosol N contribution. The overall conclusions from Figure 3.1 continue to hold when replacing the AMS fragment NEMR estimates with PILS ion NEMRs. Work is ongoing to elucidate the differences between the AMS and PILS measurements and to partition the AMS total $p$$NO_3$ and $p$$NH_4$ into inorganic and organic components. Figures A2 and A3 plot each N_r species' NEMRs per fire in separate panels, showing where data are missing and what variability exists in each species' NEMRs, and this information is also summarized in Table A1.

Figure 3.1b displays the relative proportions of the measured ΣN_r NEMRs for the same emission transects. Sums greater than 1 are possible in the case of negative NEMRs for HNO_3 or N_2O, discussed below, and a star above a given bar again indicates that a missing NEMR was filled in with the average

NEMR prior to calculating the percentage contribution. We find that reduced N_r species generally make up more than half of the of total observed ΣN_r (39 - 80%; median = 66%), with NH_3 making the largest contribution followed by pNH_4, HCN, and HNCO, and CH_3CN. Oxidized N_r species are dominated by NO_2, HONO, pNO_3, and ΣONs, with variability in the relative contributions of each. We also note again that the quantification of the ONs has a large uncertainty. On average smaller NO_y contributors to the total observed ΣN_r include NO, PAN, and PPN. NO_x does not make up the majority of measured ΣNO_y in most of these emission transects. The sum of N organic compounds measured by the PTR-ToF-MS (ΣNVOCs), not including CH_3CN, account for between 2-6% of ΣN_r, and, given the uncertainties in the NVOC measurements and number of other likely unquantified NVOCs, this is likely a lower bound for the contribution of all NVOCs to total N_r. The estimated physical age of these transects ranges from 20 - 80 minutes, and given the large abundances of PAN, pNO_3, and ΣONs, even in the freshest plumes we find evidence of previous conversion of NO_x to other NO_y species. This rapid chemical evolution appears to occur in both the most diffuse and densest smoke plumes. Another key finding of WE-CAN is that there can be significant emissions of HONO relative to NO_x. The impact of this is discussed in Peng et al. (2020) and this finding is consistent with laboratory experiments (Selimovic et al. 2018). Here we simply note this in the context of all the N_r emission ratios we were able to calculate.

Appendix tables contain additional information: Table A1 provides the species that are missing for each emission transect; Table A2 contains location and fuel types for each fire; and Table A3 contains sampling times, mean altitude of sampling, and mean estimated physical age of the emission transects for each fire. As noted above, small negative NEMRs are estimated for HNO_3 for some emission transects. This is due to lower mixing ratios measured inside the plume as compared to the background values outside the plume. In the case of HNO_3, this could be due to rapid reaction of background and possible plume produced HNO_3 with fire-emitted NH_3 and uptake to aerosol, which is then measured as enhancements in pNO_3. N_2O was another species which sometimes posed challenges to the estimation of NEMRs. For some diffuse plumes, such as Rattlesnake Creek RF01, N_2O was not clearly enhanced above background levels. N_2O is long-lived in the troposphere and has a relatively high background ($\sim$330 ppbv). Given expected emission factors (Akagi et al. 2011) of 0.16 g kg^{-1} for N_2O and 89 g kg^{-1} CO for temperature forests, we should only expect to see $\sim$1 ppbv enhancement in N_2O in plumes with maximum CO < 1000 ppbv. This is close to the estimated uncertainty in the N_2O measurement ($\pm$0.5 ppbv). Examples of the timeseries of N_2O, CO, NH_3, and CO_2 for four examples of different density plumes are included in the supplement to show differences between species with

generally large enhancements relative to background (CO and NH_3) and species with relatively smaller enhancements relative to background (N_2O and CO_2) (Figures A4 - A7). Without clear enhancements above background, estimated NEMRs ranged from small positive values to small negative values. Since the negative values are likely a measurement and background-driven artifact, here we include a correlation filter for N_2O NEMRs. Any N_2O NEMR for a transect where N_2O and CO did not have a positive correlation > 0.5 was set to NaN.

Taken together, Figures 3.1a and 3.1b indicate significant fire-to-fire variability in total observed N_r enhancements and their distribution across N_r species. Several lab studies have confirmed the influence of both burn conditions and fuel N on the emissions of N_r. Burling et al. (2010) found that N_r emission factors in the lab were dependent on both MCE and fuel N content, with higher fuel N corresponding to higher N_r emission factors. Coggon et al. (2016) also found that fuel N content plays a role in the emissions of important N_r species. Most recently, Roberts et al. (2020) show that the measured total ΣN_r in smoke correlates strongly with the mass of fuel N burned. Both fuel type and location may contribute to differences in fuel N content. Variability may exist between fuel species and within different parts of the same plant (*e.g.* Burling et al. 2010). Fire characteristics such as burn temperature, geometry, fuel moisture, and combustion efficiency will all impact the total quantity of N_r in smoke if they change the fraction of fuel N released; these factors can also strongly affect the distribution of the N_r. Burling et al. (2010) and Roberts et al. (2020) observed that this fraction of N loss to the atmosphere varied in laboratory burns from 0.16 - 0.9. Thus, the total fuel N available to be volatilized as well as the burn conditions influencing what fraction of that available fuel N is volatilized both affect the total N_r emitted by wildfires. However, the WE-CAN observations of large wildfires do not provide a constraint on the fuel N content or the total amount volatilized. A large fraction of fuel N is released as N_2 (*e.g.* Kuhlbusch et al. 1991) and some fraction of fuel N remains in the ash after burning (*e.g.* Yokelson et al. 1996). *In situ* N_2 measurements were not attempted during WE-CAN (and would not likely be precise enough to quantify denitrification of fuel N to N_2), and accurate ground measurements of fuel- and ash- N content of each fire at the time of sampling are not available.

We do not observe significant variability in total observed ΣN_r enhancements between emission transects on the same fires sampled over multiple 30 minute periods during the same flight (fire names with a, b, or c after them in Figure 3.1a). The relative distribution of N_r species is also similar across these pairs or triplet sets of emissions transects. In other words, over short time periods (30 minutes

to several hours during afternoon/early evening) we are not able to discern whether these fires are changing quickly with respect to the amount or distribution of N_r they emit.

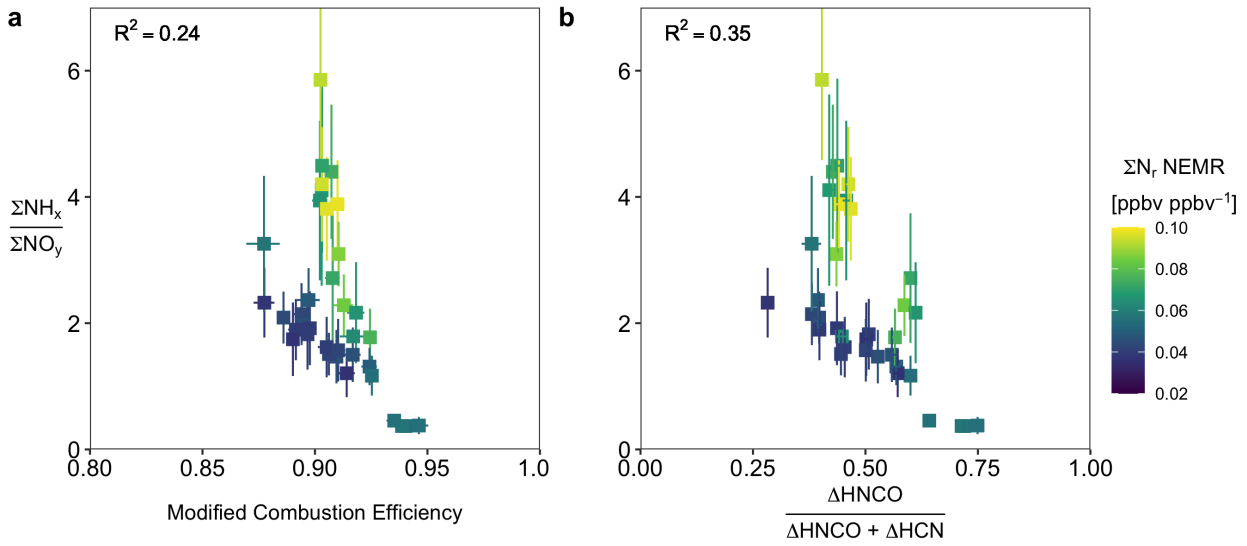

FIG. 3.2. Relationships between the ratio of ΣNH_x [$= NH_3 + pNH_4$] to ΣNO_y with: a) MCE, and b) the fraction of HCN + HNCO that exists as HNCO.

3.3.2 N_r Distribution Dependencies

Previous research has explored the relationship between combustion efficiency and other metrics of burn conditions, and the ratio of reduced to oxidized N_r in wildfire smoke (*e.g.* Goode et al. 1999; McMeeking et al. 2009). As noted in the introduction, the MCE can reflect different mixtures of fire processes that produce N_r emissions, with a lower MCE fire expected to produce more NH_3, and a higher MCE fire expected to produce more NO_x. Figure 3.2a presents a scatter plot of the molar ratio of $\Sigma NH_x/\Sigma NO_y$, where $\Sigma NH_x = NH_3 + pNH_4$ and ΣNO_y = sum of measured oxidized N species (NO, NO_2, HONO, HNO_3, PAN, PPN, pNO_3). We display this ratio instead of NH_3/NO_x (Figure A8) to account for chemical evolution in the time since emission. WE-CAN emission transects display a weak negative relationship between this ratio and MCE ($R^2 = 0.24$). This negative relationship is expected given past studies have found similar negative relationships in lab and field data, though the variance explained by MCE in past studies has sometimes been higher. For example, in both boreal wildfires and savannah grass fires, Goode et al. (1999, 2000) found that the ratio of NH_3/NO_x had a strong negative relationship with MCE ($R^2 = 0.94$) that could be fit well using the same linear regression of MCE. However, McMeeking et al. (2009) show with additional lab and field data that the ratio of NH_3/NO_x is not always strongly anti-correlated with MCE. The WE-CAN data similarly show that while MCE may explain the general

pattern in the $\Sigma NH_x/\Sigma NO_y$ ratio observed for large daytime western U.S. wildfires, other factors contribute to the variability in this ratio as well. For instance, the colorbar in Figure 3.2 indicates that the total amount of measured ΣN_r has a positive correlation with the $\Sigma NH_x/\Sigma NO_y$ ratio. That is, the more N_r emitted by the fire, the more NH_3 we might expect to be present relative to NO_x. The relationship of $\Sigma NH_x/\Sigma NO_y$ with ΣN_r itself has a $R^2 = 0.43$, with ΣN_r explaining a small amount more of the variance in $\Sigma NH_x/\Sigma NO_y$ than MCE (shown in Figure A9). The measured ΣN_r likely contains information about the fuel N content combined with how much fuel N was volatilized, complicated by how much of the volatilized N_r was denitrified to N_2.

Given our understanding of the initial pyrolysis of fuel N, holding denitrification ($N_r \rightarrow N_2$) reactions constant, we would expect a higher observed total ΣN_r to reflect a higher amount of fuel N volatilized. A higher amount of fuel N volatilized would manifest as increased amounts of N in small reduced forms (NH_3, HCN, HNCO). In the flame chemistry following the initial volatilization, some portion of these more reduced forms are oxidized to NO_x and HONO. The MCE likely reflects the combustion temperatures, with higher MCE and higher temperatures leading to more complete oxidation and vice versa. Combustion temperatures are also likely linked to the amount of denitrification that takes place. With higher combustion temperatures we would expect more denitrification. This would be a different reason for measured ΣN_r to be smaller at higher MCE. The pattern in the coloration of Figure 3.2 is consistent with contributions from each of these three linked processes. There is a higher $\Sigma NH_x/\Sigma NO_y$ ratio at lower MCE points, and when the total observed ΣN_r is higher at a given MCE, this ratio also increases. Therefore, the variability in the ratio of $\Sigma NH_x/\Sigma NO_y$ is likely influenced by both burn conditions and the total fuel N volatilized.

We also compare the fraction of HNCO in the sum of HNCO and HCN to the ratio of $\Sigma NH_x/\Sigma NO_y$ in Figure 3.2b. We hypothesize that the ratio of $\Sigma NH_x/\Sigma NO_y$ will have a tighter correlation with the fraction of HNCO than MCE because emissions of HNCO and HCN have been shown to have a temperature dependence (Hansson et al. 2004; Roberts et al. 2020), and are directly influenced by the amount of fuel N (Coggon et al. 2016). We do indeed find a weak negative relationship, shown in Figure 3.2b, with lower $\Sigma NH_x/\Sigma NO_y$ ratios at higher HNCO fractions (and higher assumed combustion temperatures). However, this negative relationship ($R^2 = 0.35$) is not much stronger than that with MCE, and so our hypothesis that the HNCO fraction would have a more clear relationship with other N_r species is not supported. This may be because both HCN and HNCO can be oxidized to other species (NO_x,

HONO etc.) and we should expect more oxidation with increasing combustion temperature. If this oxidation affects HCN and HNCO somewhat differently, then it may be able to change the relationship of HNCO/HCN and combustion temperature. One complicating factor in this analysis with HNCO and HCN concerns the assumption of HNCO and HCN being emitted via the same pyrolysis processes. If they have origins in different parts of the fuels burned, then this assumption would no longer be valid.

In summary, the similarity between both the $\Sigma NH_x/\Sigma NO_y$ relationship with both the HNCO fraction and with MCE suggests that combustion conditions and processes are driving some of the variability in the distribution of N_r in WE-CAN fires. Likewise, a similar amount of variability in $\Sigma NH_x/\Sigma NO_y$ explained by ΣN_r suggests that more N_r survives denitrification reactions at lower MCEs, and that the amount of fuel N volatilized may also contribute to the observed differences in $\Sigma NH_x/\Sigma NO_y$ across fires. These variables explain a larger fraction of the variability in $\Sigma NH_x/\Sigma NO_y$ than in NH_3/NO_x since $\Sigma NH_x/\Sigma NO_y$ accounts for much of the possible chemical evolution between emission and sampling (Figures 3.2 and A8). Other *in situ* data or metrics for specific fire characteristics such as burn temperature, burn geometry, and fuel moisture content are difficult to gather for complex wildfires like those sampled during WE-CAN. Attempts to relate satellite-derived fire radiative power estimates during the time of sampling to the ratio of $\Sigma NH_x/\Sigma NO_y$ do not yield any relationships (Figure A10a). Likewise, predicted 1000-hr fuel moisture at the time of the burn from GRIDMET (Abatzoglou 2011) (`www.climatologylab.org/gridmet.html`) is not correlated with the ratio of $\Sigma NH_x/\Sigma NO_y$ (Figure A10b).

Recent measurements of NVOCs in smoke have been made in laboratory burns (*e.g.* Gilman et al. 2015; Koss et al. 2018; Stockwell et al. 2015) and in the field (*e.g.* Coggon et al. 2016; Liu et al. 2017, , this study) via Proton-Transfer-Reaction Mass Spectrometry and chemical ionization time-of-flight mass spectrometry. NVOC EFs have been shown to depend on MCE (Coggon et al. 2016) and may be important for the formation of brown carbon and toxicity of wildfire smoke (Koss et al. 2018). In Figure A11, we show the calculated EFs of measured NVOCs summed over amide-, amine-, N-heterocyclic-, nitrile- (excluding CH_3CN), and nitroalkane- groups quantified for WE-CAN emissions transects by Permar et al. (in preparation), plotted against MCE. We observe negative correlations with MCE for all groups except the nitroalkanes.

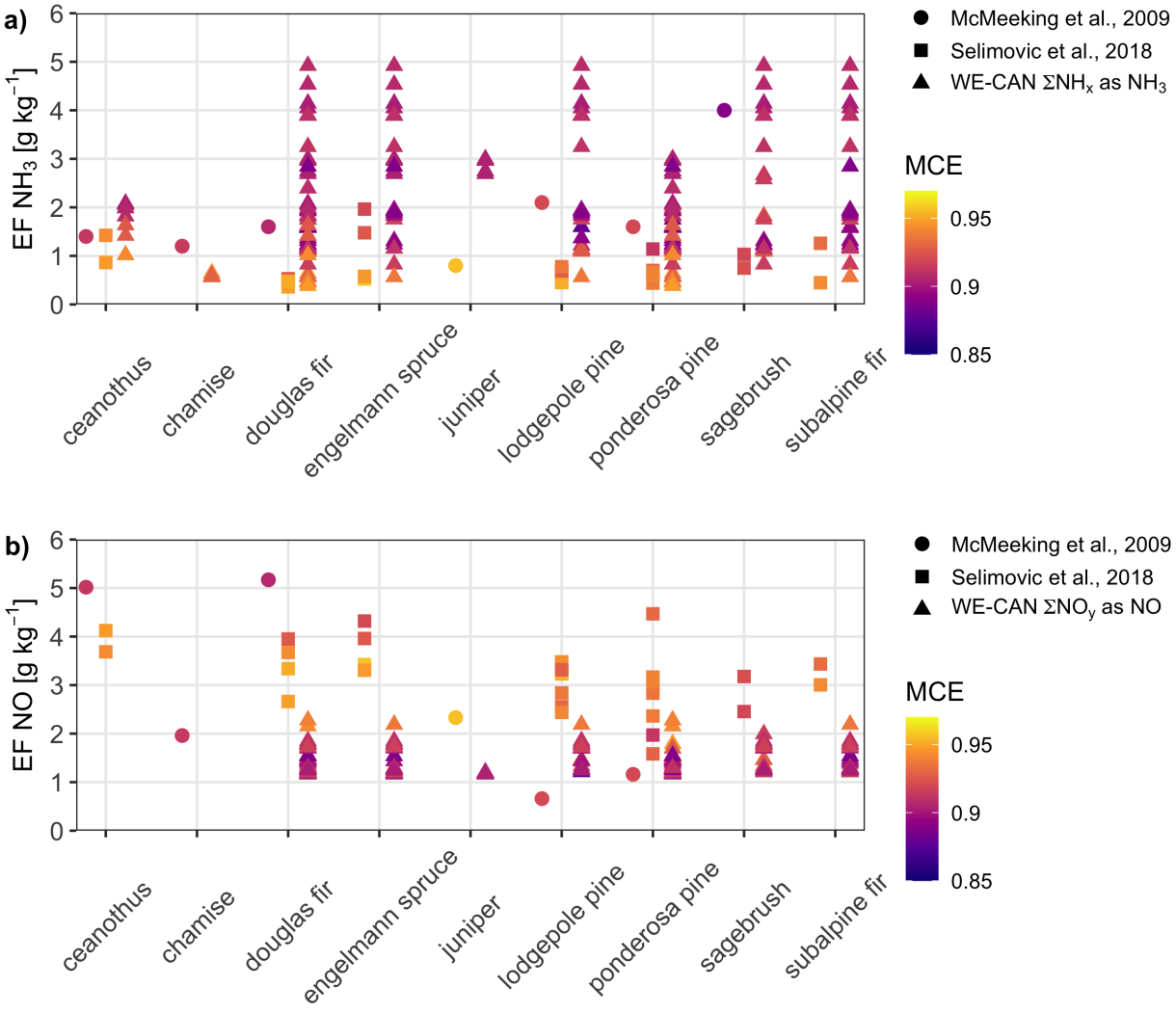

FIG. 3.3. Comparison between WE-CAN ΣNH_x and ΣNO_y emission factors to NH_3 and NO_x emission factors from FLAME-2 and FIREX-2016 lab studies. Colors indicate MCE.

3.3.3 Comparison to Laboratory Studies

We now compare WE-CAN field estimates of N_r emission factors to those measured in laboratory settings for similar fuel types. Several experiments have previously measured emissions from controlled burns of myriad fuel types in laboratories such as the Missoula Fire Lab. These emission factors are used to inform fire emission inputs into regional and global chemical transport models.

Using our calculated *in situ* emission factors, we match lab emission factors from specific fuel types to WE-CAN fires that included the same fuel type. Since all fires sampled by WE-CAN contained complex mixtures of fuels, estimates of the percentage of each fuel type burned are provided by the U.S. Forest Service. Most fires contained > 5 fuel types contributing significant percentages to the overall

area burned. Since we do not have a precise estimate of exactly which fuel(s) contributed to the smoke we sampled on a given fire, we include any fuel type with >10% contribution to the overall fuel burned for a given fire in this comparison. For example, several burns of ponderosa pine fuels were tested during the FIREX 2016 lab study (Selimovic et al. 2018), and any WE-CAN fire with >10% contribution from ponderosa pine is included in the comparison to those FIREX 2016 lab ponderosa pine burns. In this way, the same WE-CAN fire may be compared to several different specific fuel types burned in the lab.

Figure 3.3 shows the results of this comparison for NH_3 and NO_x with EFs from the FLAME-2 (McMeeking et al. 2009) and FIREX-2016 (Selimovic et al. 2018) laboratory studies. Both experiments burned a range of fuels and fuel types from across the western U.S. in the U.S. Forest Service Missoula Fire Sciences Laboratory. Here we again use WE-CAN ΣNH_x and ΣNO_y as proxies for NH_3 and NO_x at emission. We find that ΣNH_x EFs during WE-CAN for fires burning the same fuels as those burned in the lab are similar to or of a larger magnitude than the NH_3 lab EFs. Conversely, ΣNO_y EFs from WE-CAN are generally lower than NO_x EFs from the lab. Each emission factor is also colored by the burn average or emissions transect MCE. These sets of lab experiments largely represent higher MCEs than the WE-CAN data, but that is not always the case. Figure 3.3 indicates that WE-CAN EFs associated with higher MCEs are more closely comparable to the lab studies. Figure 3.4 shows the relationship between EFs and MCE across a wider range of previous studies applicable to western U.S. wildfires, without sorting by fuel type. We note that the error associated with our EF estimates is large, typically on the order of 30-40%. These same errors are applicable to Figures 4 and 6 as well, but displaying them would complicate the ease of understanding these figures. While the differences in burn conditions as captured by MCE between field and lab may offer one explanation for the difference between WE-CAN ΣNH_x and ΣNO_y EFs and the lab, another possible explanation for oxidized N is missing or uncertain NO_y measurements. The quantification of multifunctional organic nitrates and other oxidized N-containing NVOCs in the WE-CAN dataset is very uncertain. If these are present in higher quantities than we have estimated in smoke, and were directly or indirectly formed via reactions involving NO_x, then we could still underestimate the EFs of NO_x from WE-CAN by using the ΣNO_y EFs.

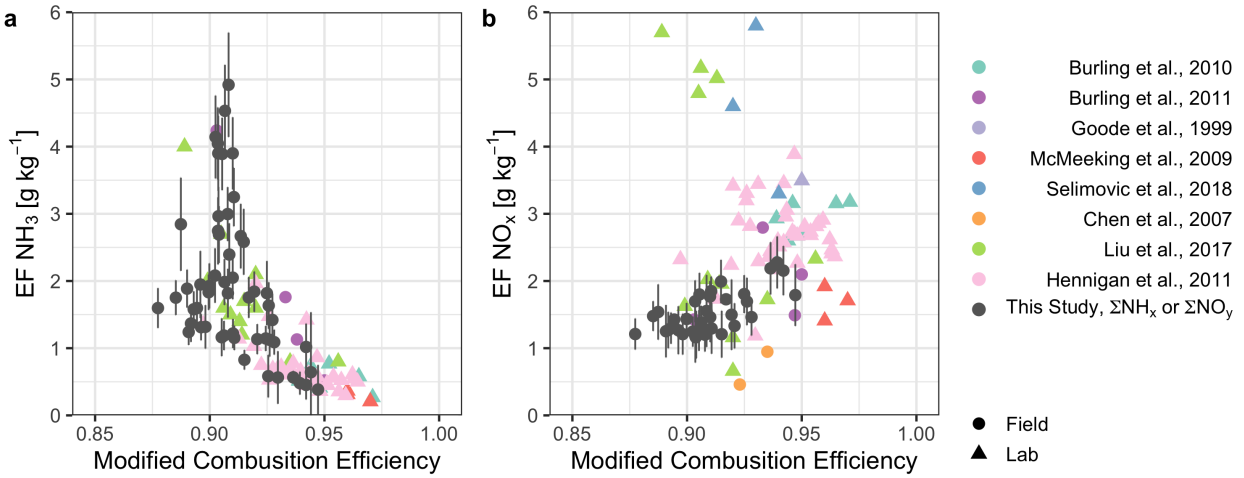

FIG. 3.4. Comparison of a) NH_3 and b) NO_x emissions factor relationships with MCE. WE-CAN data are in black with propagated uncertainties shown as vertical error bars, and literature data colored by study and with different shapes reflecting lab (triangle) or field measurements (circle) (literature data accessed from the SERA database: `https://depts.washington.edu/nwfire/sera/`).

We can also compare EFs from WE-CAN to those compiled in the literature for use in models by Akagi et al. (2011) and Andreae (2019) (Figure 3.5). Akagi et al. (2011) and Andreae (2019) both report EF factors for broad vegetation types with extratropical forest split between temperate and boreal forests. Since our fire locations were all within the lower 48 U.S. states, here we compare all WE-CAN EFs to their respective "Temperate Forest" best estimates. Figure 3.5 displays the ratio of WE-CAN emission factors for each transect to these literature best estimate values for temperature forests, with values greater than 1 indicating a WE-CAN transect EF estimate larger than that value and vice versa. The square points identify the median value across all of the WE-CAN emission transect estimates. Consistent with the previous comparisons, we find WE-CAN NH_3 and ΣNH_x EFs to be generally larger than the literature compilations, while NO_x and ΣNO_y EFs to be smaller. HCN, N_2O, and HONO EFs are also smaller, with large variability in the HONO emission factors (see Peng et al. 2020, , for more information), and CH_3CN is smaller than Akagi et al. (2011), and about the same as Andreae (2019). In our final comparison with laboratory measurements, we compare the NVOC EF estimates to the lab burn measurements of Koss et al. (2018) for nine species measured in common (Figure A12). We find general agreement in magnitude and the negative correlation between each NVOC and MCE between this study and Koss et al. (2018), though we note that the MCEs observed by Koss et al. (2018) were on average higher than those observed here.

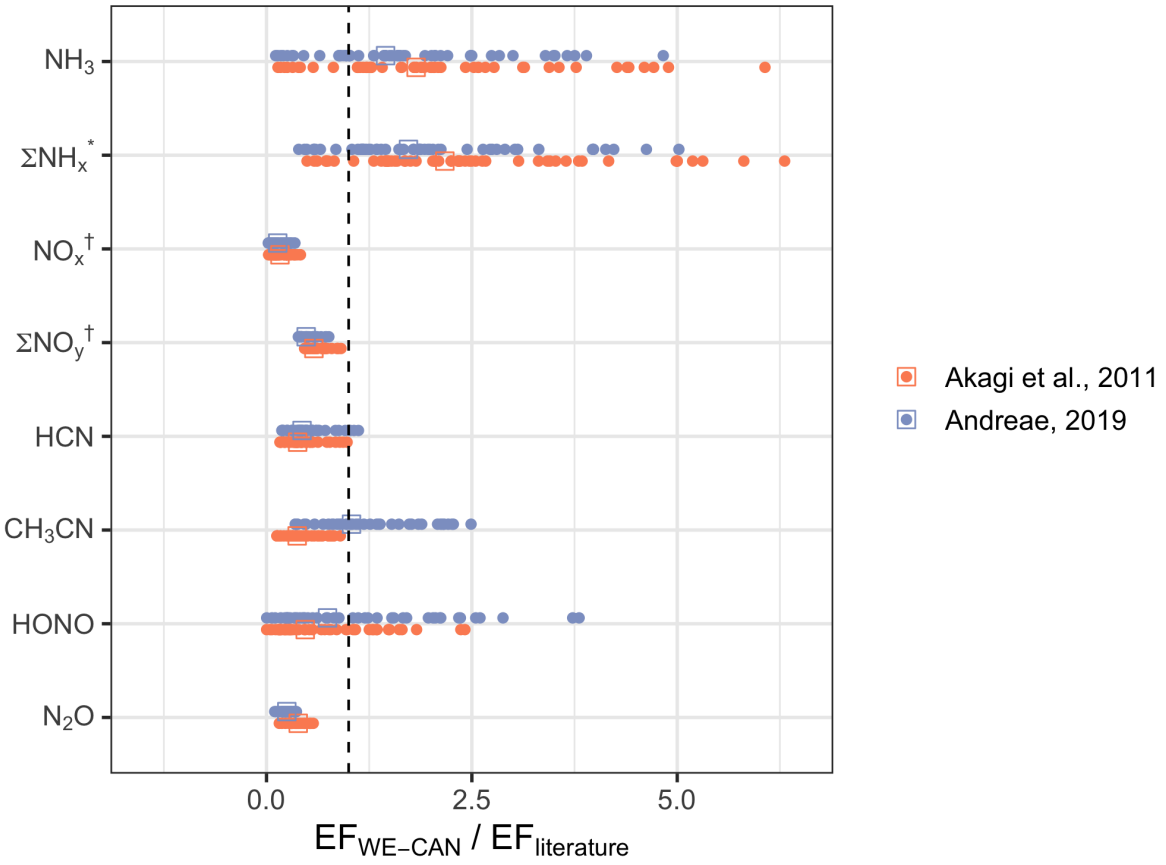

FIG. 3.5. Comparison between the ratio of different WE-CAN N_r EFs and the best estimate temperate forest EF for the same compound compiled in Akagi et al. (2011) (red dots) or Andreae (2019) (blue dots) for use in models. Square points indicate the median ratio across all WE-CAN emission transect estimates. * $EF_{WE\text{-}CAN}$ ΣNH_x is compared to the NH_3 $EF_{literature}$. † $EF_{WE\text{-}CAN}$ NO_x and ΣNO_y are compared to NO $EF_{literature}$.

3.4 SUMMARY AND CONCLUSIONS

The WE-CAN field campaign sampled smoke from 23 wildfires across the western U.S. during summer 2018. WE-CAN sampled fires of various sizes; most fires exceeded 1000 acres, and the eventual total burn area of several fires sampled during the WE-CAN campaign exceeded 100,000 acres. Sampling was conducted from the mid afternoon to early evening period. This means wildfires were primarily sampled during periods with well-developed vertical plumes, often during periods of rapid fire spread. We present NEMRs and EFs for a suite of N_r species calculated using these measurements. The three main conclusions from this work as are follows:

(1) We observe that reduced N species account for between 39 - 80% (median = 66%) of the total measured ΣN_r in fresh smoke plumes. Gas-phase NH_3 accounts for the majority of the

reduced N, with smaller contributions from $p\mathrm{NH_4}$, HCN, and HNCO. The largest contributors to oxidized N are $\mathrm{NO_x}$, $p\mathrm{NO_3}$, ΣONs, HONO, and PAN. As the primary WE-CAN sampling strategy was focused on large fires during periods with flaming fronts during mid-afternoon conditions, prior work might imply that oxidized $\mathrm{N_r}$ emissions (largely from flaming combustion) should dominate the total measured $\Sigma\mathrm{N_r}$. However, that is not what the WE-CAN data show.

(2) Within minutes after emission, rapid chemistry occurs that changes the distribution (species / amount / phase) of $\mathrm{N_r}$ in fresh smoke plume. Due to this rapid chemistry, we compare total $\Sigma\mathrm{NO_y}$ and measured $\Sigma\mathrm{NH_x}$ with common metrics of fire characteristics, such as MCE, rather than $\mathrm{NO_x}$ and $\mathrm{NH_3}$ by themselves. The ratio of $\Sigma\mathrm{NH_x}/\Sigma\mathrm{NO_y}$ generally decreases with increasing MCE, qualitatively consistent with previous research, and a similar relationship between $\Sigma\mathrm{NH_x}/\Sigma\mathrm{NO_y}$ and the HNCO fraction further suggest that combustion process and conditions drive some of the variability in the distribution of $\mathrm{N_r}$ between reduced and oxidized forms. Through the negative correlation between $\Sigma\mathrm{NH_x}/\Sigma\mathrm{NO_y}$ and the total measured $\Sigma\mathrm{N_r}$, we propose that fuel N content/volatilization differences between fires may also contribute to the observed variability in $\Sigma\mathrm{NH_x}/\Sigma\mathrm{NO_y}$, though this interpretation is complicated somewhat by unquantifiable influence from denitrification reactions ($\mathrm{N_r} \rightarrow \mathrm{N_2}$) that are likely more prevalent under more flaming combustion conditions.

(3) For similar fuel types the $\Sigma\mathrm{NH_x}$ EFs are of the same magnitude or larger than lab-based $\mathrm{NH_3}$ EFs, whereas $\Sigma\mathrm{NO_y}$ EFs are on average smaller than lab-based $\mathrm{NO_x}$ EFs. One possible explanation for the difference in $\Sigma\mathrm{NO_y}$ compared to lab $\mathrm{NO_x}$ is differences in the burn conditions between field and lab. WE-CAN sampled fires with MCEs between the median and lower limit of fires sampled previously and while WE-CAN EF estimates contain larger variability, the agreement with lab studies for $\Sigma\mathrm{NH_x}$ and $\mathrm{NH_3}$ EFs is better when only comparing across similar MCEs. Uncertain quantification of multifunctional organic nitrates and missing quantification of additional oxidized N-containing NVOCs in the WE-CAN dataset may be anotherr possible reason for this difference. If we consider all fuels sampled to be classified as temperate forest, we can also compare WE-CAN EFs to literature compilations of EFs for use in models.

CHAPTER 4

EMPIRICAL INSIGHTS INTO THE E-FOLDING TIMESCALES AND FATE OF AMMONIA IN WESTERN U.S. WILDFIRE SMOKE PLUMES[2]

4.1 INTRODUCTION

Wildfires are the largest natural terrestrial source of gas-phase ammonia (NH_3) to the atmosphere (Bouwman et al. 1997; Paulot et al. 2014) and these emissions may be growing in many regions of the world with increasing wildfire activity (*e.g.* Bray et al. 2018). NH_3 is the most abundant base in the atmosphere, and it can contribute to the formation of secondary inorganic (*e.g.* Behera and Sharma 2010; Yokelson et al. 2009) and organic (*e.g.* Liu et al. 2015) aerosol. This secondary aerosol has significant direct and indirect effects on the Earth's radiation budget, though the magnitude of these effects remains uncertain (Myhre et al. 2013; Paulot et al. 2017). NH_3 is a large fraction of the emitted reactive nitrogen (N_r) in wildfire smoke (Benedict et al. 2017; Roberts et al. 2020, ; Chapter 3) and can also be an important source of reactive nitrogen to sensitive ecosystems via deposition as the smoke travels downwind (Chen et al. 2014; Karlsson et al. 2013; Prenni et al. 2014).

The emissions of NH_3 from wildfires and the timescales of its fate in the atmosphere are both uncertain. Accurate and precise *in situ* measurements of gas-phase NH_3 are difficult due to its polarity and affinity for adsorption to surfaces (Pollack et al. 2019). Satellite retrievals of total column NH_3 hold promise for estimating emissions of NH_3 (Dammers et al. 2019), but efforts to infer emission factors from fires often rely on a prescribed value for the effective lifetime of NH_3 in smoke (Whitburn et al. 2015).

Few studies have empirically quantified the loss timescale of gas-phase NH_3 in biomass burning smoke plumes. Those that do most often call the estimated loss timescale a "lifetime" or "effective lifetime". However, the loss of gas-phase NH_3 is likely more complicated than a first-order exponential decay towards zero. Oxidation is very slow, deposition to the ground is usually negligible, and it is generally assumed that gas-phase NH_3 in smoke is lost by partitioning to the particle-phase via equilibrium-driven processes. These processes are dependent on T and RH and complicated by ongoing plume dilution and changing acid concentrations. Thus, while we report the estimated literature

[2]Adapted from a manuscript in preparation for *JGR Atmospheres*, June 2020

values in the same terms used by each analysis, we will employ the term "e-folding loss timescale towards quasi-equilibrium" , or "e-folding loss timescale" in our own analysis (Section 4.2.1). That said, Goode et al. (2000) observed an e-folding timescale of 2.5 hours in aircraft observations of an Alaskan boreal fire plume, Akagi et al. (2012a) estimated a lifetime of ~6 hours after observing NH_3 normalized excess mixing ratios decreasing by 50% over 4.5 hours of physical aging in aircraft measurements of a chaparral fire plume in California, and Adams et al. (2019) used the line density of IASI and CrIS satellite retrievals within 200 km of the Horse River wildfire in Canada to empirically estimate an NH_3 lifetime of 3 hours. In wildfire smoke further from the fire source however, four studies have inferred longer first-order or effective lifetimes of NH_3: 36-48 hours from correlation analysis of ground-based FTIR measurements Lutsch et al. (2016); 6-24 hours from regional analysis of IASI satellite retrievals over Russia R'Honi et al. (2013); 36 hours from a regional mass balance approach of IASI satellite retrievals over four tropical regions Whitburn et al. (2015); and 21 hours for an average effective lifetime in Indonesian peat fire plumes from IASI satellite retrievals Whitburn et al. (2016). The differences between the shorter observed lifetimes in fresh smoke and the longer lifetimes inferred by the ground- and satellite-based regional analyses could be due to more abundant reactants for gas-particle partitioning reactions in fresh smoke (Paulot et al. 2017) as well as changing equilibrium conditions as the smoke dilutes and is advected downwind.

It is difficult to precisely quantify the abundances of different NH_4 salts or reduced N compounds in smoke aerosol. *In situ* observations from aerosol mass spectrometers and Particle-into-Liquid samplers have inferred that ammonium nitrate (NH_4NO_3) is quickly formed (within minutes to hours) in smoke plumes based on the presence of both ammonium (NH_4^+) and nitrate (NO_3^-) fragments/species or ions (Akagi et al. 2012a; Yokelson et al. 2009; Alvarado et al. 2010; Liu et al. 2016; Hobbs et al. 2003; Kleinman et al. 2008). Abundant NH_3 in smoke accompanied by the oxidation of co-emitted nitrogen oxides (NO_x) is commonly assumed to lead to rapid association of NH_3 with nitric acid (HNO_3). However, several studies have acknowledged or offered evidence for the association of NH_3 with organic acids to form organic ammonium salts (Akagi et al. 2012a; Song et al. 2005). Other studies have reported enhancements of particulate ammonium and/or nitrate (pNH_4; pNO_3) in smoke but did not attribute these enhancements to specific causes or compounds (Hecobian et al. 2011; Benedict et al. 2017; Collier et al. 2016).

Given the present uncertainties in NH_3 evolution and the processes driving NH_3 aging in smoke, there is a need for additional empirical constraints on the e-folding loss timescale of NH_3 and its relationship with pNH_4 within wildfire smoke plumes (Paulot et al. 2017). Here, we use data from the 2018 Western Wildfire Experiment for Cloud Chemistry, Aerosol Absorption, and Nitrogen (WE-CAN) field campaign to derive empirical insights into NH_3 evolution in wildfire smoke. These data dramatically expand the number of fires for which NH_3 aging has been characterized. First, we estimate the e-folding loss timescales and distances of gas-phase NH_3 decreases with respect to gas-particle partitioning, as well as the e-folding loss timescales and distances with respect to dilution and partitioning. These loss timescales can be compared with the e-folding production timescale estimated from observed increases in pNH_4. Next, we explore the connection between NO_x oxidation chemistry and NH_3 aging, and investigate the conditions under which thermodynamic equilibrium may favor NH_4NO_3 formation. We find evidence of both inorganic and organic pNH_4 in our data. Lastly, we calculate the fraction of pNH_4 and pNO_3 in older smoke and find an anti-correlation with temperature for both, suggesting the smoke plume injection heights and transport pathways influence gas-particle partitioning of NH_3 through the abundance and equilibrium of NH_4NO_3.

4.2 Methods specific to this analysis

4.2.1 Exponential Fitting of Empirical Relationships

We calculate first-order exponential decay towards a quasi-equilibrium value (Equation 4.1) and asymptotic growth (inverse exponential decay; Equation 4.2) equations to fit the change in calculated NH_3 and pNH_4 NEMRs respectively with estimated plume age (nls and SSasymp functions: R software, package "stats", v3.5.1). These equations are fit separately to the NEMRs for each species and set of plume transects. The estimated timescale with respect to loss or production is the inverse of the exponential coefficient, $\tau = \frac{1}{k}$. Here, we call τ the e-folding loss (production) timescale. A first-order exponential decay to zero equation (Equation 4.3) is also fit to the enhancement mixing ratios above background of NH_3 and CO for each set of plume transects. The inverse of the exponential coefficient, $\tau = \frac{1}{k}$, of these fits is an estimate of the e-folding timescales (or distances if fit using the distance from the fire) with respect to dilution plus chemistry (NH_3), and just dilution (CO).

$$y = y_{\text{asymptote}} + \left(y_0 - y_{\text{asymptote}}\right) * e^{-k*x} \tag{4.1}$$

$$y = y_{\text{asymptote}} * \left(1 - e^{-k*x}\right) \tag{4.2}$$

$$y = y_0 * e^{-k*x} \tag{4.3}$$

Because we did not sample the plumes exactly at the emission source (t_0), we make one important assumption about the NH_3 and pNH_4 NEMR fits. All NH_3 and pNH_4 is assumed to be in the form of gas-phase NH_3 at emission. Accordingly, a calculated NH_3 NEMR data point of magnitude NH_3 NEMR + pNH_4 NEMR from the closest transect to the fire is added at t_0 and used in calculating the e-folding loss timescale of NH_3 NEMR for each plume. Likewise a pNH_4 NEMR point of magnitude zero is added at t_0 and used in the calculation of the pNH_4 NEMR e-folding growth timescale. With this assumption, we are able to estimate the rate of rapid partitioning often occurring in the minutes before the aircraft was able to sample the plume.

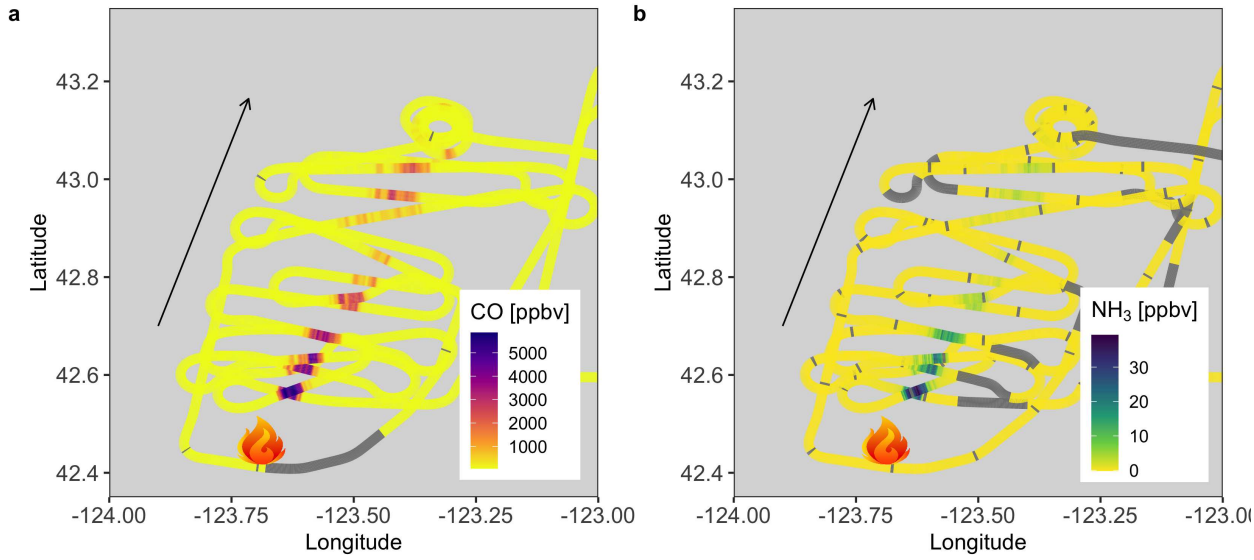

FIG. 4.1. NCAR/NSF C-130 flight track around the Taylor Creek Fire, 30 July 2018 during Research Flight 3 (RF03), colored by (a) CO and (b) NH_3 mixing ratios. The black arrow shows the average wind direction and the fire icon shows the fire location. Grey periods in the flight track indicate calibration and/or instrument zero periods or other periodical instrument checks.

4.3 RESULTS AND DISCUSSION

Figure 4.1 shows the sampling pattern downwind of the Taylor Creek Fire sampled on 30 July 2018 during RF03. The flight track is colored by CO (4.1a) and NH_3 (4.1b) mixing ratios with darker colors indicating the plume core as the aircraft transited the smoke plume. Transects further downwind

contained progressively less CO (evidence of dilution) and NH_3 (evidence of dilution plus chemistry). The Taylor Creek Fire plume was a discrete plume that was injected above the boundary layer and entrained into the free-tropospheric flow. This fire afforded the best opportunity to sample a "Gaussian-dispersing" plume using a pseudo-Lagrangian flight pattern. The estimated emission times (t_0, described in section 2.2.5) for most of the individual plume transects shown in Figure 4.1 are within 1 hour (during a several-hour flight time), indicating the pseudo-Lagrangian sampling was effective. We have identified 7 other cases of pseudo-Lagrangian sampling where the estimated emission times from individual passes were within ~2 hours of each other. The Bear Trap Fire (9 August 2018; RF09) plume was sampled with two separate pseudo-Lagrangian patterns and the South Sugarloaf Fire (26 August 2018; RF15) plume was sampled at multiple altitudes at each distance downwind. These cases were separated and kept distinct for this analysis. Thus, the 8 pseudo-Lagrangian sampling cases correspond to 6 individual fires.

Measurements of gas-phase NH_3 and aerosol species such as pNH_4 from the AMS are tightly correlated with CO in fresh and old smoke in the WE-CAN dataset; and NH_3enhancements above background reached > 400 ppbv in fresh smoke. Distinct enhancements of NH_3 of > 1 ppbv are generally present even in old smoke (Figure A14a), while detectable background mixing ratios of ~0.2 - 1 ppbv are present in the clean free troposphere.

Figure 4.2 shows the evolution of dilution-corrected gas-phase NH_3, pNH_4, and the sum of NH_3 and pNH_4, ΣNH_x. While 6 out of the 8 plumes are observed to lose NH_3 with physical aging, both altitudes of the South Sugarloaf plume maintain roughly constant NH_3 NEMRs and pNH_4 NEMRs appear to increase. If all the NH_3 lost from the gas-phase partitions to the aerosol, in a perfectly Lagrangian-sampled plume we would expect ΣNH_x to remain constant after correcting for dilution. When viewed this way, we observe steady or slightly decreasing ΣNH_x NEMRs with estimated physical age for all fires with the exception of South Sugarloaf. Several of the apparent decreases are within the propagated uncertainty of the measurements and NEMR calculations. Background errors become larger as the plume dilutes and enhancements above background are less pronounced. However, the decrease in the Bear Trap smoke plume is outside the propagated uncertainty, and represents ~ 40% loss of ΣNH_x over ~4 hours of physical aging. Likely explanations for "missing" ΣNH_x include partitioning of NH_3 to smaller (*e.g.* recently nucleated) particles than the size range captured by the AMS (70 - 1000 nm). NH_3 is not likely removed from plumes sampled in the upper boundary layer/free troposphere by deposition

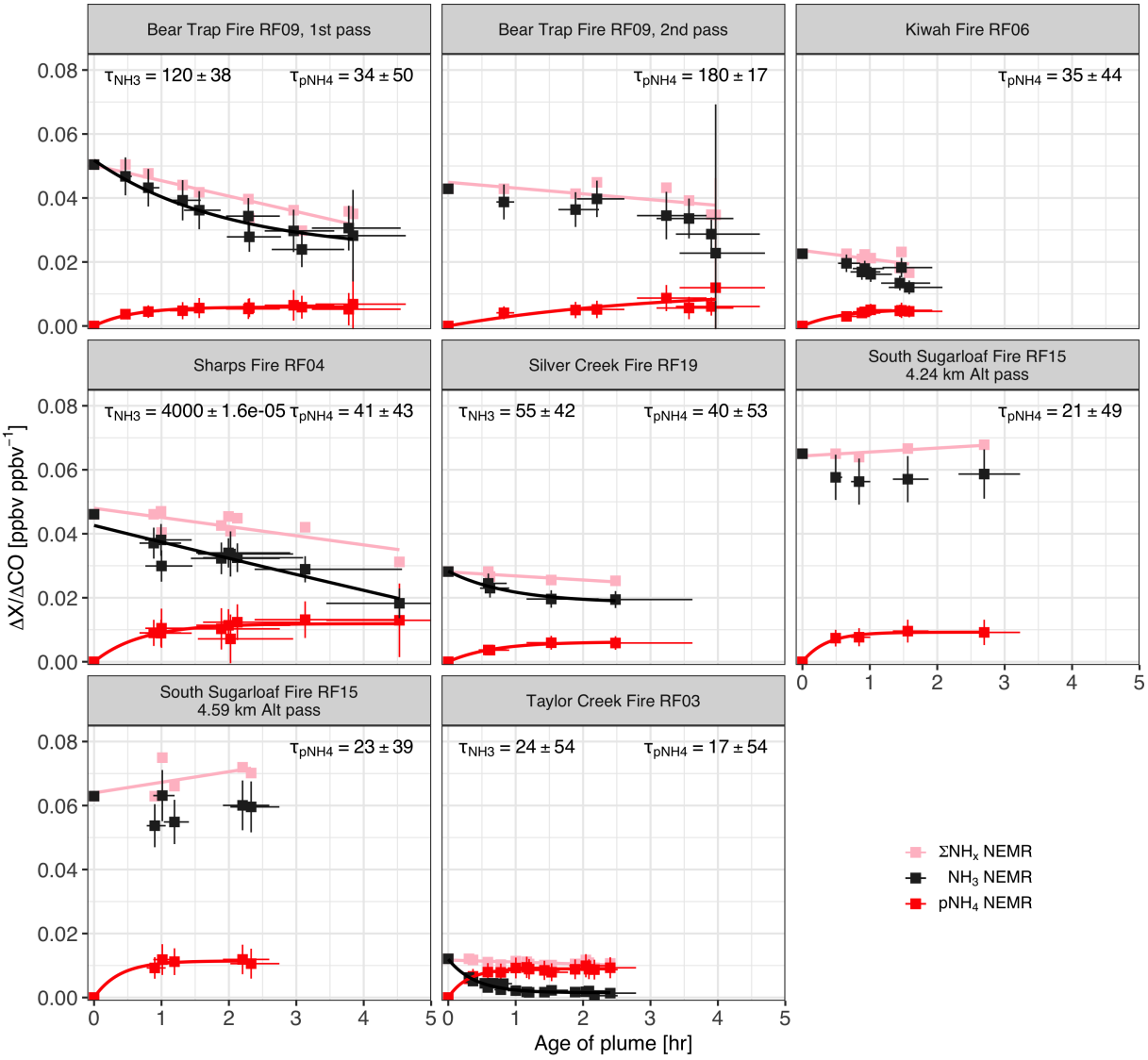

FIG. 4.2. Evolution of NH_3 and pNH_4 NEMRs with estimated physical plume age. The sum of NH_3 and pNH_4 is shown in pink points, NH_3 is in black, and pNH_4 is shown in red, with empirical fits plotted as lines. Empirical fits are an exponential decay to a quasi-equilibrium value for NH_3, and an asymptotic increase (inverse exponential decay) for pNH_4. τ_{NH3} and τ_{pNH4} represent the estimated e-folding time with respect to chemical losses and chemical production respectively, $\pm$ 1σ standard deviation in minutes. No estimate for the e-folding time is shown if the fit did not converge.

during our timescales of interest (*e.g.* Akagi et al. 2012a), nor via oxidation by OH, given the lifetime of NH_3 against oxidation by OH is ~14 days ($k = 1.6\times 10^{-13}$ cm^3 molec.$^{-1}$ s^{-1}; Sander et al. 2006).

NH_3 partitioning fractions in these plumes sampled during WE-CAN span a wide range. After 1.5 hours, the plumes included here ranged from pNH_4 fractions of 0.2 - 0.9 (pNH_4 fraction = $pNH_4/\Sigma NH_x$). This is a wider range than described in the limited existing literature covering plumes that have been

sampled as they age. In the two comparable examples, Akagi et al. (2012a) observed a $p\mathrm{NH}_4$ fraction of 0.13 after 1.5 hours of aging in a southern California chaparral fire, and Yokelson et al. (2009) observed a $p\mathrm{NH}_4$ fraction of ~0.32 after 1 hour of aging in tropical Yucatan Peninsula smoke plumes.

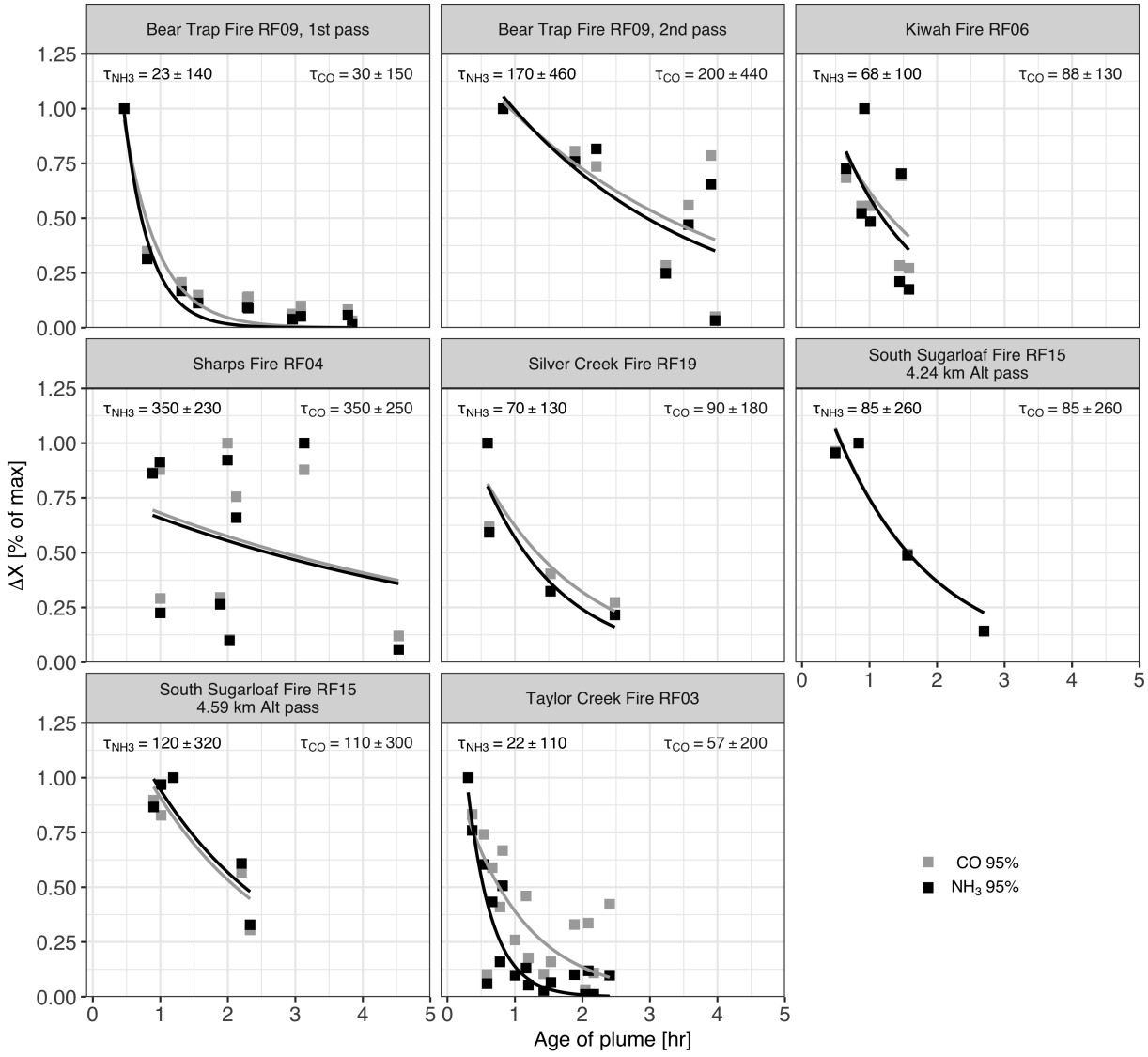

FIG. 4.3. Evolution of NH_3 and CO mixing ratios with estimated physical plume age. Points plotted are the mean mixing ratio of NH_3 in black and CO in grey of each plume transect, minus the estimated background and normalized by the greatest value across all passes in that plume (usually the youngest plume transect). τ_{NH3} and τ_{CO} represent the estimated e-folding time with respect to dilution + chemical losses with 1σ standard deviation in minutes, calculated for a first-order exponential decay to zero.

We assume the loss of NH_3 from the gas-phase to follow a first order exponential decay towards a quasi-equilibrium value greater than zero. Our observations in older smoke show continued NH_3 enhancements (Figure A14a) and so an exponential decay towards 0 would not make sense, nor does it make sense from a thermodynamic point of view if NH_4NO_3 is present in the aerosol phase. Because we are fitting both an e-folding loss timescale as well as a quasi-equilibrium asymptote, our fits converge in only 4 out of the 8 plumes. The estimated e-folding loss timescale of NH_3, τ_{NH3}, in these 4 plumes is between ~24 - 4000 minutes (median of 55 minutes), with the Sharps Fire plume a possible outlier. As Figure 4.3 shows, the Sharps Fire plume as sampled did not behave similar to a gaussian-dispersing plume (with exponentially decaying CO enhancements). The flight scientist during that flight noted that at certain points it appeared as if smoke from a previous day of burning was being lifted out of the valley into the free troposphere. While we excluded transects with clear evidence of this influence from the current analysis, and the transects kept in meet the t_0 emission time criteria, the Sharps Fire plume likely represents an unideal case from which to estimate the timescale of gas-phase NH_3 loss. Timescales in the most well-defined plumes, Bear Trap 1st Pass and Taylor Creek, were estimated to be 120 ±38 and 24 ±54 minutes, respectively. The e-folding timescale of the average mixing ratio enhancements (i.e., not dilution corrected) of NH_3 and CO are shown in Figure 4.3. We observe e-folding timescales of NH_3 with respect to dilution plus chemical losses that range from 22 - 350 minutes (median of 77 minutes), generally shorter for a given plume than the timescales with respect to chemical losses only. E-folding distances range between 12 - 130 km (Figure A15) and could be useful in future satellite analyses and comparisons.

We also fit an asymptotic growth curve (the inverse of an exponential decay) to the pNH$_4$ NEMR estimates for each fire (Figure 4.2). The presence of pNH$_4$ in the downwind transect nearest to each fire suggests that a large fraction of the partitioning of gas-phase NH_3 into the aerosol happens on a timescale of tens of minutes between emission and the first *in situ* sampling transect. As we note above, the succeeding increase in pNH$_4$ is enough to balance the loss of gas-phase NH_3 within measurement errors for many fires. Over the short time span represented by these data (0 - 4 hours of physical transport), in some cases, pNH$_4$ NEMRs continue to increase as the plume ages, while in other cases the pNH$_4$ NEMR appears to stabilize. The e-folding timescales of the asymptotic growth in pNH$_4$ range from 17 - 180 minutes, with Bear Trap 1st Pass and Taylor Creek plumes estimates of 34 ± 50 and 17 ± 53 minutes, respectively.

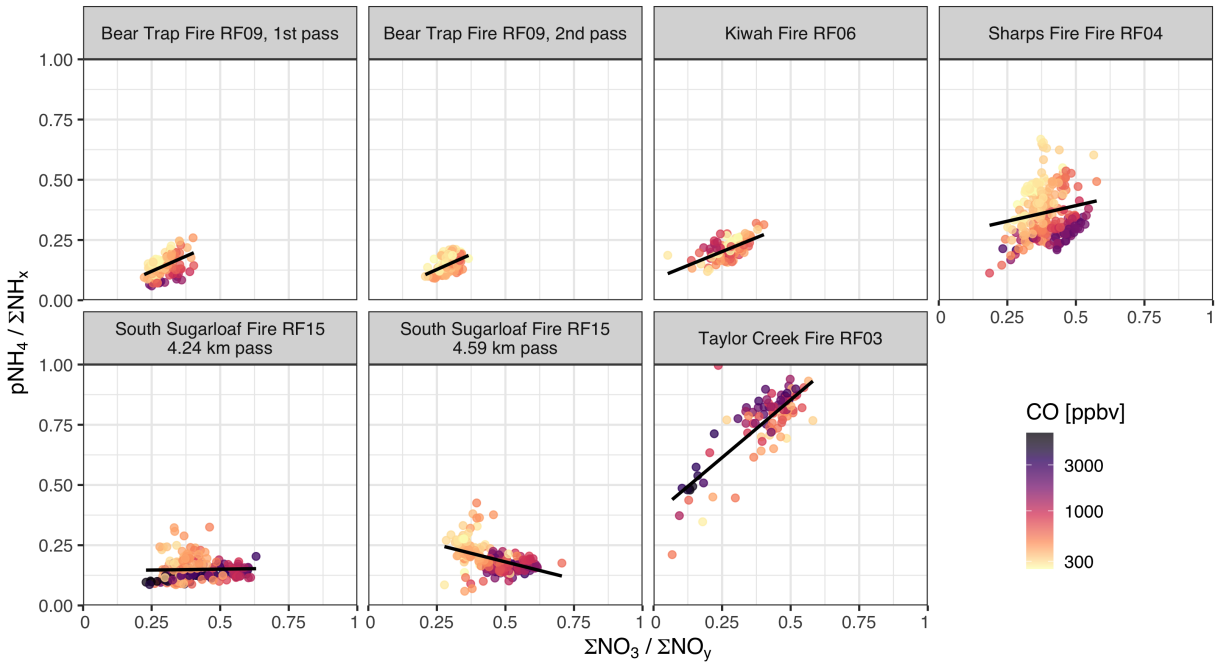

FIG. 4.4. Relationship between the fraction of $p\mathrm{NH_4}$ out of total ammonia ($\Sigma\mathrm{NH_x}$= $\mathrm{NH_3}$ + $p\mathrm{NH_4}$) and the fraction of more oxidized nitrogen species ($\Sigma\mathrm{NO_z}$ = PAN + PPN + $\mathrm{HNO_3}$ + $p\mathrm{NO_3}$) out of total reactive nitrogen oxides ($\Sigma\mathrm{NO_y}$ = $\mathrm{NO_x}$ + HONO + PAN + PPN + $\mathrm{HNO_3}$ + $p\mathrm{NO_3}$). All observations are averaged according to the 5 second timebase for measurements collected by the AMS. Black lines represent linear least squares regression of the data points. Data points are colored by CO mixing ratio for all measurements above 250 ppbv.

$\mathrm{NH_3}$ partitioning to aerosol can end up in three forms. $\mathrm{NH_3}$ can form inorganic salts with nitrate, sulfate, or other inorganic species (Seinfeld and Pandis 2016). It can form salts with organic acids (Malm et al. 2005; Akagi et al. 2012a) or react with some organic compounds (*e.g.* some carbonyls) to form nitrogen-containing organic compounds (Updyke et al. 2012; Laskin et al. 2015; Liu et al. 2015). It can also dissolve into solution and exist as an ammonium ion if a liquid phase exists in the aerosol (Seinfeld and Pandis 2016). AMS $p\mathrm{NH_4}$ should capture each of these forms, as well as amines or other reduced N groups that fragment as $\mathrm{NH_4}$ and have already partitioned to the particle-phase. However, based on the PTR-ToF-MS measurements, gas-phase amines are <5% of gas phase $\mathrm{NH_3}$ across all WE-CAN smoke plumes when they were intercepted (Chapter 3), so it is likely that the contribution to the observed increase in $p\mathrm{NH_4}$ during the pseudo-Lagrangian sampling from amines or other reduced N components is small.

If oxidized nitrogen chemistry is linked to (or indicative of) the partitioning of $\mathrm{NH_3}$ to the aerosol through the formation of $\mathrm{NH_4NO_3}$, we would expect a positive relationship between the fraction of

ΣNH_x that is pNH_4 and the fraction of the sum measured oxidized nitrogen ($\Sigma NO_y = NO_x + HONO + PAN + PPN + HNO_3 + pNO_3$) that is NO_z ($\Sigma NO_z = PAN + PPN + HNO_3 + pNO_3$). This relationship is shown in Figure 4.4 for each plume where all data are available. Fresh plumes start with lower quantities of $pNH_4/\Sigma NH_x$ and $\Sigma NO_z/\Sigma NO_y$ and both quantities increase as the plume ages. The $\Sigma NO_z/\Sigma NO_y$ fraction is qualitatively similar to the negative log of NO_x fraction proxy for chemical age used in previous studies of wildfire smoke (Kleinman et al. 2008; Sedlacek III et al. 2018), and an increase in this fraction with aging reflects the transformation of NO_x into more highly oxidized products such as PAN, HNO_3, and organic nitrates. As this chemistry proceeds, partitioning of NH_3 into pNH_4 is also occurring, whether via the formation of inorganic salts or through NH_3-organic reactions. Figure 4.4 demonstrates three important patterns. First, for most plumes, ΣNO_z is more than 50% of ΣNO_y. This is the case for even the first transect of the smoke plumes shown in Figure 4.4 and is a result of rapid oxidation of NO_x in the first tens of minutes after emission (Peng et al. 2020, ; Juncosa Calahorrano et al., in preparation). Second, the pNH_4 fraction ranges widely between 0.1 - 0.9. The Taylor Creek Fire plume is an obvious outlier, with a pNH_4 fraction $> \sim 0.5$ even in the freshest plume transects. There is evidence that Taylor Creek was a particularly chemically active plume, with high NO_x and HONO emission factors (Chapter 3 Peng et al. 2020), the highest estimated NO_x relative to NH_3 (NO_x/NH_3 ratio) of any fire (Chapter 3), and more rapid O_3 production than any other plume sampled. Third, smaller CO mixing ratios at higher pNH_4 fractions in the South Sugarloaf and Sharps Fire plumes suggest that under some circumstances more dilute smoke (either plume edges or physically older smoke) partitions a higher fraction of NH_3 into the aerosol phase for a given fraction of NO_z.

Concurrent work by Juncosa Calahorrano et al. (in preparation) estimates HNO_3 formation from the OH oxidation of NO_2 in the Bear Trap and Taylor Creek fire plumes. Assuming all produced HNO_3 partitions to the aerosol phase in association with NH_3, they find that NO_2 oxidation by OH can account for $\sim$100% of the pNO_3 formation in the Taylor Creek plume, and $\sim$300% of the pNO_3 formation in Bear Trap. Possible reasons for the overestimation of pNO_3 increases could include an incomplete understanding of OH concentration evolution and uptake of HNO_3 by super-micron particles. These rough estimates support the conclusion that the partitioning of NH_3 into the aerosol phase is at least in part due to the formation of NH_4NO_3 through the association with gas-phase HNO_3.

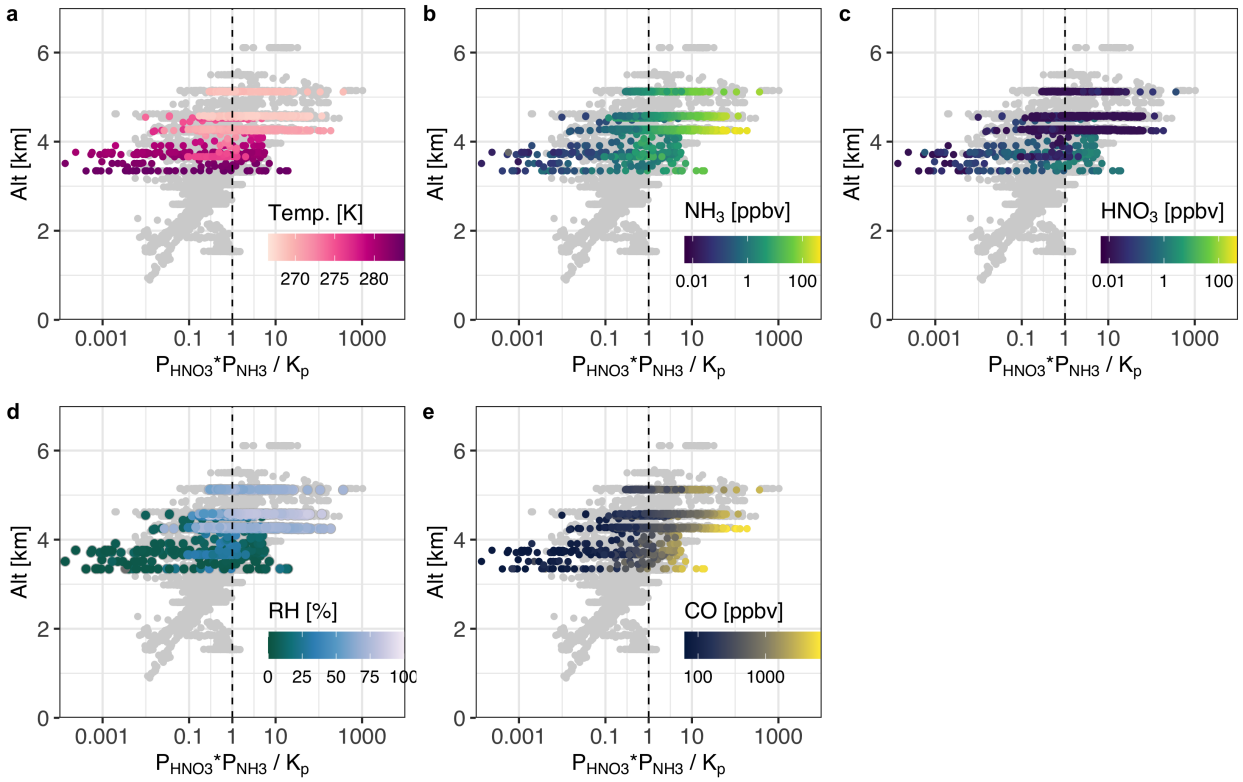

FIG. 4.5. The altitude dependence of the ratio of the product of NH_3 and HNO_3 partial pressures with the dry dissociation constant for NH_4NO_3, K_p. All points are averaged measurements on the AMS timebase (5 seconds). Grey points show all measurements within identified smoke plumes throughout the campaign. Colored points are those from the 8 fire plumes included in prior figures. Each panel is colored by a different measurement: a) ambient temperature, b) NH_3 mixing ratio, c) HNO_3 mixing ratio, d) ambient relative humidity, and e) CO mixing ratio. The vertical dashed line in each panel indicates a K_p ratio of 1.

To investigate the thermodynamics of possible NH_4NO_3 formation within WE-CAN smoke plumes, we calculate the dissociation constant of NH_4NO_3, K_p (Table 10.7 in Seinfeld and Pandis 2016), and compare it to the product of partial pressures of gas-phase NH_3 and HNO_3 (Figure 4.5). K_p is dependent on temperature (Figure 4.5a) (see also Stelson and Seinfeld 1982), and it indicates whether a parcel is supersaturated with respect to NH_4NO_3 when particles are dry (which assumes a low environmental relative humidity and particles have not deliquesced). This K_p formulation does not consider physical and chemical properties of the smoke aerosol that may shift particles away from NH_4NO_3 equilibrium such as mixing state, phase separation, and aerosol pH (*e.g.* Kanakidou et al. 2005; Guo et al. 2018). Higher relative humidities (typically > 60 %) will likely cause NH_4NO_3-containing aerosol to deliquesce at the temperatures sampled here, increasing the likelihood of additional NH_4NO_3 formation. 63% of samples had RH < 60 % in the data shown in Figure 4.5d, and for simplicity we always assume the

aerosol is dry. When the product of NH_3 and HNO_3 partial pressures is greater than K_p, or a ratio > 1 (vertical dashed lines in Figure 4.5), the parcel is assumed to be NH_4NO_3 supersaturated, and NH_4NO_3 will form as the system moves towards thermodynamic equilibrium. Conversely a K_p ratio < 1 indicates the parcel is NH_4NO_3 subsaturated and NH_4NO_3 in aerosol, if it exists, will start to dissociate and transition back into the gas-phase as the system moves towards equilibrium.

Figure 4.5 shows that NH_4NO_3 supersaturation (points to the right of the vertical dashed lines) is more likely in higher altitude plumes because the temperature dependence of K_p pushes partitioning of NH_4NO_3 toward the particle phase, as inferred by Paulot et al. (2017). Individual data points in the plumes sampled during WE-CAN span a wide range of K_p ratios, from 0.001 to 1000; low values are driven by low NH_3 and HNO_3 mixing ratios and warmer temperatures (Figures 4.5a, b, c), and high values are driven by high NH_3 mixing ratios and colder temperatures. The total amount of available NH_3 and HNO_3 drives the relative amount of possible NH_4NO_3 formed, assuming there are no other physical or chemical constraints to the systems' equilibrium, and under this assumption the large range of observed K_p ratios indicates that the smoke is not often near NH_4NO_3 equilibrium. It is possible these observations of K_p ratios far out of equilibrium could constitute evidence for the influence of different physical and chemical properties mentioned above. Garofalo et al. (2019) showed that submicron aerosol measured during WE-CAN were generally > 85% organic, and thus it is likely many bulk properties are dominated by organic compounds.

NH_3 is nearly always in excess in these plumes, particularly when the K_p ratio is > 1, and thus HNO_3 may be a limiting factor in the formation of NH_4NO_3 (Figures 4.5b and c). Gas-phase HNO_3 enhancements were not observed or they were small (typically < 5 ppbv; Figure A14b) compared to tens or hundreds of ppbv in observed NH_3 mixing ratios (Figure A14a), implying that NH_4NO_3 formation is HNO_3 limited. NH_4NO_3 supersaturation is also more common in fresher denser plumes (Figure 4.5e), where appreciable quantities of HNO_3 have sometimes been produced (Figure 4.5c) and before dilution reduces the total abundances of both NH_3 and HNO_3.

As stated earlier, the pNH_4 measurement in smoke may contain contributions from inorganic NH_4 salts with inorganic acid anions, organic NH_4 salts from the association of NH_3 with organic acids (*e.g.* Akagi et al. 2012a), and fragments of reduced organic N such as amines or other covalently bonded reduced organic nitrogen compounds (*e.g.* Farmer et al. 2010; Lin et al. 2016). Thus, we have good reason to expect that not all the pNH_4 measured in smoke is inorganic (i.e., NH_4^+ associated with NO_3^- or

SO_4^{2-}). There were two measurements of aerosol composition on board the C-130 measuring molecular fragments via mass spectrometry (AMS) and ions present via ion chromatography (PILS) that might enable us to test this assertion. However, it is difficult to directly use both the PILS and AMS aerosol composition measurements due to the large difference in sampling period (2 minutes versus 5 seconds respectively), particularly considering that smoke plumes are very heterogeneous and highly variable. Additionally, measurements we might expect to compare well on a 2 minute average basis, such as inorganic chloride (PILS Cl^- and AMS *p*Cl) generally differ by 1-3 orders of magnitude in dense smoke (PILS $Cl^- <$ AMS *p*Cl), and the timeseries for PILS data do not correlate well with either the AMS data or CO. This unresolved difference could possibly be due to aerosol morphology, mixing state, and composition (e.g. organic coatings, tar balls etc.) affecting transmission and detection differently in each instrument, as well as the fact that the instruments were on different inlets on the aircraft. Work attempting to understand these differences is ongoing. That said, we can compare between the self-consistent measured PILS ions to answer the question, are organic acids present in smoke aerosol, and are they abundant enough for us to reasonably assume the presence of ammonium salts of organic acid anions? We find that the fraction of charge-weighted sum organic acid ion mixing ratio equivalents ($\sum$ formate, acetate, 2∗oxalate, 2∗malonate, 2∗succinate, and 2∗glutarate) is often greater than the abundance of the NH_4^+ ion in the PILS measurements that overlap with identified smoke plumes. This indicates that organic acids are present in the sampled aerosol and that they are present at sufficient levels for us to assume that NH_4-organic salts may exist in the plumes sampled. This conclusion is consistent with the enrichment of organic acids and NH_4^+ observed in boreal forest fire smoke (Talbot et al. 1992) and tropical Amazon biomass burning haze (Andreae et al. 1988), though we note that smoke in these studies was estimated to be older than the fresh smoke measurements analyzed here.

Further work is needed to estimate the quantify the fraction of inorganic versus organic NH_4 salts, as well as to investigate the possibility contribution of covalently bonded reduced N (C_xH_yN such as amines or NH_4-organic compounds) to the *p*NH_4 measurement. Empirical AMS fragment apportioning analyses for *p*NH_4 during WE-CAN are ongoing, but the diversity of species present in smoke aerosol complicates separation of inorganic *p*NH_4 from organic *p*NH_4. Ion balance methods using the AMS measurements are complicated by the fact that both *p*SO_4 and *p*NO_3 likely have inorganic and organic contributions (Farmer et al. 2010; Chen et al. 2019). Additionally, the AMS generally measures the non-refractory component of potassium (K) and thus we do not report K mass. We expect refractory K to be present in wildfire smoke submicron aerosol (Li et al. 2003; McMeeking et al. 2009;

Levin et al. 2010), and we see considerable K^+ in the PILS observations. Therefore, since K would likely be associated with some fraction of the inorganic anions, and some fraction of both $p\mathrm{SO}_4$ and $p\mathrm{NO}_3$ may be organic, calculating the inorganic $p\mathrm{NH}_4$ fraction of total $p\mathrm{NH}_4$ from an ion balance is difficult. Thermodynamic modeling efforts may likewise suffer from the same constraints, and while it may be needed to assist in answering these questions, it is outside the scope of the current analysis. In summary, the PILS ion measurements suggest that NH_4-organic salts are likely present in western wildfire smoke plumes, and future work is needed to estimate the relative abundance of these NH_4-organic salts as well as the relative contribution of reduced organic N to the measured $p\mathrm{NH}_4$.

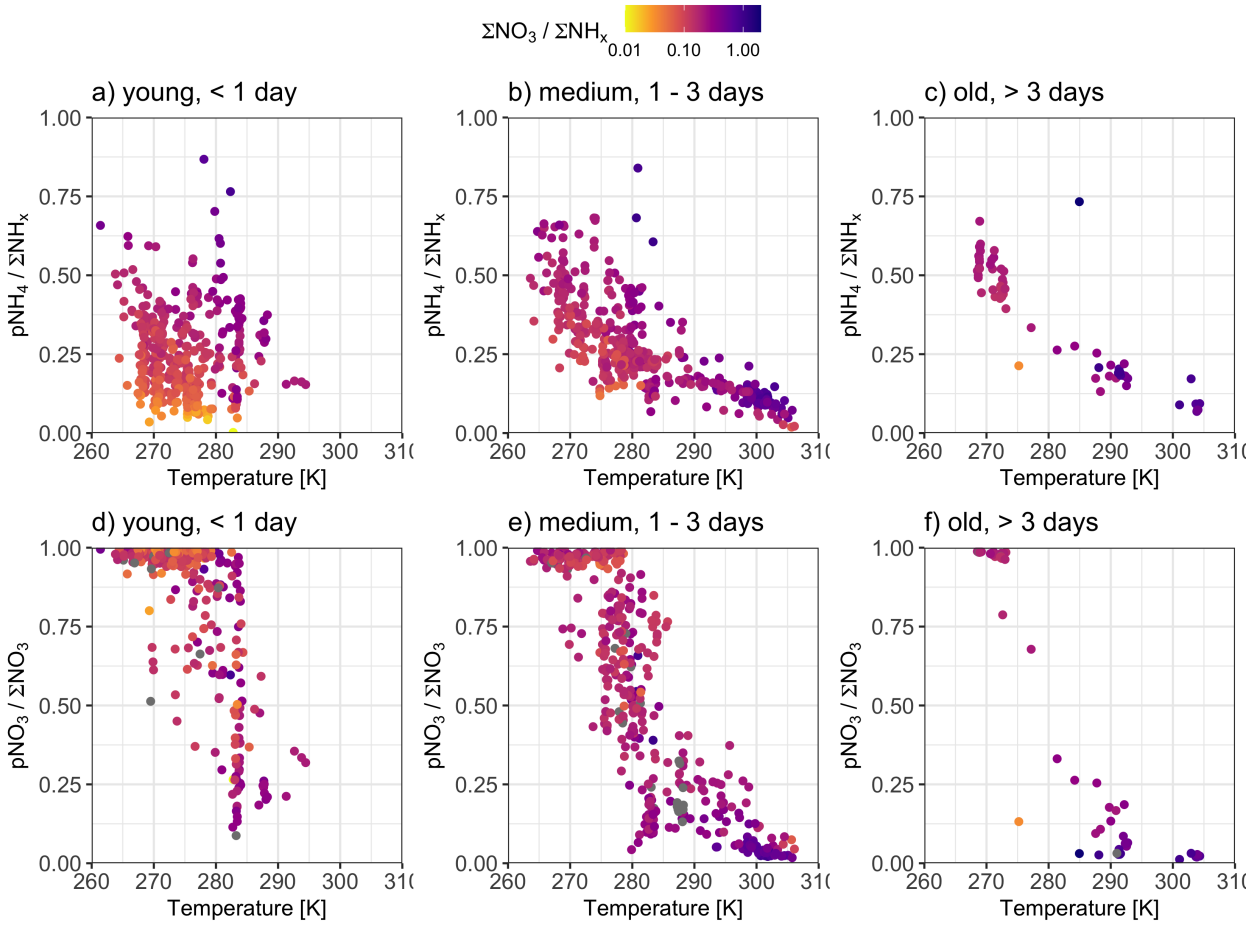

FIG. 4.6. (a-c) Measured $p\mathrm{NH}_4$ fraction ($p\mathrm{NH}_4/\Sigma\mathrm{NH}_x$) as a function of temperature, binned by young, medium, and old smoke, as defined by chemical age estimates from O'Dell et al. (in preparation). (d-f) Measured $p\mathrm{NO}_3$ fraction ($p\mathrm{NO}_3/\Sigma\mathrm{NO}_3$; $\Sigma\mathrm{NO}_3 = p\mathrm{NO}_3 + \mathrm{HNO}_3$) as a function of temperature, binned by the same chemical age estimates. Observations are averaged to the timebase of the TOGA instrument (approximately 30-second samples every 100 seconds) and colored by the ratio of measured sum nitrate to measured sum ammonia ($\Sigma\mathrm{NO}_3/\Sigma\mathrm{NH}_x$) on a $\log_{10}$ scale. Data points include only the observations collected > 2 km above sea level in order to limit ground-based emission influence, and are not background-corrected.

While Figure 4.5 shows the physical and chemical context for NH_4NO_3 thermodynamic equilibrium in smoke connected to a specific fire and with a physical age of < 1 day, we also encountered smoke of indeterminate origin, some of which had likely been emitted more than 1 day prior to sampling. Though establishing an estimated physical age is difficult for this smoke, we can use estimated chemical age categories described by O'Dell et al. (in preparation) to assess how the physical smoke context may change the pNH_4 fraction ($pNH_4/\Sigma NH_x$) in older smoke. The first three panels in Figure 4.6 show that there is a negative correlation between the ambient environmental temperature and the pNH_4 fraction in medium (1 - 3 days chemical aging) and old (> 3 days chemical aging) smoke, while this relationship is not present in the young smoke (< 1 day chemical aging). We note that most of the data previously presented in Figures 4.2 - 4.5 is classified as young smoke. Temperature here can be considered an inverse proxy for altitude, with higher sampling altitudes typically having lower temperatures. As might be expected, relative humidity is also correlated with pNH_4 fraction in medium and old smoke, meaning higher pNH_4 fractions are observed at both colder temperatures and higher relative humidities (Figure A16). Since colder and wetter conditions push the NH_4NO_3 equilibrium toward the aerosol-phase, these empirical relationships suggest a larger contribution from inorganic NH_3 partitioning in colder and wetter smoke plumes. Figures 4.6e and 4.6f support this conclusion, showing the same negative relationship with temperature for the fraction of pNO_3 in the sum measured nitrate ($\Sigma NO_3 = pNO_3 + HNO_3$) in medium and old smoke. This conclusion is also consistent with the inference made by Paulot et al. (2017), that smoke plumes injected higher into the free troposphere more favorably produce NH_4NO_3. The fractions of pNH_4 and pNO_3 in each of the Figure 4.6 panels are colored by the ratio of measured sum nitrate to measured sum ammonia ($\Sigma NO_3/\Sigma NH_x$). This ratio suggests that a greater abundance of sum nitrate relative to sum ammonia is correlated with a higher pNH_4 fraction in young and medium chemically aged smoke. Higher $\Sigma NO_3/\Sigma NH_x$ correlating with greater NH_3 partitioning is consistent with one of the insights from Figure 4.5, that NH_4NO_3 production is often limited by HNO_3 availability, as well as the observations from individual fires, where Taylor Creek has the fastest e-folding loss timescale and the highest oxidized nitrogen to reduced N ratios (Chapter 3). We note that the data shown in Figure 4.6 are not background-corrected, thus describing the behavior of total ammonia (panels a - c) and total nitrate (panels d - f) in smoke-impacted air. While entrainment of NH_3, pNH_4, and pNO_3 from surrounding air masses is not likely to be contribute to already enhanced abundances in older smoke, HNO_3 may be present in the free troposphere

(Figure A14b) and affect the $p\mathrm{NO_3}$ fraction in well-diluted (medium and old) smoke along with smoke-produced $\mathrm{HNO_3}$. By showing the full observed behavior of the $p\mathrm{NH_4}$ and $p\mathrm{NO_3}$ fractions in smoke across different chemical ages, we conclude that aged smoke plumes in the western U.S. likely contribute to the production of $\mathrm{NH_4NO_3}$ in the free troposphere. This production may be enhanced in smoke with lower temperatures (injection at higher altitudes) and higher $\Sigma\mathrm{NO_3}/\Sigma\mathrm{NH_x}$ ratios.

4.4 Conclusions

We have characterized evolution of gas-phase $\mathrm{NH_3}$ in a set of western wildfire smoke plumes during summer 2018 and investigated some of the complexity in the partitioning of $\mathrm{NH_3}$ to $p\mathrm{NH_4}$, including the relationship of $\mathrm{NH_3}$ partitioning to $\mathrm{HNO_3}$ and other acids as well as to temperature and RH. $\mathrm{NH_3}$ mixing ratios decrease in fresh smoke plumes in most of the sampled plumes, faster than can be explained by dilution alone, and concurrent increases in observed sub-micron $p\mathrm{NH_4}$ from the AMS are able to account for this loss in many plumes. While the limited existing literature on $\mathrm{NH_3}$ evolution in smoke tends to estimate a lifetime or effective lifetime for $\mathrm{NH_3}$ loss, we recognize the complexity in this term: $\mathrm{NH_3}$ is likely lost from the gas phase through an equilibrium process dependant on T and RH that happens concurrent with ongoing dilution and changing inorganic and organic acids abundances. Thus we describe an e-folding loss timescale to quasi-equilibrium for $\mathrm{NH_3}$ gas-particle partitioning that is on the order of tens of minutes to several hours in the fresh smoke plumes sampled. We find empirical evidence for the association of $\mathrm{NH_3}$ and $\mathrm{HNO_3}$ to form $\mathrm{NH_4NO_3}$ through the positive relationship between the $p\mathrm{NH_4}$ fraction of $\Sigma\mathrm{NH_x}$ and the $\Sigma\mathrm{NO_z}$ fraction of $\Sigma\mathrm{NO_y}$. We examine the thermodynamic context for the formation of $\mathrm{NH_4NO_3}$ by calculating the $\mathrm{K_p}$ ratio. Under the assumption that this equilibrium is independent from aerosol mixing state, phase separation, or pH, we find that many of our *in situ* measurements are far from equilibrium, both super- and sub- saturated with respect to $\mathrm{NH_4NO_3}$. Fresh, dense plumes injected at higher altitudes (and lower temperatures) are more likely to favor $\mathrm{NH_4NO_3}$ formation. We also suggest the presence of $\mathrm{NH_4}$-organic salts in the plumes sampled given the abundant organic acid ions measured by the PILS. Lastly, in smoke with chemical ages older than ~1 day, we find evidence for the presence of $\mathrm{NH_4NO_3}$ via the negative relationship between the environmental temperature and both $p\mathrm{NH_4}$ and $p\mathrm{NO_3}$ fractions. This again suggests that smoke injected higher in the free troposphere favors the formation of $\mathrm{NH_4NO_3}$, consistent with the findings of Paulot et al. (2017).

CHAPTER 5

INVESTIGATING MECHANISMS FOR PAN AND PPN PRODUCTION IN WESTERN U.S. WILDFIRE SMOKE PLUMES[3]

5.1 INTRODUCTION

As discussed in prior chapters, wildfires are an important source of reactive nitrogen (N_r) to the atmosphere (Lobert et al. 1990). Acyl peroxy nitrates (APNs) are a class of NO_y compounds with the general structure, $RC(O)OONO_2$, that are thought to be particularly important atmospheric reservoirs of NO_x (Singh and Hanst 1981; Singh 1987). APNs are in a highly temperature-dependent chemical equilibrium with their acyl peroxy (AP) radical precursors and NO_2, and can act as a temporary sink for NO_x in fresh smoke plumes injected in the free troposphere. In these conditions, rapid formation of APNs is facilitated by the combined effect of large precursor concentrations and lower temperatures. As smoke plumes dilute and move downwind, APNs can decompose and become a source of NO_x, thereby contributing to the transport of N_r across continental scales (Fischer et al. 2014) and production of O_3 in downwind regions (*e.g.* Val Martín et al. 2006; Jaffe and Wigder 2012). Despite a recognition of the importance of APN chemistry for the overall chemical evolution of smoke, reproducing the production of PAN in smoke plumes has remained challenging for models (*e.g.* Alvarado et al. 2015). This is at least partially due to the sheer number of factors that influence APN formation, including OH abundance, actinic flux, precursor abundances, and environmental conditions.

The most common APN is peroxyacetic nitric anhydride (PAN; $CH_3C(O)O_2NO_2$; also often called by its misnomer peroxyacetyl nitrate) (Roberts 2007). PAN is formed by the reaction of the peroxy acetyl (PA; $CH_3C(O)O_2$) radical with NO_2. Typically the next most abundant APN, peroxypropionic nitric anhydride (PPN; $CH_3CH_2C(O)O_2NO_2$) is the product of the reaction of the peroxy propionyl radical (PP radical; $CH_3CH_2C(O)O_2$) with NO_2. The following set of reactions describe the production and loss of PAN by a representative oxygenated volatile organic compound (oVOC). Reactions 5.1a and 5.1b describe the formation pathways for PA radicals via the OH oxidation or photolysis of aldehydes, ketones or other oVOCs. Reactions 5.2a and 5.2a describe the reversible reaction between the PA radical and NO_2 to form PAN, and Reactions 5.3 - 5.6 describe chemical loss pathways for the PA radical or PAN.

[3]Adapted from a manuscript in preparation for *JGR Atmospheres*, June 2020

$$\text{oVOC} + \text{OH}\ (+\text{O}_2) \rightarrow \text{RC(O)O}_2 \tag{5.1a}$$

$$\text{oVOC} + h\nu(+\text{O}_2) \rightarrow \text{RC(O)O}_2 \tag{5.1b}$$

$$\text{RC(O)O}_2 + \text{NO}_2 \rightarrow \text{RC(O)OONO}_2 \tag{5.2a}$$

$$\text{RC(O)OONO}_2 \rightarrow \text{RC(O)O}_2 + \text{NO}_2 \tag{5.2b}$$

$$\text{RC(O)O}_2 + \text{NO} \rightarrow \text{products} \tag{5.3}$$

$$\text{RC(O)O}_2 + \text{HO}_2 \rightarrow \text{products} \tag{5.4}$$

$$\text{RC(O)O}_2 + \text{RO}_2 \rightarrow \text{products} \tag{5.5}$$

$$\text{RC(O)OONO}_2 + \text{OH} \rightarrow \text{products} \tag{5.6}$$

The most important immediate APN precursors, defined here as a direct PA or PP radical precursor, vary depending on the environment. Globally the most important immediate PAN precursors are thought to be acetaldehyde, acetone (particularly in the upper free troposphere), and methylglyoxal (Fischer et al. 2014). In polluted urban environments such as Houston acetaldehyde is the dominant PA radical precursor (Roberts et al. 2001; Sillman and West 2009), whereas in heavily vegetated places with large biogenic emissions methacrolein can be a major PA radical source (Roberts et al. 2001; Williams et al. 1997). In Chinese megacities such as Beijing, acetaldehyde is the dominant PAN precursor (Xue et al. 2014), but both acetaldehyde and methylglyoxal appear to be important immediate PAN precursors at a rural site outside Beijing and in the Pearl River Delta region (Xue et al. 2014; Yuan et al. 2018). In locations where urban outflow mixes with biogenic emissions, methylvinyl ketone (MVK), methacrolein, methylglyoxal, biacetyl, and acetaldehyde are significant immediate PAN precursors (LaFranchi et al. 2009). Thus, while the PA radical has many possible oxygenated volatile organic compound (oVOC) precursors, in most regions a handful of species likely account for the majority of

PA radical production. For PPN, the dominant (and often assumed exclusive) immediate precursor in most environments is propanal (CH_3CH_2CHO)(Roberts et al. 2001).

There are limited measurements of PAN with its likely immediate PAN radical precursors in smoke over the appropriate chemical timescales suitable for empirically based assessments of PAN production in fresh wildfire smoke. To our knowledge only two studies have investigated the immediate oVOC PAN precursors in smoke, and no studies have investigated the immediate precursors of PPN. Using detailed chemical modeling, Müller et al. (2016) found that acetaldehyde and biacetyl are the major PAN precursors in a small prescribed burn smoke plume in Georgia. Likewise, Liu et al. (2016) used a similar chemical modeling approach to conclude that biacetyl is needed along with acetaldehyde to explain PAN production in southeastern U.S. agricultural fire smoke plumes. Here, we investigate PAN and PPN evolution in 8 pseudo-Lagrangian smoke plumes sampled during the Western Wildfire Experiment for Cloud Chemistry, Aerosol Absorption, and Nitrogen (WE-CAN) aircraft campaign. We find evidence of PAN and PPN production within the first several hours of physical aging in every plume. Next we use a simple chemical production model for PAN and PPN to test our ability to predict PAN and PPN formation using a small set of likely precursors. We find empirical evidence that acetaldehyde and biacetyl are important immediate PAN precursors in large western wildfire smoke plumes, and suggest that models at all scales need to include emissions, formation, and photolysis of biacetyl in order to represent PAN production. Lastly, we determine that additional PPN precursors are likely needed in western smoke apart from propanal, and hypothesize ethylglyoxal may be a likely candidate. Very few measurements of ethylglyoxal exist however, suggesting an area of future research.

5.2 Methods specific to this analysis

5.2.1 Time evolution model of PAN

To estimate the production of PAN and PPN in our plumes, we solve a simplified explicit integral of the mass balance for each species assuming a limited number of dominant production pathways. This integrated steady state mass balance model has been used to investigate PAN production and dominant precursors in forest and urban environments (LaFranchi et al. 2009; Roberts et al. 2001). We define total PAN, PAN_T, as the sum of PAN and the PA radical:

$$[PAN_T] = [PAN] + [PA\ radical] \quad (1)$$

The total abundance of PAN_T is written as the integral over time of the production rate of PAN_T minus the loss rate of PAN_T:

$$[PAN_T] = \int (\text{Production of } PAN_T - \text{Loss of } PAN_T)\, dt \tag{2}$$

Filling in the production and loss terms with Reactions 5.1 - 5.1 from the introduction, where Reactions 5.2a and 5.2b do not affect the net production or loss of PAN_T and thus are not included, yields:

$$[PAN_T] = \int (k_1[OH(t)][oVOC(t)] - k_3[PA(t)][NO(t)] - k_4[PA(t)][HO_2(t)] - k_5[PA(t)][RO_2(t)] - k_6[PAN(t)][OH(t)])\, dt \tag{3}$$

Because the PA radical lifetime is very short ($\ll \sim$1s), we apply a steady state assumption to the PA radical mass balance equation and solve for the steady state concentration of PA radical, PA_{SS}:

$$[PA_{SS}] = \frac{k_1[OH][oVOC] + k_{2b}[PAN]}{k_{2a}[NO_2] + k_3[NO] + k_4[HO_2] + k_5[RO_2]} \tag{4}$$

Incorporating the PA steady state assumption into the PAN_T equation and introduce the parameter β, the equation for PAN_T simplifies to:

$$[PAN_T] = \int (\beta\ k_1[OH(t)][oVOC(t)] - (1-\beta)\ k_{2b}[PAN(t)] - k_6[PAN(t)][OH(t)])\, dt \tag{5}$$

Where β is the probability that the PA radical reacts with NO_2 to form PAN versus being lost to reaction with NO, HO_2, or RO_2.

$$\beta = \frac{k_{2a}[NO_2]}{k_{2a}[NO_2] + k_3[NO] + k_4[HO_2] + k_5[RO_2]} \tag{6}$$

Generalizing the PAN_T integrated mass balance to include production from the oxidation of several oVOCs produces:

$$[PAN_T] = \int (\beta\ (\sum_i k_i[OH(t)][oVOC_i(t)]) - (1-\beta)\ k_{2b}[PAN(t)] - k_6[PAN(t)][OH(t)])\, dt \tag{7}$$

Following the same logic yields an equation for total PPN (PPN_T = PPN + PP radical), where β is assumed to be the same for both PA and PP radicals:

$$[\mathrm{PPN}_T] = \int (\beta\ (\sum_i k_i[\mathrm{OH}(t)][\mathrm{oVOC}_i(t)]) - (1-\beta)\ k_{2b}[\mathrm{PPN}(t)] - k_6[\mathrm{PPN}(t)][\mathrm{OH}(t)])\ \mathrm{d}t \quad (8)$$

Equations 7 and 8 are then solved iteratively, adding the net production for each time step to the previous estimate for PAN (including terms for production of PA radicals by both oxidation and photolysis):

$$[\mathrm{PAN}](t+1) = (\beta\ (\sum_i k_i(t)[\mathrm{OH}(t)][\mathrm{oVOC}_i(t)] + \sum_i j_i(t) * [\mathrm{oVOC}_i(t)]) - (1-\beta)\ (k_{2b}(t)[\mathrm{PAN}](t)) - k_6(t)[\mathrm{OH}(t)][\mathrm{PAN}(t)])) * \Delta t \quad (9)$$

And for PPN:

$$[\mathrm{PPN}](t+1) = (\beta\ (\sum_i k_i(t)[\mathrm{OH}(t)][\mathrm{oVOC}_i(t)] + \sum_i j_i(t) * [\mathrm{oVOC}_i(t)]) - (1-\beta)\ (k_{2b}(t)[\mathrm{PPN}](t)) - k_6(t)[\mathrm{OH}(t)][\mathrm{PPN}(t)])) * \Delta t \quad (10)$$

The WE-CAN measurements contain most of the information (*i.e.* oVOC precursors, j-values, temperature) needed to solve these equations and compare our estimated PAN and PPN with the observed evolution of PAN and PPN in pseudo-Lagrangian sampled smoke plumes. However, there are a few additional assumptions required. First, we assume that [PA] $\ll$ [PAN], such that $[\mathrm{PAN_T}] \cong [\mathrm{PAN}]$ (and likewise $[\mathrm{PPN_T}] \cong [\mathrm{PPN}]$). This is reasonable given the very short lifetime of PA and PP radicals. Next, we do not have measurements of *in situ* HO_2 and RO_2, but we can infer an upper bound for β using measurements of NO and NO_2. Given ratios of NO/NO_2 of ~0.15 - 0.3 in fresh WE-CAN plumes, this upper bound is ~0.65 - 0.8. Measurements of HO_2 and RO_2 concentrations are rare in smoke. The only measurements we are aware of represent smoke with substantially longer physical ages than the majority of the WE-CAN samples (Cook et al. 2007). These measurements suggest that the sum of HO_2 and RO_2 is between ~10 - 45 pptv (Cook et al. 2007); these small mixing ratios make sense given that these radicals have very short lifetimes against oxidation by OH and NO, and quickly cycle between the HO_x and RO_x families. The combined abundance of HO_2 and RO_2 is rarely above one hundred ppt in other, even highly polluted, environments (*e.g.* Hornbrook et al. 2011; Griffith et al. 2016). β is not very sensitive to HO_2 and RO_2 at these abundances. Even if we include extreme mixing ratios of 500 pptv

for both HO_2 and RO_2 in the calculation of β, the largest change would reduce β to ~0.6. Thus, we can reasonably constrain β between ~0.6 and 0.8.

OH was not directly measured during WE-CAN, and thus OH abundance and evolution needs to be inferred from other measurements. Our understanding of the abundance of evolution of OH in wildfire smoke plumes is rapidly evolving. Studies of smoke across a variety of ecosystems have observed enhanced OH concentrations (Hobbs et al. 2003; Yokelson et al. 2009; Akagi et al. 2012a) that are likely dynamically evolving in fresh plumes (*e.g.* Peng et al. 2020). We explore three general forms of OH concentration timeseries: a constant value of OH with plume age, a timeseries starting with high OH and following an exponential decay to a lower set value, and a timeseries consisting of a linear decrease to a set value. The assumption that OH may be higher in the youngest smoke is based on the high abundances of HONO often observed in the freshest WE-CAN smoke plumes and analyses indicating that the rapid photolysis of this HONO is an important source of OH (Peng et al. 2020). We describe our specific estimates of OH in the Section 5.3.

Assumptions are also required to attribute fractions of individual mass/charge (m/z) measurements made by the PTR-ToF-MS to different isomers. The PTR-ToF-MS measurements are reported using the isomer fractions calculated by Koss et al. (2018). The Koss et al. (2018) fractions were estimated from Fire Influence on Regional and Global Environments Experiment (FIREX-2016) lab measurements of freshly emitted smoke, and the relative proportions of different isomers could change with smoke age. When possible, we test and evaluate these fractions using the speciated GC-MS measurements from the Total Organic Gas Analyzer (TOGA) instrument (Apel et al. 2003, 2015). While at too low of time resolution to use directly in estimating the NEMRs of oVOC APN precursors, the TOGA measurements are generally consistent with the estimated oVOCs fractions used here. More details are provided in Section 5.3.2 and in the appendix.

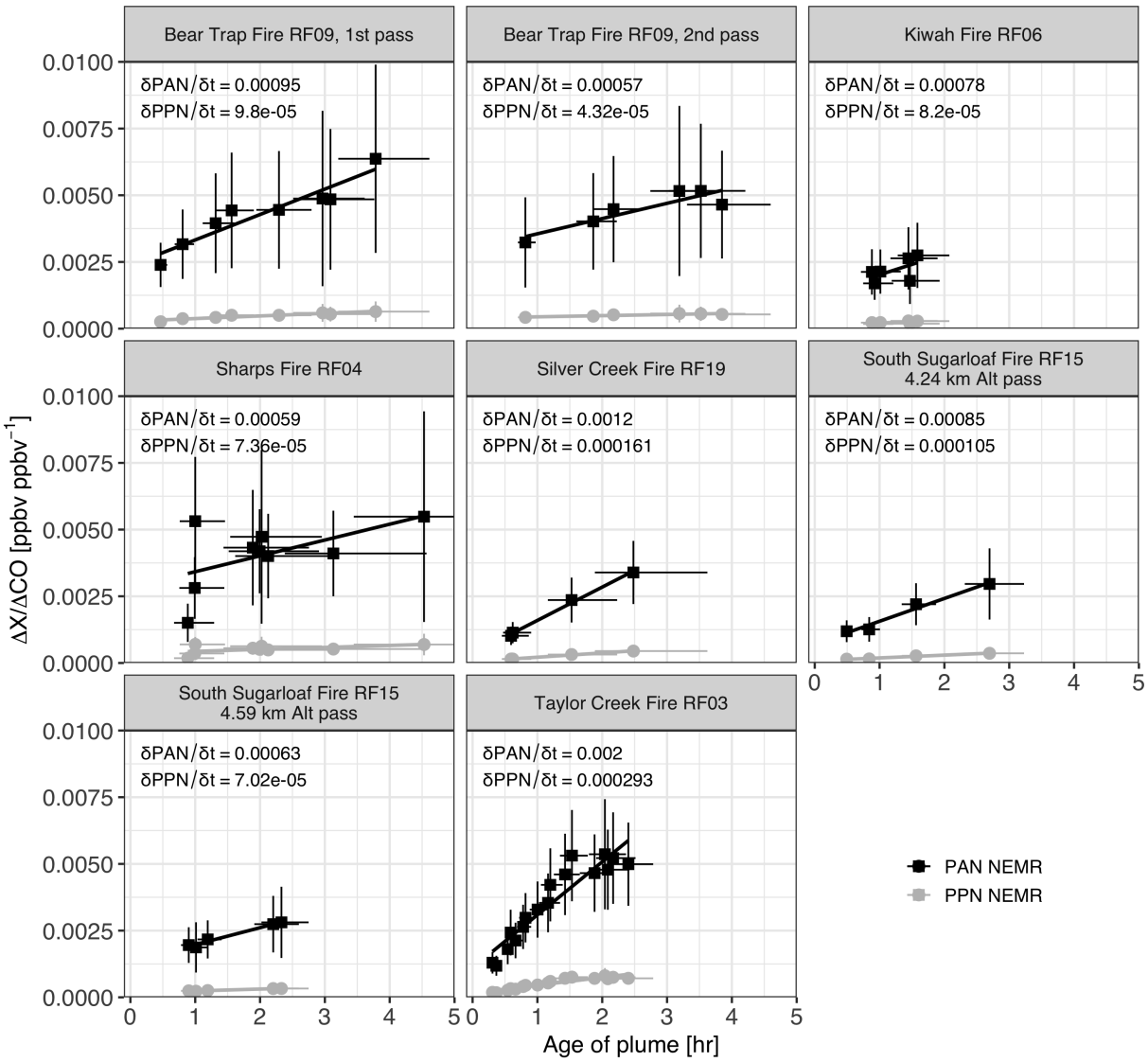

FIG. 5.1. PAN and PPN NEMRs (black squares and grey circles respectively) plotted with estimated physical plume age for 8 separate pseudo-Lagrangian sampling patterns of fires sampled during WE-CAN. The linear rate of change in PAN and PPN NEMRs is specified within each panel, in units of ppbv/ppbv CO hr^{-1}. 1σ standard deviation error bars are included for both calculated NEMRs and estimate physical age. PPN NEMR errors are too small to be distinguished on many of the sub-plots.

5.3 RESULTS AND DISCUSSION

5.3.1 Observed PAN and PPN evolution

Figure 5.1 presents the evolution of observed PAN and PPN NEMRs with estimated physical age in 8 pseudo-Lagrangian sampled plumes. PAN is not directly emitted by wildfires so the presence of positive NEMRs in the earliest transect through each plume is evidence of rapid PAN and PPN production

within minutes of emission. Corrected for dilution using CO, both PAN and PPN abundances increase over the first several hours. The PAN rate of increase ranges from 0.0006 ppbv/ppbv CO hr^{-1} to 0.002 ppbv/ppbv CO hr^{-1} and PPN increases at a rate of 4×10^{-5} to 2×10^{-4} ppbv/ppbv CO hr^{-1}. The PAN and PPN NEMR increases during the Taylor Creek Fire smoke plume are both about twice as fast as in any other plume.

Akagi et al. (2012a) observed a factor of 10 increase in $\Delta PAN/\Delta CO_2$ ratios over 4 hours in a chaparral fire in southern California, or a factor of 2.5 per hour. For comparison WE-CAN plumes increase by a factor of 0.5 - 2.3 per hour, i.e. there is a slower rate of increase in all WE-CAN plumes except for Taylor Creek. However, Akagi et al. (2012a) intercepted the chaparral fire plume closer to the source than most of the WE-CAN sampling, and therefore likely captured much of the rapid initial production of PAN. Alvarado et al. (2010) observed enhancements of PAN increasing from 0.04% - 0.08% to 0.23% - 0.36% over about 4 hours in a Canadian boreal wildfire plume. This corresponds to factors of 0.7 - 2.25 per hour increases in PAN. Liu et al. (2016) observed increases of the ratio of PAN to NO_y in southeastern US agricultural fires, of similar rates to that observed by Alvarado et al. (2010). Further afield in the Yucatan, Yokelson et al. (2009) documented PAN NEMRs increasing from 0.0025 to 0.006 over 1 hour in a tropical forest fire plume, corresponding to a factor of 2.4 increase in an hour. In summary, PAN NEMRs with the WE-CAN smoke plumes evolved in a manner consistent with previous observations.

The flattening of the PAN and PPN NEMRs at ~1.5 hours of aging in the Taylor Creek Fire plume (RF03; 30 June 2018) suggests that PAN production may slow after the first few hours of plume transport. Not all individual plumes were sampled long/far enough to test if PAN production slows similarly in every plume, though a composite analysis by Juncosa Calahorrano et al. (submitted) suggests that the PAN fraction of total measured oxidized reactive nitrogen stabilizes after ~3 hours of physical plume transport. If the smoke is transported isothermally and the NO_x ratio stays consistent, PAN and PPN may reach an equilibrium. Of course the absolute abundances of APNs may continue to fall due to dilution with additional transport. If the plume then ascends/descends and the environmental temperature changes, or if the NO/NO_2 ratio changes due to permanent sinks of NO_x, mixing with background air, or additions of fresh NO_x from outside sources, then this equilibrium would shift, taking up more NO_2 into APNs (at colder temperatures or lower NO/NO_2 ratios) or releasing NO_x into the air mass (at higher temperatures and higher NO/NO_2 ratios). Satellite observations of PAN in smoke plumes or *in situ* field projects that are able to sample the same plume for several days of aging may

offer additional insights into the equilibrium behavior of APNs in smoke that are difficult to infer from the WE-CAN dataset.

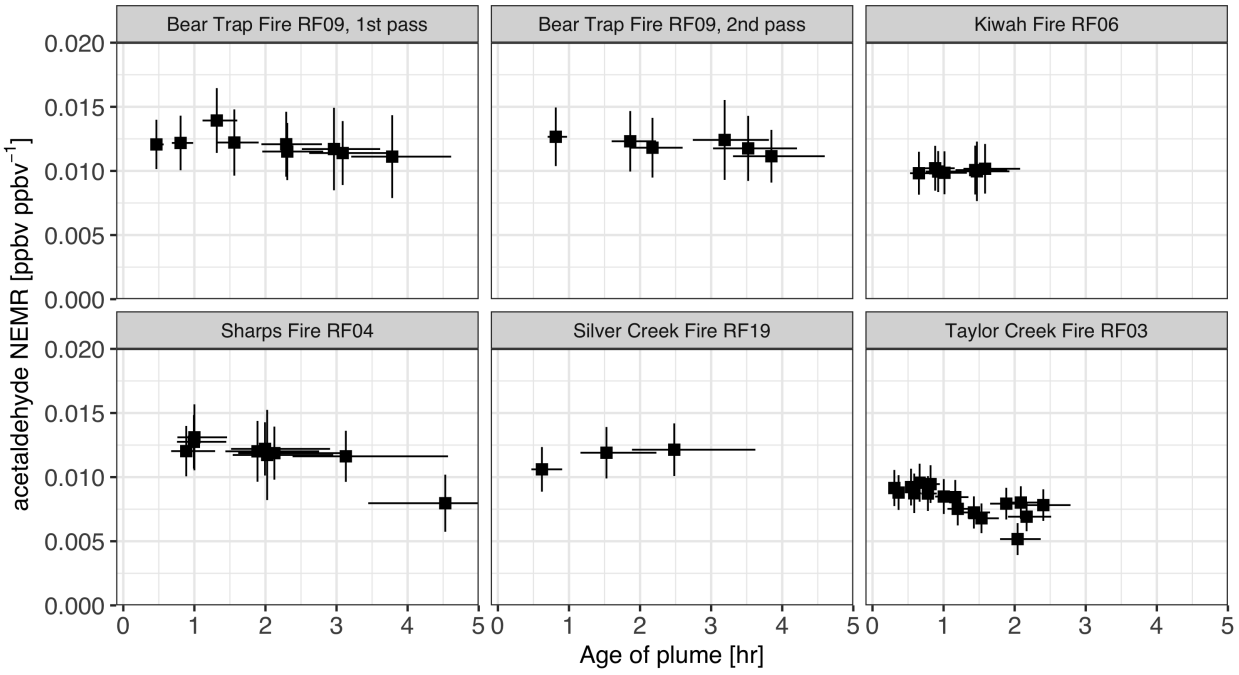

FIG. 5.2. Evolution of acetaldehyde with estimated physical age for pseudo-lagrangian sampled plumes in WE-CAN. Vertical NEMR 1σ standard deviation error bars are included and horizontal error bars denote the 1σ standard deviation in estimated physical age.

5.3.2 Constraints on PAN and PPN model inputs

We move now to examining three case studies of PAN and PPN production using the integrated mass balance production model described in Section 5.2.1. The three plume case studies are the Taylor Creek Fire, the Bear Trap Fire 1st pass sampling pattern, and the Silver Creek Fire plumes. These case studies were chosen as the most well constrained examples of PAN and PPN evolution in the WE-CAN dataset that also contain all the measurements necessary as inputs for the model (*e.g.,* South Sugarloaf Fire plume sampling does not include PTR-ToF-MS measurements). There are four sets of variable inputs to the model: the OH concentration, the value of β, the oVOCs mixing ratios, and the reaction rate coefficients/photolysis rate coefficients. Several of these input have constraints, and we walk through these next.

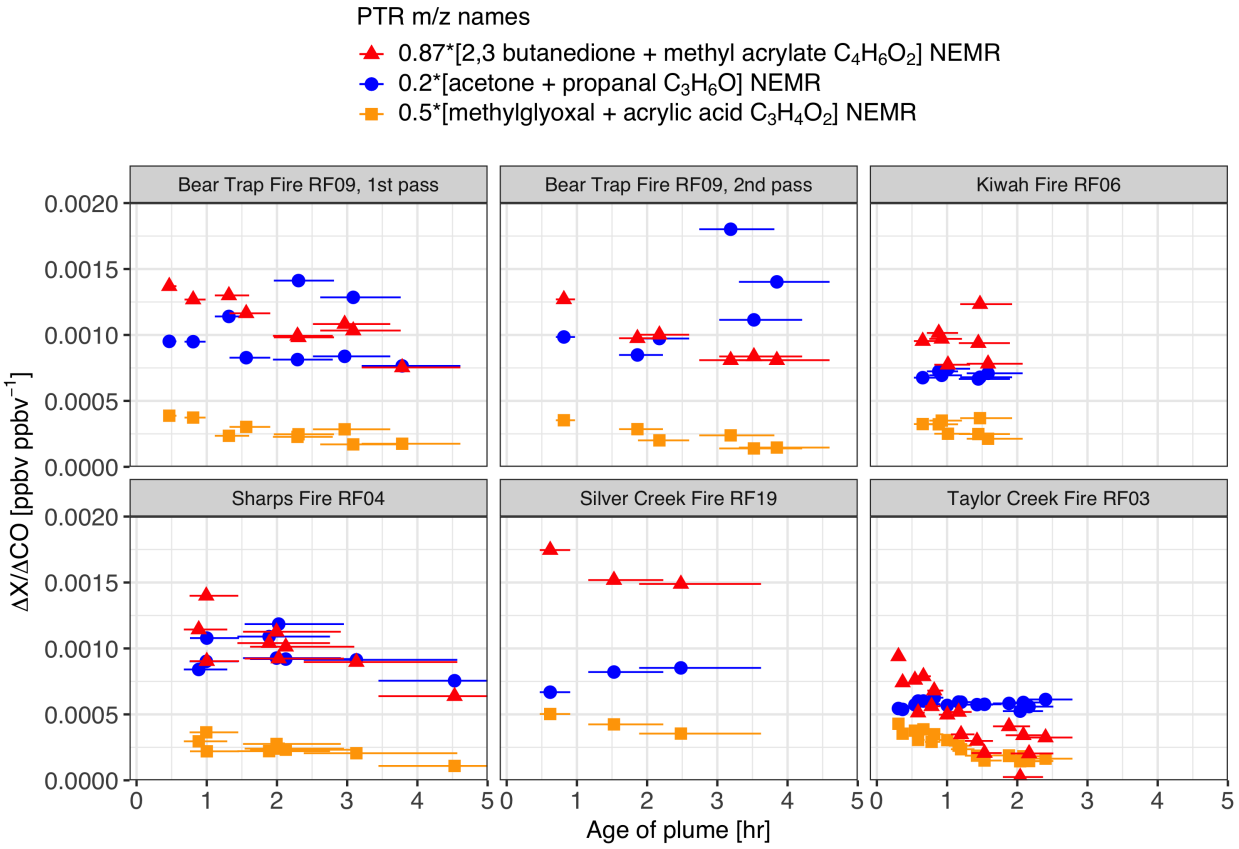

FIG. 5.3. Evolution of biacetyl (2,3-butanedione), methylglyoxal, and propanal with estimated physical age for pseudo-Lagrangian sampled plumes in WE-CAN. NEMR 1σ standard deviation error bars are not shown to enable easier interpretation. Errors are large for each of these measurements, on the order of 100% of the calculated NEMRs for most transects. Horizontal error bars denote the 1σ standard deviation in estimated physical age.

We choose to include the subset of quantified oVOCs in the model that can serve as immediate PA and PP radical precursors on the timescale of the WE-CAN observations. For PAN, acetaldehyde is commonly an important precursor, and biacetyl and methylglyoxal have been shown to be important precursors in southeastern U.S. agricultural and prescribed burns (Liu et al. 2016; Müller et al. 2016). Many other species such as acetone, hydroxyacetone, methyl ethyl ketone (MEK), MVK, and methacrolein are potential PA radical sources but the combination of their relatively slower oxidation/photolysis rates and their observed abundances in smoke make them less important in fresh smoke plumes. For PPN the assumed dominant immediate precursor is propanal. All of the aforementioned species were detected by the PTR-ToF-MS instrument during WE-CAN, though all but acetaldehyde are quantified together with isomers of their molecular formula. We base our apportionment on Koss et al. (2018)

and update it based on an evaluation of the TOGA measurements. For example, Koss et al. (2018) suggest a fraction of one for acetone and 0 for propanal in the acetone+propanal m/z peak of 59.0491. However TOGA's speciated measurements of propanal as a percentage of propanal + acetone show a range of fractions between 5 - 20% in smoke (CO > 500 ppbv; Figure A17). Thus we use propanal fractions of 0.15 and 0.1. Methylglyoxal and biacetyl are not quantified by TOGA, so we rely on the Koss et al. (2018) estimated fractions of 0.5 and 0.87 times their respective m/z peak mixing ratios. These fractions could change over time given different production and loss rates of the different contributing species to each m/z peak. However, we do not have further constraints and thus use a constant fraction for each species. Figure 5.2 shows the evolution of acetaldehyde in the six pseudo-Lagrangian plumes presented above with valid PTR measurements, and Figure 5.3 shows the evolution of biacetyl, methylglyoxal, and propanal on a smaller y axis range. All six plumes are shown rather than just the three we will focus on as case studies to show the consistency in behavior across pseudo-Lagrangian sampled plumes in WE-CAN. Acetaldehyde NEMRs are much larger than those of the other PAN or PPN precursors, and tend to be relatively constant with estimated physical age. Likewise propanal tends to be nearly constant, while methylglyoxal and biacetyl (2,3 butanedione) both decrease with physical age. It is worth noting that the freshest NEMRs for acetaldehyde, biacetyl, and propanal in the Taylor Creek Fire are smaller than the freshest NEMRs in the other plumes. We know the Taylor Creek plume was particularly reactive and had a higher MCE than most smoke plumes sampled (Peng et al. 2020), indicating a larger contribution from flaming combustion processes. This could mean either the emissions of these species were lower in the Taylor Creek Fire, or that more rapid chemical losses between the time of emission and first sampling are reflected in the lower NEMRs. For the purposes of our PAN and PPN production models however, we use smoothed estimates of the evolution of each oVOC with time as inputs to the production terms. Observed changes in oVOCs abundances (i.e. timescale of minutes to hours) are slow enough not to affect the steady-state assumption in the PAN and PPN production models.

TABLE 5.1. Rate coefficients used in this analysis.

	k(T) or k(T,[M])[a]	k(298 K)	Reference
VOC + OH reactions			
acetaldehyde	$4.4\times10^{-12}\exp(365/T)$	1.5×10^{-11}	Atkinson et al. (2006)

[a] Where $k(M = \frac{k_0[M]}{1+\frac{k_0[M]}{k_{inf}}} \times F_c$ and $\log(F_c) = \frac{\log(F_{cent})}{1+(\frac{\log(k_0[M]k_{inf})}{N})^2}$

TABLE 5.1. Rate coefficients used in this analysis.

	k(T) or k(T,[M])[a]	k(298 K)	Reference
methylglyoxal	$1.83\times10^{-12}\exp(560/T)$	1.2×10^{-11}	Baeza-Romero et al. (2007)
ethylglyoxal		1.4×10^{-11}	Jenkin et al. (1997)
propanal	$5.1\times10^{-12}\exp(405/T)$	2.0×10^{-11}	Atkinson et al. (2006)
butenes	$6.6\times10^{-12}\exp(465/T)$	3.1×10^{-11}	Jenkin et al. (1997)
methylfurans		7.3×10^{-11}	Aschmann et al. (2011)
toluene	$1.8\times10^{-12}\exp(340/T)$	5.6×10^{-12}	Jenkin et al. (2003)
Acyl Peroxy Radical reactions			
$RC(O)O_2 + NO_2 \rightarrow APN$	$k_0 = 2.7\times10^{-28}(T/300)^{-7.1}$ $k_{inf} = 1.2\times10^{-11}(T/300)^{-0.9}$ $F_{cent} = 0.3$ $N = 1$	1.0×10^{-11}	Atkinson et al. (1997, 2004)
$PAN \rightarrow RC(O)O_2 + NO_2$	$k_0 = 4.9\times10^{-3}\exp(-12100/T)$ $k_{inf} = 4.0\times10^{16}\exp(-13600/T)$ $F_{cent} = 0.3$ $N = 1.41$	4.6×10^{-4}	Atkinson et al. (1997, 2004)
$PPN \rightarrow C_2H_5C(O)O_2 + NO_2$	$k_0 = 1.7\times10^{-3}\exp(-112800/T)$ $k_{inf} = 4.0\times10^{16}\exp(-13940/T)$ $F_{cent} = 0.36$ $N = 1.41$	4.6×10^{-4}	Kirchner et al. (1999)
$RC(O)O_2 + NO \rightarrow$ products	$8.1\times10^{-12}\exp(270/T)$	2×10^{-11}	Atkinson et al. (1997, 2004)
$RC(O)O_2 + HO_2 \rightarrow$ products	$4.3\times10^{-13}\exp(1040/T)$	1.4×10^{-11}	Jenkin et al. (1997)
$RC(O)O_2 + RO_2 \rightarrow$ products	$2.0\times10^{-12}\exp(500/T)$	1.1×10^{-11}	Tyndall et al. (2001)

[a] Where $k(M = \frac{k_0[M]}{1+\frac{k_0[M]}{k_{inf}}} \times F_c$ and $\log(F_c) = \frac{\log(F_{cent})}{1+(\frac{\log(k_0[M]/k_{inf})}{N})^2}$

TABLE 5.1. Rate coefficients used in this analysis.

	k(T) or k(T,[M])[a]	k(298 K)	Reference
APN + OH reactions			
PAN		3×10^{-14}	Talukdar et al. (1995)
PPN		3×10^{-13}	LaFranchi et al. (2009)
NO_x and HO_x reactions			
$NO + HO_2$	$3.5\times10^{-12}\exp(250/T)$	8.1×10^{-12}	NASA (2015)
$NO + RO_2$	$2.54\times10^{-12}\exp(360/T)$	8.5×10^{-12}	Jenkin et al. (1997)
$HO_2 + RO_2$	$2.9\times10^{-13}\exp(1300/T)$	2.3×10^{-11}	Jenkin et al. (1997)
$RO_2 + RO_2$		2.4×10^{-12}	Jenkin et al. (1997)

[a] Where $k(\mathrm{M} = \frac{k_0[\mathrm{M}]}{1+\frac{k_0[\mathrm{M}]}{k_{\mathrm{inf}}}} \times \mathrm{F}_c$ and $\log(\mathrm{F}_c) = \frac{\log(\mathrm{F}_{cent})}{1+(\frac{\log(k_0[\mathrm{M}]k_{\mathrm{inf}})}{\mathrm{N}})^2}$

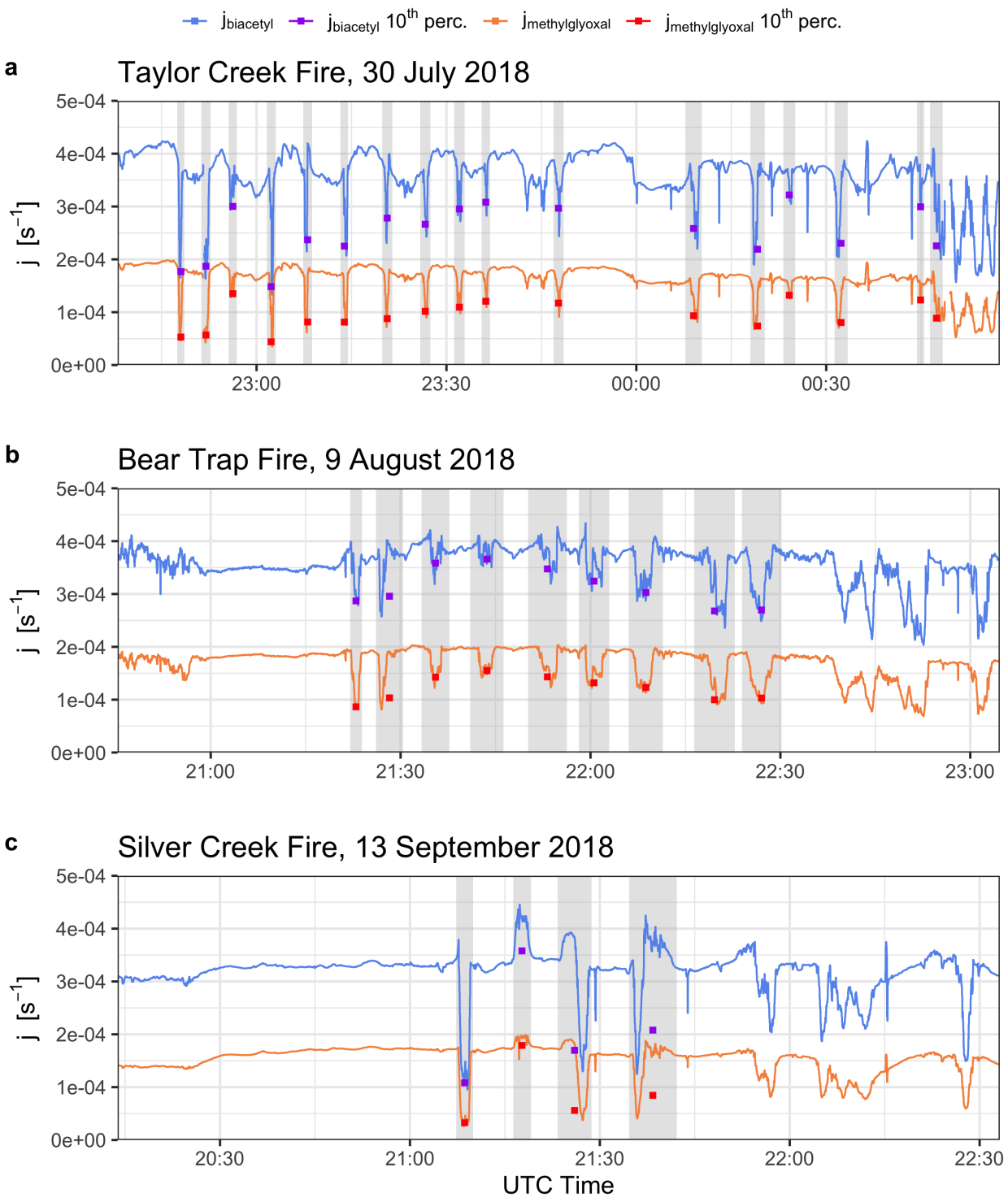

FIG. 5.4. Timeseries of observed photolysis dissociation rates, j, for biacetyl in blue and methylglyoxal in orange for the three case study plumes. Purple and red points are the 10th percentile values for j-biacetyl and j-methylglyoxal respectively in each plume transect (grey shading).

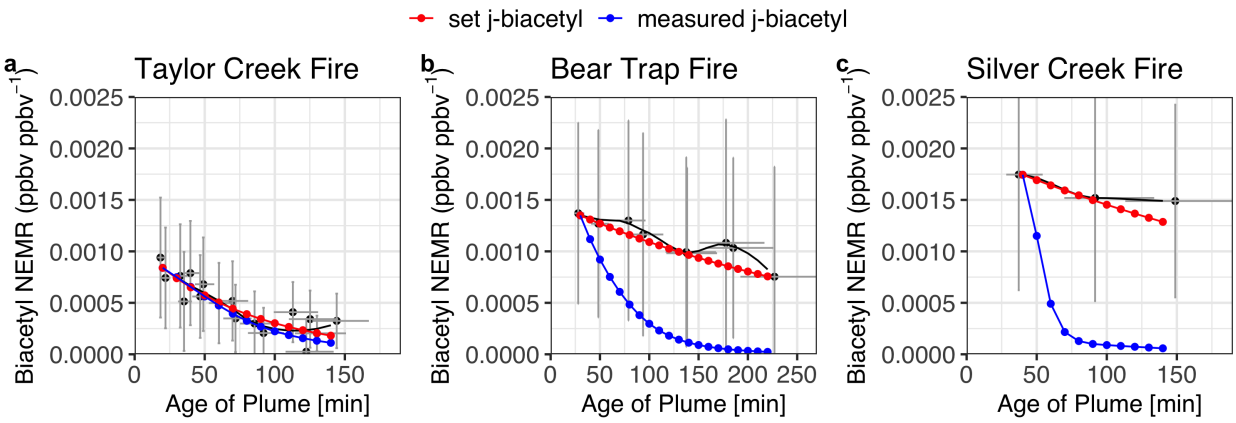

FIG. 5.5. Observed and estimated evolution of biacetyl NEMRs with physical age for the three case study plumes. Estimated loss following observed photolysis rates is in blue, and estimated loss using constant values of 1×10^{-4}, 5×10^{-5}, and 5×10^{-5} s^{-1} respectively for the Taylor Creek, Bear Trap, and Silver Creek plumes are in red. Production of biacetyl is assumed negligible.

We use the set of rate coefficient equations compiled in LaFranchi et al. (2009) for the set of reactions in the introduction 5.1 - 5.6),shown in Table 5.1, and use mean ambient temperature from each transect to produce time-resolved estimates of the rate coefficients. Actinic flux was measured onboard the C-130, and j-values for the photolysis of biacetyl and methylglyoxal are calculated using literature recommended cross sections and quantum yields. In Figure 5.4 we show timeseries of the biacetyl and methylglyoxal j-values for each of the plume sampling time periods. Grey shading indicates plume transects and we clearly observe depressed j-values in the middle (and more dense) parts of each transect due to enhanced scattering and absorption in the dense plume cores. To arrive at a timeseries of j-values to use in the model, we calculate the 10th percentile j-value of each plume transect and interpolate between them across the estimated physical plume age. Figure 5.5 shows the predicted evolution of biacetyl assuming only loss by photolysis, with the interpolated observed j-values included in the blue loss term. Even with this conservative observation-based estimate of the photolysis rate, the model overestimates the observed loss rate of biacetyl. No production of biacetyl is included here. The main formation pathway of biacetyl is the oxidation of o-xylene with a branching ratio of ~0.35 (Jenkin et al. 2003). However, the low abundance of o-xylene and the low relative probability of this formation pathway mean significant biacetyl production with the first few hours of smoke plume aging is unlikely. The red line in Figure 5.5 is based on setting a constant j-value of 1×10^{-4}, 5×10^{-5}, and 5×10^{-5} s^{-1} respectively for the Taylor Creek, Bear Trap, and Silver Creek plumes. These "set j-values" are a factor of 2-4 lower than the observed j-values (used in blue line in Figure 5.5) for biacetyl, but fit the loss rate

of biacetyl (black dots in Figure 5.5) in each plume. We explore the difference the observed versus loss constrained j-values make on the estimated PAN production below.

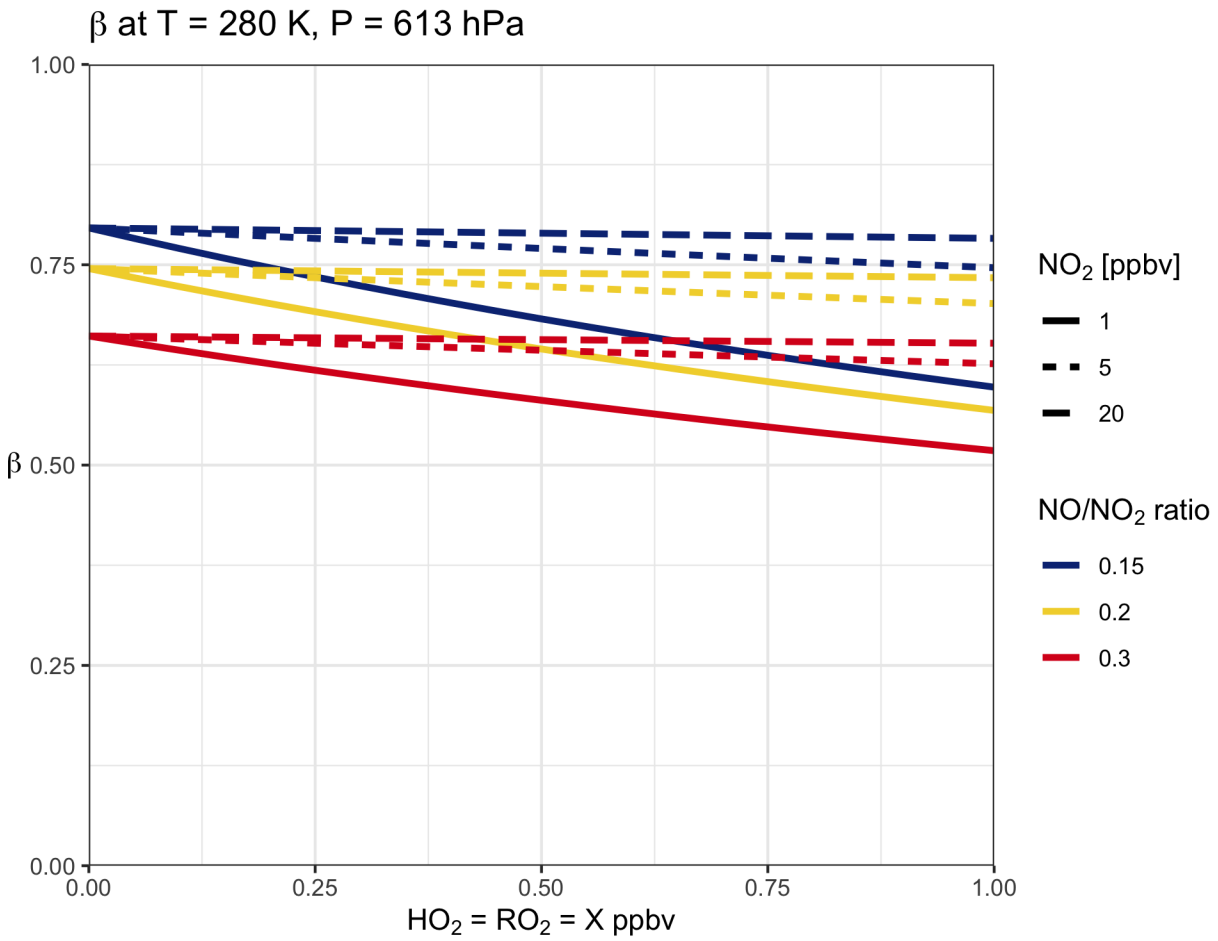

FIG. 5.6. Estimates of β under different NO_x and HO_2 and RO_2 conditions. For plotting simplicity we assume HO_2 and RO_2 both equal the given x-axis value. NO_2 mixing ratios are set and denoted by line type, whereas NO mixing ratios are calculated based on the NO/NO_2 ratio and denoted by different colors.

β describes the relative probability of the formation of PAN (PPN) by the PA (PP) + NO_2 reaction, versus the probability of permanent loss of PA (PP) radical to reaction with NO, HO_2, or RO_2. Therefore β depends on the concentrations of NO_2, NO, HO_2 and RO_2. We only have measurements of NO_2 and NO in all plumes. Cook et al. (2007) reported HO_2 and RO_2 mixing ratios of 10 - 45 pptv in aged smoke plumes over the Atlantic, and Liu et al. (2016) modeled HO_2 and RO_2 concentrations of $\sim 10^8$ - 10^9 molecules cm^{-3} (or ~2 - 25 pptv at T = 273, P = 700 hPa) in southeastern U.S. agricultural smoke plumes. In Figure 5.6 we explore the range of potential β values under different NO_x and HO_2 and RO_2 concentrations. Across all fresh WE-CAN plumes, we observed a range of NO/NO_2 ratios from ~0.15 -

0.3, and NO_2 mixing ratios from ~1 ppbv to tens of ppbv. We explore NO/NO_2 ratios of 0.15, 0.2, and 0.3 in three colors for NO_2 abundances of 1, 5, and 20 ppbv in the solid and dashed lines, over a range of HO_2 and RO_2 mixing ratios from 0 to 1 ppbv each. Without any HO_2 or RO_2, β varies from ~0.65 - 0.8, and even under very large HO_2 and RO_2 mixing ratios and relatively small NO_x β only varies between 0.5 - 0.8. Therefore, we set 0.8 as an upper bound for β, and entertain a range from 0.6 - 0.8, with 0.7 as the default value. Since the NO_x ratio remains relatively constant on the timescales sampled here, β does not evolve with time.

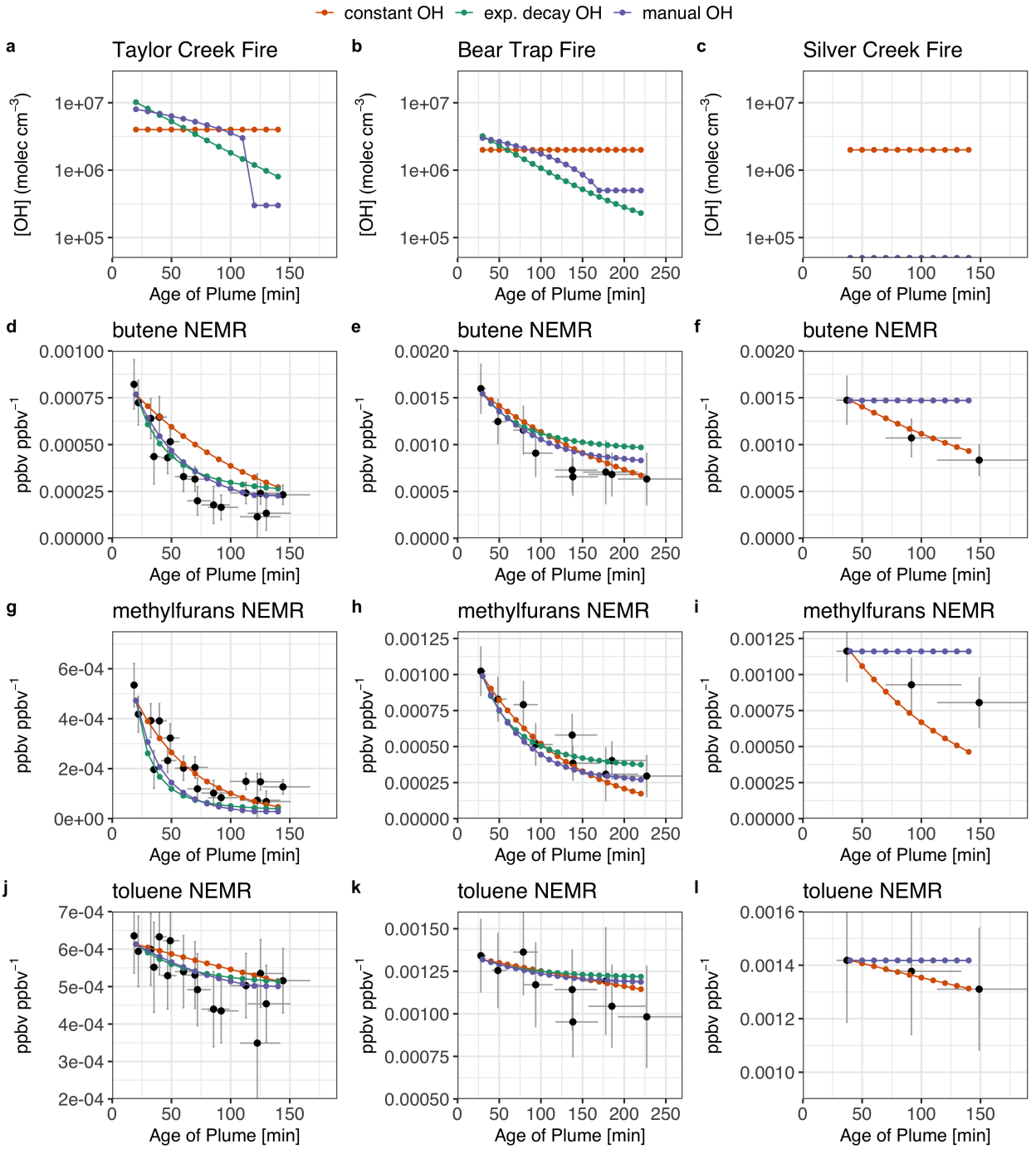

FIG. 5.7. a, b, c) Prescribed OH concentration timeseries for the three case study plumes. d, e, f) Observed and estimated evolution of butenes NEMRs (all isomers measured together) with estimated physical age for the three case study plumes. g, h, i) Observed and estimated evolution of methylfurans NEMRs with estimated physical age for the three case study plumes. 2- and 3-methylfuran are included, rate coefficient used is for 2-methylfuran: 7.31×10^{-11} cm^3 molec.$^{-1}$ s^{-1}. j, k, l) Observed and estimated evolution of toluene NEMRs with estimated physical age for the three case study plumes. Error bars in all panels are the 1σ standard deviations of the calculated NEMRs and estimate physical age.

Lastly, we need to prescribe OH concentration timeseries. Liu et al. (2016) report average OH concentrations of 5×10^5 - 2×10^7 molecules cm^{-3} within the agricultural plumes they modeled. We used this range of values as a starting point and iterated with different prescribed OH concentration timeseries to find a timeseries for each plume that predicted the decay in three fast-reacting primary emitted VOCs: butenes (all isomers measured together), 2- and 3-methylfuran (also measured together), and toluene. We tested 1) setting a constant OH with time, 2) starting at high OH and following an exponential decay with an e-folding time of 45 minutes, and 3) setting a manual timeseries consisting of a linear decrease in OH concentrations down to a set lower value. Figure 5.7 presents visual depictions of each of these three options and the associated calculated decay for each VOC species. A manually-set OH concentration that linearly decreases from 8×10^6 to 3×10^6 molecules cm^{-3} and settles at 5×10^5 molecules cm^{-3} fits the observed VOC decay best for the Taylor Creek Fire (Figure 5.7, left column). A constant OH concentration of 2×10^6 molecules cm^{-3} for both Bear Trap and Silver Creek Fire plumes best matches these observations (Figure 5.7 middle and right columns). These OH concentrations fall within the range estimated by Liu et al. (2016) and are consistent with those estimated by (Hobbs et al. 2003) and (Yokelson et al. 2009). We do not exactly reproduce the observed loss of each of the three VOCs in the three plumes, and this could be due to several factors including imperfect lagrangian sampling, underconstrained OH reaction rate coefficients for 2- and 3- methylfuran (Aschmann et al. 2011), and loss by reaction with other oxidants such as O_3 and NO_3. Methylfurans may also have sources in smoke from isoprene or other conjugated dienes (Brégonzio-Rozier et al. 2015; Tapia et al. 2011). Butenes and toluene however, are not secondarily produced in smoke.

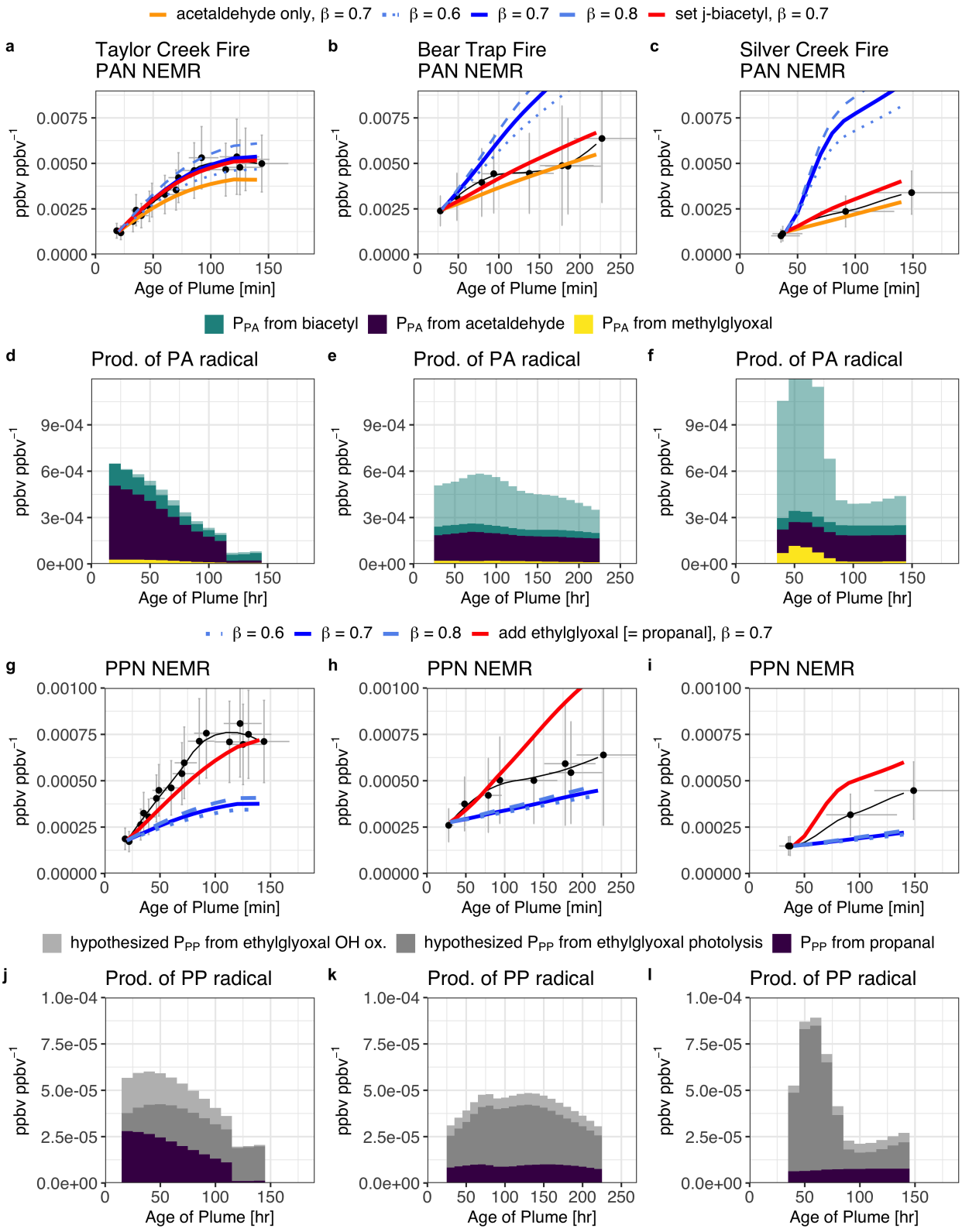
acetaldehyde only, β = 0.7
β = 0.6
β = 0.7
β = 0.8
set j-biacetyl, β = 0.7
a
Taylor Creek Fire
PAN NEMR
b
Bear Trap Fire
PAN NEMR
c
Silver Creek Fire
PAN NEMR
ppbv ppbv⁻¹
Age of Plume [min]
P_PA from biacetyl
P_PA from acetaldehyde
P_PA from methylglyoxal
d
Prod. of PA radical
e
Prod. of PA radical
f
Prod. of PA radical
Age of Plume [hr]
β = 0.6
β = 0.7
β = 0.8
add ethylglyoxal [= propanal], β = 0.7
g
PPN NEMR
h
PPN NEMR
i
PPN NEMR
hypothesized P_PP from ethylglyoxal OH ox.
hypothesized P_PP from ethylglyoxal photolysis
P_PP from propanal
j
Prod. of PP radical
k
Prod. of PP radical
l
Prod. of PP radical

FIG. 5.8. Summary of the PAN and PPN production models compared to observations. Observed (black) NEMRs for PAN (panels a, b, c) and PPN (panels g, h, i) versus estimated physical age for the three case study plumes: Taylor Creek in the left column, Bear Trap 1st set of transects in the middle column, and Silver Creek in the right column. Blue, red, and orange lines represent the modeled PAN and PPN NEMRs for different sets of inputs; blue lines represent the full set of observations and best constraints. Panels d, e, and f show timeseries of the dilution-corrected production of the PA radical, split up by precursor. The biacetyl contribution is further split into lighter and darker shaded portions. The light portion indicates the contribution to the best constrained model (blue line) from observed j-biacetyl, whereas the dark portion shows the contribution from a set value of j-biacetyl (see Figure 5.5). Panels j, k, and l display the total production of the PP radical, with the contribution from propanal in purple (corresponding to the blue line model in panels g, h, and i), and a hypothesized contribution from ethylglyoxal photolysis in dark grey and ethylglyoxal OH oxidation in light grey (corresponding to the red line model in panels g, h, and i).

5.3.3 PAN and PPN production model results

In Figure 5.8 we compare the observed evolution of PAN and PPN with the modeled production of PAN and PPN according to the integrated steady-state mass balance equation described above. For each plume, we show several different sets of inputs. In the blue line models for PAN (Figure 5.8a, b, and c), we use the full set of observations and best estimates for β and OH. This includes production from the OH oxidation of acetaldehyde and methylglyoxal, and the photolysis of biacetyl and methylglyoxal according to the observed j-values. The orange line model restricts production to that of acetaldehyde only, and the red line model includes production from all precursors, but j-biacetyl is set to a constant value for each plume to match observed biacetyl loss (Figure 5.5) .

The full model with observed j-values (blue line in Figure **??**) overestimates PAN production in all three plumes, though it is within the observed error for the Taylor Creek plume. The orange line model suggests that acetaldehyde oxidation can account for the majority of the PAN production, and that the photolysis of biacetyl is an important secondary contributor in these plumes. This is consistent with the findings from Liu et al. (2016) and Müller et al. (2016) based on smaller plumes sampled over the southeastern US. The timeseries of the production of PA radicals in Figure **??**d-f confirm the likely importance of acetaldehyde and biacetyl. Methylglyoxal oxidation and photolysis is a minor contributor except in the beginning of the Silver Creek plume where observed j-methylglyoxal is enhanced in the second plume transect (Figure 5.4c), along with j-biacetyl (Figure 5.4c) and j-NO_2 (not shown). Setting the j-biacetyl to lower constant values (red line) improves the predicted PAN, but still overestimates the Bear Trap and Silver Creek plumes. The j-biacetyl calculation from observed actinic flux is underconstrained. Measured absorption cross sections across the relevant wavelength spectrum (~300 -

450) agree well (Horowitz et al. 2001), but wavelength resolved quantum yields of CH_3CO from biacetyl have not been measured. Instead, an average quantum yield of 0.16 across the wavelength region has been inferred from observations of biacetyl loss (Plum et al. 1983) and effective j-biacetyl has been estimated as $0.035 * \text{j-}NO_2$ from outdoor chamber observations (Klotz et al. 2001). Rajakumar et al. (2008) measured a high pressure limit CH_3CO quantum yield of 1 at 248 nm, but this measurement is not extensible to the lower and mid-troposphere. Additionally, the PTR measurement of biacetyl has a large uncertainty, both in the calibration conversion for number of counts per sec (ncps) to mixing ratio and in the fraction of the mass that is attributed to biacetyl. While the lab measurements by Koss et al. (2018) suggest that a large fraction, ~0.9, of the $C_4H_6O_2$ peak should be attributed to biacetyl at the emission source, we do not have good constraints on if or how this fraction evolves with plume aging. If that fraction decreased due to biacetyl loss and/or increasing $C_4H_6O_2$ fragments from larger VOCs, then the total production of PAN from biacetyl would likewise decrease. Under these conditions the uncertainty or error in the j-biacetyl values would not need to be as large. Given these possibilities, we conclude that biacetyl is likely an important PAN precursor in western wildfire smoke plumes, but more work needs to be done to constrain the wavelength-resolved biacetyl CH_3CO quantum yield and to quantify the abundance and evolution of biacetyl in smoke plumes.

The main differences in the observed rates of PAN production in these three plumes can be explained by the differences in the OH concentrations and the possible contribution from biacetyl. The Taylor Creek plume model includes higher OH concentrations for the first 2 hours of aging compared to Bear Trap and Silver Creek (Figure 5.7a, b, c), and thus has a higher production rate of PAN. The relative NEMRs of acetaldehyde are similar for all three plumes, so OH concentration plays the largest role in the differing contribution of acetaldehyde to PA radical production (Figure 5.8d, e, and f). Initial biacetyl NEMRs are smallest in the Taylor Creek plume and decay to lower values over the estimated aging time. This means that uncertainty in the j-biacetyl values affects the Taylor Creek plume calculations least.

Figure **??**g-i present the observed and modeled PPN NEMRs. PPN is underpredicted with the best-constrained values of OH and β (blue line for PPN simulation), with production from propanal alone. One possible reason for this could be the misestimation of the propanal PTR fraction. Following the propanal fraction estimates from TOGA for the Taylor Creek and Bear Trap plumes (Figure A17) we assign different fractions to each plume here. Propanal is equal to ~0.15 times the PTR propanal+acetone measurement in Taylor Creek, but equal to ~0.1 times the PTR measurement for Bear Trap and Silver

Creek. Increasing this fraction to ~0.45 would bring the blue line model up closer to the observed PPN evolution in all three plumes, but this would be a factor of two higher than any fraction observed in smoke with the TOGA measurements. Another factor in the underestimate of PPN by the blue line model could be too large a loss rate for PPN. PPN does have a faster reaction rate with OH compared to PAN (k_{OH} ~3×10^{-13} cm^3 $molec.^{-1}$ s^{-1} versus k_{OH} ~3×10^{-14} cm^3 $molec.^{-1}$ s^{-1}), but this loss pathway is negligible for both species compared to the reaction of PA and PP radicals with NO, HO_2, or RO_2 and therefore should not affect the underprediction of PPN by the blue line model. There is no evidence for different reaction rates of PP versus PA with NO and other peroxy radicals; LaFranchi et al. (2009) applied the same β for their calculations of both PAN and PPN, and we follow the same convention here. LaFranchi et al. (2009) suggest that the rate coefficient of PA+RO_2 reaction could be underestimated by up to a factor of 3, but incorporating a larger PA+RO_2 reaction rate here would push β lower and drive further underpredictions of the PPN NEMRs. Additionally, at the NO_x abundances in these fresh plumes, even a factor of 3 increase in the PA+RO_2 rate would only change β by ~0.05.

The underprediction of PPN by a model that includes propanal as the only PP radical source suggests other sources of the PP radical. Propanal (CH_3CH_2CHO) is considered the dominant source in most environments (Roberts et al. 2001), but ethylglyoxal (CH_3CH_2COCHO) is another potential PP radical precursor. Ethylglyoxal both photolyzes and reacts with OH to produce PP radicals with a yield of 1, with j-values similar to methylglyoxal photolysis and OH reaction rates similar to propanal (MCM v3.3.1). Along with other dicarbonyls such as glyoxal and biacetyl, ethylglyoxal has been measured in cigarette smoke (Moree-Testa and Saint-Jalm 1981), Brazilian charcoal burning plants (Anunciação et al. 2012), and pine and oak residential fire place burning (Schauer et al. 2001), so it is likely that it is emitted by wildfires as well. It can also be formed as a product of OH oxidation of ethylbenzene (Obermeyer et al. 2009), though the production rate of ethylglyoxal is likely too slow and the abundances of ethylbenzene observed during WE-CAN are too small to be a significant source of ethylglyoxal. In existing measurements of ethylglyoxal in ambient smoke (using derivatized filter sampling in a Mediterranean shrubland) ethylglyoxal is present in similar abundances to propanal (Garcia-Hurtado et al. 2014). However, ethylglyoxal is not identified by Hatch et al. (2015), Gilman et al. (2015) or Koss et al. (2018) all of whom identified hundreds of VOCs in smoke including several isomers of ethylglyoxal. These studies all used high time-resolution GC-MS and/or PTR-ToF-MS measurements techniques though, and it is possible that ethylglyoxal is difficult to detect and quantify using these methods. Fragmentation in PTR drift tubes similar to known issues for glyoxal (Stönner et al. 2017) and

non-elution/inefficient separation or low recovery from GC columns (Aschmann et al. 2014; Salvador et al. 2016) could complicate or prevent detection of ethylglyoxal in these common high time resolution VOC measurement techniques for smoke.

MEK can also form the PP radical, but this is a minor OH oxidation pathway (∼8%) with a relatively slow rate (MEK lifetime ∼weeks). Photolysis and OH oxidation of 3-pentanone/diethyl ketone are additional PP radical formation pathways, and 2-methyl-3-pentanone and other C_6 diones are yet more potential PP radical sources, but the abundances of these precursors combined with their oxidation or photolysis rates make them unlikely candidates to explain the large additional source of PP radicals needed in fresh smoke plumes. Likewise, *cis*-3-hexan-1-ol has been shown to be a PP radical precursor (Grosjean et al. 1993), but abundances of the $C_6H_{12}O$ peak in the PTR are too small for this molecule to be an important precursor even if measurements at that peak solely consisted of *cis*-3-hexan-1-ol.

Thus, we hypothesize the presence of ethylglyoxal in WE-CAN sampled plumes in quantities large enough to be a significant immediate PPN precursor in fresh smoke. To explore this hypothesis, we add an ethylglyoxal production term to the PPN production model with the abundances as propanal based on Garcia-Hurtado et al. (2014). We use the observed j-methylglyoxal as the j-ethylglyoxal, with a yield of 1 PP radical, and use a constant OH rate coefficient of 1.39×10^{-11} cm^3 $molec.^{-1}$ s^{-1} (MCM v3.3.1). The red line in Figure **??**g-i shows the result of this calculation. The model can simulate the observed magnitude of the final PPN NEMR in the Taylor Creek plume, though the evolution is not well-simulated. However, for the other two plumes the inclusion of ethylglyoxal overpredicts PPN production. Figure **??**j-l breaks down the potential ethylglyoxal PP radical source from photolysis (dark grey) and OH oxidation (light grey). The photolysis source dominates in the Bear Trap and Silver Creek plumes.

There is enormous uncertainty in the theoretical exercise in adding ethylglyoxal. The abundances of ethylglyoxal could be wrong, the assumption that j-ethylglyoxal is equivalent to j-methylglyoxal could be incorrect, and the OH oxidation rate coefficient does not include a temperature dependence. Though the literature basis is thin, the likelihood of direct emissions from biomass burning, potential abundances similar to propanal, and PP production rate coefficients fast enough to be important in fresh smoke all point towards to ethylglyoxal as a potentially important PPN precursor in fresh wildfire smoke worth future investigation.

5.3.4 Uncertainties and Discussion

Uncertainties abound in this analysis. Uncertainty in the estimated physical age, and in the validity of the pseudo-Lagrangian pattern assumptions could mean we are misestimating the magnitude or rate of PAN and PPN production in the observations. We note that the plumes in this analysis were all large, high, and fresh smoke plumes from fires burning in midafternoon. APN evolution may be different in nighttime plumes, in older plumes, or in plumes injected at or near ground-level. WE-CAN was not able to sample the evolution of these smoke plume types, and future analyses should aim to explore APN evolution in those contexts as well. Individual uncertainties in the PAN and PPN production model inputs offer enough wiggle room that it is tempting to try to tailor the model outputs to exactly fit the PAN and PPN evolution. However, several of the inputs are reasonably well constrained. Even though we do not have measurements of HO_2 and RO_2, we can constrain β to a fairly small range given those we do have of NO and NO_2. Our OH concentration timeseries are generally consistent with the smoke literature, and are constrained by independent VOC measurements with varying lifetimes against OH oxidation. Most of the rate coefficients used above have also been well-studied in the lab.

The two parameters that contribute the most uncertainty to the model are the oVOC precursor abundances and the j-values. Additional laboratory measurements of the biacetyl quantum yield across a full range of temperatures and wavelengths may be needed to more precisely and accurately estimate the photolysis of biacetyl in smoke. If the attribution of specific PTR m/z peaks to different isomers is more complicated than the treatment presented here, then the enhancements of several PAN and PPN precursors could be quite a bit different than currently estimated. The possibility of an unquantified compound such as ethylglyoxal being present in smoke may be one example of how attribution could be more complicated. Ethylglyoxal and biacetyl are isomers, and our assumption of 87% attribution of the PTR $C_4H_6O_2$ (m = 86 g mol $^{-1}$) peak to biacetyl is close to an upper bound for the abundance of biacetyl. If some portion of the mixing ratio quantified at that peak were instead ethylglyoxal, then that could have the effect of reducing the overestimation of PAN by the model at the same time as reducing the underestimation of PPN. Measurements of ethylglyoxal via commonly used techniques are likely difficult, but a proton-transfer ion-trap mass spectrometry instrument did detect a significant fraction (>50%) of unidentified contribution to the $C_4H_6O_2$ peak in a series of lab burns (Yokelson et al. 2013b). Of course the sensitivity of the PTR to distinct compounds at the same m/z such as ethylglyoxal and biacetyl may differ, with important ramifications for the conversion from number of counts per second to mixing ratio. These sensitivity differences already contribute to large individual uncertainties (> 40%

) in many of the PTR m/z measurements though. Future fast measurements tuned and calibrated to this specific set of APN precursor species may be needed to further our understanding of the PAN and PPN formation mechanisms in smoke. Lastly, it is possible that this simplified model framework may be missing other important APN precursors. Along these lines, detailed full atmospheric chemistry simulations of individual smoke plumes, though outside the scope of this analysis, could yield further insights into the production of PAN and PPN in fresh wildfire smoke plumes as well.

5.4 Conclusions

We have presented an analysis of the evolution of PAN and PPN in 8 pseudo-Lagrangian sampled smoke plumes in the western US, as well an observationally constrained steady-state production model of PAN and PPN in fresh western wildfire smoke plumes. We have three main findings.

(1) Corrected for dilution, both PAN and PPN abundances increase in all plumes over the first several hours of observed aging. The rate of increase for PAN NEMRs is between 0.0006 and 0.002 ppbv/ppbv CO hr^{-1} and in the same range as observations of PAN production in smoke across a range of ecosystems, from southern California to boreal Canada to the tropical Yucatan.

(2) Acetaldehyde is the dominant immediate PAN precursor in large western wildfire smoke plumes, with biacetyl also serving as an important precursor. To our knowledge this is the first time these conclusions have been drawn for smoke from an observational framework and it suggests that biacetyl should be included in models of smoke plume evolution. The relative importance of biacetyl is determined by both its abundance and evolution as well as its photolysis rate. Further work is needed to more accurately and precisely measure the *in situ* mixing ratios of biacetyl in smoke. More confidence in the wavelength-resolved quantum yield of biacetyl would also reduce the uncertainty in the contribution from biacetyl to PAN production.

(3) Propanal is an important immediate PPN precursor in fresh wildfire smoke. We also hypothesize that at least one other PPN precursor is needed to explain PPN production, and suggest that this precursor may be ethylglyoxal. Very few *in situ* measurements of ethylglyoxal exist, possibly due to measurement technique constraints, but future lab and field studies might assess whether ethylgloxal can be quantified with high temporal resolution in wildfire smoke and whether its hypothesized contribution to PPN production is reasonable.

CHAPTER 6

CONCLUSIONS AND NEXT STEPS

6.1 CONCLUSIONS

The WE-CAN field intensive sampled fresh smoke from 23 identified large wildfires in the western U.S. during August and September 2018. Pseudo-Lagrangian sampling was done for about half of these fires. Additionally, mixed and older smoke from indeterminate sources was sampled in the free troposphere as well as in the California Central Valley where it mixed with anthropogenic emissions.

Using a large cross section of the suite of chemical and physical measurements made onboard the NSF/NCAR C-130 aircraft, here I have presented three analyses investigating the emissions and evolution of reactive N in wildfire smoke plumes, separated into chapters based on three manuscripts. Chapter 2 describes the common measurements and methods used across multiple analyses. In Chapter 3, I use all available *in situ* measurements of N compounds in the freshest smoke sampled near each fire to investigate the emissions of reactive N by western U.S. wildfires and compare estimated emission factors to literature compilations and previous lab and field measurements. In Chapter 4, I employ measurements taken during pseudo-Lagrangian sampling patterns on a subset of fires to explore the loss timescales of NH_3 and the factors influencing its partitioning to the particle-phase in smoke. And lastly, in Chapter 5 I use measurements from this same set of pseudo-Lagrangian sampled plumes to empirically determine the dominant precursors of PAN and PPN in fresh western wildfire smoke plumes. The key findings of each Chapter are as follows:

6.1.1 Chapter 3 key findings

I found that reduced N species contributed a large proportion (39 = 80%, median = 66%) of total reactive N (N_r) emissions in the plumes sampled.This was not necessarily expected since the fires sampled were a subset of the largest wildfires in the western U.S. during summer 2018 and were sampled during the midafternoon, typically the most active period of the day. Large, intensively burning fires are expected to include the most flaming combustion conditions, which would lead to higher (and assumed dominant) emission of oxidized N. NH_3 and NO_x are two of the most abundant N_r species in wildfire smoke, though I observe significant abundances of pNH_4, pNO_3, PAN, and organic nitrates even in these youngest plume samples. The presence of PAN in particular is evidence for rapid chemistry that changes the form and distribution of N_r within minutes in these plumes. Due to this rapid chemistry, I compare total measured oxidized N (ΣNO_y) and total measured ammonia (ΣNH_x) with

common metrics of fire characteristics, such as MCE, rather than NO_x and NH_3 by themselves. The ratio of $\Sigma NH_x/\Sigma NO_y$ generally decreases with increasing MCE, qualitatively consistent with previous research, and a similar relationship between $\Sigma NH_x/\Sigma NO_y$ and the HNCO fraction further suggest that combustion processes and conditions drive some of the variability in the distribution of N_r between reduced and oxidized forms. Through the negative correlation between $\Sigma NH_x/\Sigma NO_y$ and the total measured ΣN_r, I propose that fuel N content/volatilization differences between fires may also contribute to the observed variability in $\Sigma NH_x/\Sigma NO_y$, though this interpretation is complicated somewhat by unquantifiable influence from denitrification reactions ($N_r \rightarrow N_2$) that are likely more prevalent under more flaming combustion conditions.

In comparing our emission factor estimates with previous literature and lab and field measurements I find that for similar fuel types ΣNH_x EFs are of the same magnitude or larger than lab-based NH_3 EFs, whereas ΣNO_y EFs are on average smaller than lab-based NO_x EFs. Lower MCEs observed for WE-CAN fires compared to lab burns may explain some of these differences. Missing or uncertain observations of the full suite of oxidized N species may also bias the WE-CAN ΣNO_y EFs lower. In general, our data offer a significant expansion in the number of wildfires sampled for most of these fuel types.

6.1.2 Chapter 4 key findings

I characterized the evolution of gas-phase NH_3 and investigated some of the complexity in the partitioning of NH_3 to pNH_4. NH_3 mixing ratios decrease in fresh smoke plumes in most of the sampled plumes, faster than can be explained by dilution alone, and concurrent increases in observed submicron pNH_4 from the AMS are able to account for this loss in many plumes. While the limited existing literature on NH_3 evolution in smoke tends to estimate a lifetime or effective lifetime for NH_3 loss, I recognize the complexity in this term: NH_3 is likely lost from the gas phase through an equilibrium process dependant on T and RH that happens concurrent with ongoing dilution and changing inorganic and organic acids abundances. Thus I describe an e-folding loss timescale to quasi-equilibrium for NH_3 gas-particle partitioning that is on the order of tens of minutes to several hours in the fresh smoke plumes sampled. I find empirical evidence for the association of NH_3 and HNO_3 to form NH_4NO_3 through the positive relationship between the pNH_4 fraction of ΣNH_x and the ΣNO_z fraction of ΣNO_y and examine the thermodynamic context for the formation of NH_4NO_3 by calculating the K_p ratio. Under the assumption that this equilibrium is independent from aerosol mixing state, phase separation, or pH, I find that many of our *in situ* measurements are far from equilibrium, both super- and sub-

saturated with respect to NH_4NO_3. Fresh, dense plumes injected at higher altitudes (and lower temperatures) are more likely to favor NH_4NO_3 formation. The abundant organic acid ions measured by the PILS also suggest the presence of NH_4-organic salts in the plumes sampled. Lastly, in smoke with chemical ages older than ~1 day, I find evidence for the presence of NH_4NO_3 via the negative relationship between the environmental temperature and both pNH$_4$ and pNO$_3$ fractions. This again suggests that smoke injected higher in the free troposphere favors the formation of NH_4NO_3, consistent with the findings of Paulot et al. (2017).

6.1.3 Chapter 5 key findings

I observe dilution corrected increases in PAN and PPN in all pseudo-Lagrangian plumes sampled. The rate of increase is in the same range as observations of PAN production in smoke across a range of ecosystems, from southern California to boreal Canada to the tropical Yucatan. In three case studies, a simple observationally-constrained PAN and PPN production model suggests that acetaldehyde is the dominant immediate PAN precursor in large western wildfire smoke plumes, with biacetyl also serving as an important precursor. To my knowledge this is the first time these conclusions have been drawn for smoke from an observational framework and it suggests that biacetyl should be included in models of smoke plume evolution. The relative importance of biacetyl is determined by both its abundance and evolution as well as its photolysis rate. With respect to PPN, I find that propanal is an important immediate PPN precursor in fresh wildfire smoke. Unexpectedly, I also find that at least one other immediate PPN precursor is likely needed to explain PPN production, and suggest that this precursor may be ethylglyoxal. However, very few *in situ* measurements of ethylglyoxal exist to test this hypothesis.

6.2 Next Steps

There are five general areas of future extensions to this work, ranging from individual scale analyses to coordinated community efforts. There are extensions to this set of observational analyses, some of which are already being undertaken. Modeling efforts at plume, regional, and global scales will help place the WE-CAN dataset in a broader context. Satellite observations could be used to extend these analyses on larger spatiotemporal scales. Additional *in situ* observations may be needed to capture the full range of real world smoke chemistry and assess the representativeness of our current observations. And lastly, laboratory studies will continue to be needed to constrain individual reactions,

explore complex chemistry in controlled contexts, and to develop new capabilities for quantifying key atmospheric constituents. Briefly, I will explore a few possible next steps in each of these areas.

6.2.1 Observational analysis extensions

The extraordinary set of measurements made by all the WE-CAN research teams is the singular reason this work was even possible in the first place. Sampling so many fires with such a comprehensive set of observations has opened the door to analyses across several or many plumes, instead of relying just on individual case studies. There are several ongoing analyses that tie directly into the understanding of reactive N in wildfire smoke. A manuscript describing the evolution and distribution of oxidized nitrogen in greater detail is in preparation (Julieta Juncosa Calahorrano, personal communication), as well as a manuscript exploring the production of O_3 in the WE-CAN smoke plumes (Emily Fischer, personal communication).

I investigated the formation of PAN and PPN in fresh smoke, but the same set of measurements may be used to ask whether PAN and PPN are in steady state in older smoke. The main challenges are likely in the estimating the concentration of OH in these older plumes, as well as the concentrations of HO_2 and RO_2 which may become more important to the fraction of AP radicals lost as NO_x dilutes and oxidizes. Additional oVOC precursors may become important in older smoke as well, as more reactive PAN precursor abundances decrease.

More work is needed to understand the bulk aerosol composition measurements made during WE-CAN. Empirical analyses attempting to separately estimate the fraction of inorganic and organic AMS pNO_3 are ongoing, and similar analyses that may be able to separate AMS pNH_4 between the pNH_4 contribution from NH_4 salts and reduced N compounds could be undertaken as well. More work is also needed to better integrate the PILS data into future aerosol composition analyses. Temporal filtering of higher-frequency data may be necessary when directly comparing PILS measurements with the rest of the dataset. While I find support for the idea that NH_4-organic salts are present in WE-CAN plumes, more work could be done using the PILS data to link gas-phase organic acids to the particle-phase measurements.

6.2.2 Modeling

Like most atmospheric science field projects, WE-CAN observations are a snapshot in time across a subset of the phenomena (in this case wildfires). Atmospheric modeling efforts will be needed to help assess the representativeness of these observations to the broader set of western U.S. wildfire smoke

plumes, interrogate updated knowledge about chemical mechanisms, and understand the larger impacts of western U.S. wildfire smoke both regionally and globally. This modeling will need to be done on detailed plume scales all the way up to regional and global scales. The thermodynamic equilibria inherent to both NH_3 partitioning and the formation of APNs reinforces the importance of not only getting the emissions of these species correct, but also estimating the injection height (and therefore ambient temperature) correctly as well, especially in large scale models.

Models employing detailed chemical mechanisms such as the Master Chemical Mechanism (MCM Jenkin et al. 2003) and the Generator of Explicit Chemistry and Kinetics of Organics in the Atmosphere (GECKO-A) and/or detailed aerosol partitioning mechanisms such as ISORROPIA II (Fountoukis and Nenes 2007) or E-AIM (Wexler and Clegg 2002) will be important for assessing whether our empirical understanding of smoke chemistry mechanisms is consistent with a more holistic representation. Smoke plumes are extraordinarily complex and difficult to model, but detailed model simulations can help answer questions such as what fraction of APNs do we capture with PAN and PPN? Smoke contains hundreds of VOC species in appreciable quantities (*e.g.* Hatch et al. 2015), it would make sense that other APNs are being formed as well (Altshuller 1993; Yokelson et al. 2009). And can we treat NH_4NO_3 thermodynamic equilibrium separately from aerosol mixing state? And what is the influence of pH of aerosol composition?

6.2.3 Satellite observations

Capabilities in retrieving column observations of PAN and NH_3 from satellite instruments are continually improving. Notably, the Cross-track Infrared Sounder (CrIS) instrument onboard the Suomi-NPP satellite holds promise for higher sensitivity and higher spatial resolution retrievals compared to previous observations from the Tropospheric Emission Spectrometer (TES) and the Infrared Atmospheric Sounding Interferometer (IASI). Higher fidelity retrievals of PAN and NH_3 can be combined with CrIS retrievals of CO to extend the WE-CAN observations. Preliminary work (Julieta Juncosa Calahorrano, personal communication) shows that CrIS retrievals can capture both the production of PAN as well as the loss of NH_3 in individual smoke plumes. The possibility of extending production and loss timescale analyses across many plumes and years is exciting. Larger datasets from these analyses may also be able to leverage other satellite products estimating differences in burn conditions with fire radiative power and fuel type maps to tease out broader associations than can be done with limited *in situ* observations.

Improved satellite retrievals of PAN and NH_3 in smoke may also lend themselves towards another type of analysis. Deposition of N from smoke is already important to sensitive ecosystems, and better, more spatially dense, satellite retrievals combined with regional and global scale modeling could result in better estimation of N deposition from smoke and more confidence in our ability to predict future changes in N deposition due to changes in wildfire frequency or magnitude.

6.2.4 Additional in situ observations

WE-CAN sampled a large number of fires, but due to aircraft and logistical constraints these fires were nearly all sampled during midafternoon while emitting smoke into the upper boundary layer or free troposphere. This may bias our results towards large fresh smoke plumes emitted by actively burning fires. Therefore a good question is: Are our observations broadly representative or not? Sampling natural experiments such as fires will often lead to over- and under-sampling of certain processes or types of fires. The atmospheric science community identified wildfire smoke as a joint focus area several years ago, and a series of other aircraft, ground, and lab studies have been undertaken that can augment the findings from WE-CAN. Specifically, the Fire Influence on Regional to Global Environments 2016 (FIREX-2016) laboratory studies, the Fire Influence on Regional to Global Environments and Air Quality (FIREX-AQ) field project in summer 2019, and the Fire and Smoke Model Evaluation Experiment (FASMEE) in summer and fall 2019 have all gathered additional *in situ* and remote sensing observations in smoke. FASMEE contained sampling of smoke from large scale prescribed burns, FIREX-AQ sampled smoke further into nighttime and likely captured plume evolution from the same fire over multiple days, and FIREX-2016 included many different western U.S. fuels as well as chamber evolution experiments. Ground sampling teams during both WE-CAN and FIREX-AQ were able to capture plumes that either were not lofted into the free troposphere or settled back into valleys overnight. The combination of data from these projects along with WE-CAN can be used to critically assess whether the full range of fire behavior, fuel types, and atmospheric processing was captured.

The analyses in Chapter 3 and 4 would not have been possible without high time resolution and accurate gas-phase NH_3 measurements, and more observations of the timescales and forms of NH_3 partitioning in biomass burning smoke could help improve our understanding of wildfire smoke's impact on radiative balance (Paulot et al. 2017). There is a need for more *in situ* observations of NH_3 evolution, not only in this region but also for boreal and tropical regions. Fires in these other regions can have very different emission ratios of reactive nitrogen species (*e.g.* Akagi et al. 2011). Paulot et al. (2017)

and this study have offered evidence suggesting larger ratios of NO_x/NH_3 emitted may be more conducive to faster NH_3 partitioning via formation of NH_4NO_3 and additional *in situ* observations could help test the generality of this inference.

6.2.5 Laboratory measurements

My work has identified a need for new laboratory experiments, specifically with respect to PAN and PPN formation mechanisms. I suggest three different types of experiments.

While multiple measurements of biacetyl cross sections as a function of wavelength are consistent with each other (Horowitz et al. 2001), to my knowledge the quantum yield of dissociation of biacetyl as a function of wavelength in the tropospherically-relevant spectral region has not been measured. Average quantum yields across the absorption region have been estimated from photolysis chamber experiments, and a specific quantum yield at 248 nm has been measured by Rajakumar et al. (2008). If biacetyl is potentially the second most important PAN precursor in fresh wildfire smoke, then we need better constraints on its photolysis rates.

The other uncertainty in the contribution of biacetyl to PAN production is uncertainty in the quantification of its mixing ratio in smoke by the PTR-ToF-MS. Further work is needed to more accurately and precisely measure mixing ratios of biacetyl in smoke. While comparison between different VOC measurement techniques in very fresh smoke from lab burns has attributed $\sim 90\%$ of measured mass to biacetyl at the 86 ($C_4H_6O_2$) m/z (Koss et al. 2018), future aging experiments of smoke that include photolysis may be able to test this attribution in more chemically aged smoke.

Lastly, future lab studies may investigate the quantification of ethylglyoxal in smoke, and could place better constraints on its OH oxidation rate coefficient and photolysis rate. It is not clear if ethylglyoxal can be detected or quantified by the current commonly used VOC measurement techniques (Joost de Gouw, personal communication). All published quantification of ethylglyoxal to date has been done via derivatized filter sampling. However, these methods may not be reliable for all carbonyls and dicarbonyls (Apel et al. 2003). Ethylglyoxal and biacetyl are isomers ($C_4H_6O_2$), and so one question that a lab experiment could address is: Could some of the detection of biacetyl in a PTR actually be attributed to ethylglyoxal? The previously mentioned apportioning of the $C_4H_6O_2$ m/z measurement PTR measurements was done with a gas chromatograph (GC) in line with the PTR (Abigail Koss, personal communication). If the GC column did not transmit ethylglyoxal then it would not have been included in the apportioning. In the lab studies described by Yokelson et al. (2013b), a proton ion-trap mass spectrometer quantified "unknown mass at 86 m/z" , offering one small piece of evidence that

perhaps ethylglyoxal could be detected at that mass. Of course other dicarbonyls can fragment in the PTR and quantification then becomes complex and uncertain (Stönner et al. 2017). In summary, some simple experiments attempting to detect and quantify ethylglyoxal with multiple different techniques in the lab could provide immediate insight into how likely it is that ethylglyoxal's contribution to PPN production is reasonable.

References

Abatzoglou, J. T., 2011: Development of gridded surface meteorological data for ecological applications and modelling. *International Journal of Climatology*, **33 (1)**, 121–131, doi: 10.1002/joc.3413, URL https://rmets.onlinelibrary.wiley.com/doi/abs/10.1002/joc.3413.

Adams, C., et al., 2019: Satellite-derived emissions of carbon monoxide, ammonia, and nitrogen dioxide from the 2016 Horse River wildfire in the Fort McMurray area. *Atmospheric Chemistry and Physics*, **19 (4)**, 2577–2599, doi: https://doi.org/10.5194/acp-19-2577-2019, URL https://www.atmos-chem-phys.net/19/2577/2019/acp-19-2577-2019.html.

Akagi, S. K., R. J. Yokelson, C. Wiedinmyer, M. J. Alvarado, J. S. Reid, T. Karl, J. D. Crounse, and P. O. Wennberg, 2011: Emission factors for open and domestic biomass burning for use in atmospheric models. *Atmospheric Chemistry and Physics*, **11 (9)**, 4039–4072, doi: https://doi.org/10.5194/acp-11-4039-2011, URL https://www.atmos-chem-phys.net/11/4039/2011/acp-11-4039-2011.html.

Akagi, S. K., et al., 2012a: Evolution of trace gases and particles emitted by a chaparral fire in California. *Atmospheric Chemistry and Physics*, **12 (3)**, 1397–1421, doi: https://doi.org/10.5194/acp-12-1397-2012, URL https://www.atmos-chem-phys.net/12/1397/2012/acp-12-1397-2012.html, publisher: Copernicus GmbH.

Akagi, S. K., et al., 2012b: Measurements of reactive trace gases and variable O $_3$ formation rates in some South Carolina biomass burning plumes. *Atmospheric Chemistry and Physics Discussions*, **12 (9)**, 25 255–25 328, doi: 10.5194/acpd-12-25255-2012, URL https://www.atmos-chem-phys-discuss.net/12/25255/2012/.

Altshuller, A. P., 1993: PANs in the Atmosphere. *Air & Waste*, **43 (9)**, 1221–1230, doi: 10.1080/1073161X.1993.10467199, URL http://www.tandfonline.com/doi/abs/10.1080/1073161X.1993.10467199.

Alvarado, M. J., et al., 2010: Nitrogen oxides and PAN in plumes from boreal fires during ARCTAS-B and their impact on ozone: an integrated analysis of aircraft and satellite observations. *Atmospheric Chemistry and Physics*, **10 (20)**, 9739–9760, doi: https://doi.org/10.5194/acp-10-9739-2010, URL https://www.atmos-chem-phys.net/10/9739/2010/, publisher: Copernicus GmbH.

Alvarado, M. J., et al., 2015: Investigating the links between ozone and organic aerosol chemistry in a biomass burning plume from a prescribed fire in California chaparral. *Atmospheric Chemistry and Physics*, **15 (12)**, 6667–6688, doi: https://doi.org/10.5194/acp-15-6667-2015, URL https://www.atmos-chem-phys.net/15/6667/2015/, publisher: Copernicus GmbH.

Andreae, M. O., 2019: Emission of trace gases and aerosols from biomass burning – an updated assessment. *Atmospheric Chemistry and Physics*, **19 (13)**, 8523–8546, doi: https://doi.org/10.5194/acp-19-8523-2019, URL https://www.atmos-chem-phys.net/19/8523/2019/acp-19-8523-2019.html.

Andreae, M. O., et al., 1988: Biomass-burning emissions and associated haze layers over Amazonia. *Journal of Geophysical Research: Atmospheres*, **93 (D2)**, 1509–1527, doi: 10.1029/JD093iD02p01509, URL https://agupubs.onlinelibrary.wiley.com/doi/abs/10.1029/JD093iD02p01509, _eprint: https://agupubs.onlinelibrary.wiley.com/doi/pdf/10.1029/JD093iD02p01509.

Andrews, S. J., et al., 2016: A comparison of very short lived halocarbon (VSLS) and DMS aircraft measurements in the tropical west Pacific from CAST, ATTREX and CONTRAST. *Atmospheric Measurement Techniques*, **9 (10)**, 5213–5225, doi: https://doi.org/10.5194/amt-9-5213-2016, URL https://www.atmos-meas-tech.net/9/5213/2016/.

Anunciação, D. S., E. T. Sousa, A. B. d. Carvalho, and P. A. P. Pereira, 2012: Emission profiles of carbonyl compounds at a Brazilian charcoal plant. *Journal of the Brazilian Chemical Society*, **23 (9)**, 1606–1613, doi: 10.1590/S0103-50532012005000025, URL http://www.scielo.br/scielo.php?script=sci_abstract&pid=S0103-50532012000900004&lng=en&nrm=iso&tlng=en, publisher: Brazilian Chemical Society.

Apel, E. C., A. J. Hills, R. Lueb, S. Zindel, S. Eisele, and D. D. Riemer, 2003: A fast-GC/MS system to measure C2 to C4 carbonyls and methanol aboard aircraft. *Journal of Geophysical Research: Atmospheres*, **108 (D20)**, doi: 10.1029/2002JD003199, URL http://agupubs.onlinelibrary.wiley.com/doi/abs/10.1029/2002JD003199, _eprint: https://onlinelibrary.wiley.com/doi/pdf/10.1029/2002JD003199.

Apel, E. C., et al., 2015: Upper tropospheric ozone production from lightning NOx-impacted convection: Smoke ingestion case study from the DC3 campaign. *Journal of Geophysical Research: Atmospheres*, **120 (6)**, 2505–2523, doi: 10.1002/2014JD022121, URL http://agupubs.onlinelibrary.wiley.com/doi/abs/10.1002/2014JD022121, _eprint: https://onlinelibrary.wiley.com/doi/pdf/10.1002/2014JD022121.

Aschmann, S. M., N. Nishino, J. Arey, and R. Atkinson, 2011: Kinetics of the Reactions of OH Radicals with 2- and 3-Methylfuran, 2,3- and 2,5-Dimethylfuran, and E- and Z-3-Hexene-2,5-dione, and Products of OH + 2,5-Dimethylfuran. URL https://pubs.acs.org/doi/pdf/10.1021/es103207k, archive Location: world Library Catalog: pubs.acs.org Publisher: American Chemical Society, doi: 10.1021/es103207k.

Aschmann, S. M., N. Nishino, J. Arey, and R. Atkinson, 2014: Products of the OH Radical-Initiated Reactions of Furan, 2- and 3-Methylfuran, and 2,3- and 2,5-Dimethylfuran in the Presence of NO. *The Journal of Physical Chemistry A*, **118 (2)**, 457–466, doi: 10.1021/jp410345k, URL https://doi.org/10.1021/jp410345k, publisher: American Chemical Society.

Atkinson, R., 1986: Kinetics and mechanisms of the gas-phase reactions of the hydroxyl radical with organic compounds under atmospheric conditions. *Chemical Reviews*, **86 (1)**, 69–201, doi: 10.1021/cr00071a004, URL https://pubs.acs.org/doi/abs/10.1021/cr00071a004, publisher: American Chemical Society.

Atkinson, R., D. L. Baulch, R. A. Cox, R. F. Hampson, J. A. Kerr, M. J. Rossi, and J. Troe, 1997: Evaluated Kinetic and Photochemical Data for Atmospheric Chemistry: Supplement VI. IUPAC Subcommittee on Gas Kinetic Data Evaluation for Atmospheric Chemistry. *Journal of Physical and Chemical Reference Data*, **26 (6)**, 1329–1499, doi: 10.1063/1.556010, URL https://aip.scitation.org/doi/10.1063/1.556010, publisher: American Institute of Physics.

Atkinson, R., et al., 2004: Evaluated kinetic and photochemical data for atmospheric chemistry: Volume I - gas phase reactions of O_x, HO_x, NO_x and SO_x species. *Atmospheric Chemistry and Physics*, **4 (6)**, 1461–1738, doi: https://doi.org/10.5194/acp-4-1461-2004, URL https://www.atmos-chem-phys.net/4/1461/2004/, publisher: Copernicus GmbH.

Atkinson, R., et al., 2006: Evaluated kinetic and photochemical data for atmospheric chemistry: Volume II – gas phase reactions of organic species. *Atmospheric Chemistry and Physics*, **6 (11)**, 3625–4055, doi: 10.5194/acp-6-3625-2006, URL http://www.atmos-chem-phys.net/6/3625/2006/.

Baeza-Romero, M. T., D. R. Glowacki, M. A. Blitz, D. E. Heard, M. J. Pilling, A. R. Rickard, and P. W. Seakins, 2007: A combined experimental and theoretical study of the reaction between methylglyoxal and OH/OD radical: OH regeneration. *Physical Chemistry Chemical Physics*, **9 (31)**, 4114–4128, doi: 10.1039/B702916K, URL https://pubs.rsc.org/en/content/articlelanding/2007/cp/b702916k, publisher: The Royal Society of Chemistry.

Bahreini, R., et al., 2008: Design and Operation of a Pressure-Controlled Inlet for Airborne Sampling with an Aerodynamic Aerosol Lens. *Aerosol Science and Technology*, **42 (6)**, 465–471, doi: 10.1080/02786820802178514, URL https://doi.org/10.1080/02786820802178514.

Bahreini, R., et al., 2009: Organic aerosol formation in urban and industrial plumes near Houston and Dallas, Texas. *Journal of Geophysical Research: Atmospheres*, **114 (D7)**, doi: 10.1029/2008JD011493, URL https://agupubs.onlinelibrary.wiley.com/doi/abs/10.1029/2008JD011493.

Behera, S. N. and M. Sharma, 2010: Investigating the potential role of ammonia in ion chemistry of fine particulate matter formation for an urban environment. *Science of The Total Environment*, **408 (17)**, 3569–3575, doi: 10.1016/j.scitotenv.2010.04.017, URL http://www.sciencedirect.com/science/article/pii/S0048969710003955.

Benedict, K. B., A. J. Prenni, C. M. Carrico, A. P. Sullivan, B. A. Schichtel, and J. L. Collett, 2017: Enhanced concentrations of reactive nitrogen species in wildfire smoke. *Atmospheric Environment*, **148**, 8–15, doi: 10.1016/j.atmosenv.2016.10.030, URL http://www.sciencedirect.com/science/article/pii/S1352231016308378.

Benedict, K. B., et al., 2019: Volatile organic compounds and ozone in Rocky Mountain National Park during FRAPPÉ. *Atmospheric Chemistry and Physics*, **19 (1)**, 499–521, doi: https://doi.org/10.5194/acp-19-499-2019, URL https://www.atmos-chem-phys.net/19/499/2019/.

Boubel, R. W., E. F. Darley, and E. A. Schuck, 1969: Emissions from Burning Grass Stubble and Straw. *Journal of the Air Pollution Control Association*, **19 (7)**, 497–500, doi: 10.1080/00022470.1969.10466517, URL https://doi.org/10.1080/00022470.1969.10466517, publisher: Taylor & Francis _eprint: https://doi.org/10.1080/00022470.1969.10466517.

Bouwman, A. F., D. S. Lee, W. a. H. Asman, F. J. Dentener, K. W. V. D. Hoek, and J. G. J. Olivier, 1997: A global high-resolution emission inventory for ammonia. *Global Biogeochemical Cycles*, **11 (4)**, 561–587, doi: 10.1029/97GB02266, URL http://agupubs.onlinelibrary.wiley.com/doi/abs/10.1029/97GB02266, _eprint: https://onlinelibrary.wiley.com/doi/pdf/10.1029/97GB02266.

Bowman, D. M. J. S., et al., 2009: Fire in the Earth System. *Science*, **324 (5926)**, 481–484, doi: 10.1126/science.1163886, URL https://science.sciencemag.org/content/324/5926/481, publisher: American Association for the Advancement of Science Section: Review.

Bray, C. D., W. Battye, V. P. Aneja, D. Q. Tong, P. Lee, and Y. Tang, 2018: Ammonia emissions from biomass burning in the continental United States. *Atmospheric Environment*, **187**, 50–61, doi: 10.1016/j.atmosenv.2018.05.052, URL http://www.sciencedirect.com/science/article/pii/S1352231018303625.

Brégonzio-Rozier, L., et al., 2015: Gaseous products and secondary organic aerosol formation during long term oxidation of isoprene and methacrolein. *Atmospheric Chemistry and Physics*, **15 (6)**, 2953–2968, doi: 10.5194/acp-15-2953-2015, URL https://www.atmos-chem-phys.net/15/2953/2015/.

Burling, I. R., et al., 2010: Laboratory measurements of trace gas emissions from biomass burning of fuel types from the southeastern and southwestern United States. *Atmospheric Chemistry and Physics*, **10 (22)**, 11 115–11 130, doi: https://doi.org/10.5194/acp-10-11115-2010, URL https://www.atmos-chem-phys.net/10/11115/2010/acp-10-11115-2010.html.

Chen, L.-W. A., P. Verburg, A. Shackelford, D. Zhu, R. Susfalk, J. C. Chow, and J. G. Watson, 2010: Moisture effects on carbon and nitrogen emission from burning of wildland biomass. *Atmospheric Chemistry and Physics*, **10 (14)**, 6617–6625, doi: 10.5194/acp-10-6617-2010, URL https://www.atmos-chem-phys.net/10/6617/2010/.

Chen, X., et al., 2014: Seasonal ambient ammonia and ammonium concentrations in a pilot IMPROVE NHx monitoring network in the western United States. *Atmospheric Environment*, **91**, 118–126, doi: 10.1016/j.atmosenv.2014.03.058, URL http://www.sciencedirect.com/science/article/pii/S135223101400243X.

Chen, Y., et al., 2019: Response of the Aerodyne Aerosol Mass Spectrometer to Inorganic Sulfates and Organosulfur Compounds: Applications in Field and Laboratory Measurements. *Environmental Science & Technology*, **53 (9)**, 5176–5186, doi: 10.1021/acs.est.9b00884.

Christopher, S. A., J. Chou, J. Zhang, X. Li, T. A. Berendes, and R. M. Welch, 2000: Shortwave direct radiative forcing of biomass burning aerosols estimated using VIRS and CERES data. *Geophysical Research Letters*, **27 (15)**, 2197–2200, doi: 10.1029/1999GL010923, URL http://agupubs.onlinelibrary.wiley.com/doi/abs/10.1029/1999GL010923, _eprint: https://onlinelibrary.wiley.com/doi/pdf/10.1029/1999GL010923.

Coggon, M. M., et al., 2016: Emissions of nitrogen-containing organic compounds from the burning of herbaceous and arboraceous biomass: Fuel composition dependence and the variability of commonly used nitrile tracers. *Geophysical Research Letters*, **43 (18)**, 9903–9912, doi: 10.1002/2016GL070562, URL https://agupubs.onlinelibrary.wiley.com/doi/abs/10.1002/2016GL070562.

Collier, S., et al., 2016: Regional Influence of Aerosol Emissions from Wildfires Driven by Combustion Efficiency: Insights from the BBOP Campaign. *Environmental Science & Technology*, **50 (16)**, 8613–8622, doi: 10.1021/acs.est.6b01617, URL https://doi.org/10.1021/acs.est.6b01617, publisher: American Chemical Society.

Cook, P. A., et al., 2007: Forest fire plumes over the North Atlantic: p-TOMCAT model simulations with aircraft and satellite measurements from the ITOP/ICARTT campaign. *Journal of Geophysical Research: Atmospheres*, **112 (D10)**, doi: 10.1029/2006JD007563, URL

https://agupubs.onlinelibrary.wiley.com/doi/abs/10.1029/2006JD007563, _eprint: https://agupubs.onlinelibrary.wiley.com/doi/pdf/10.1029/2006JD007563.

Correia, A. W., C. A. I. Pope, D. W. Dockery, Y. Wang, M. Ezzati, and F. Dominici, 2013: Effect of Air Pollution Control on Life Expectancy in the United States: An Analysis of 545 U.S. Counties for the Period from 2000 to 2007. *Epidemiology*, **24 (1)**, 23–31, doi: 10.1097/EDE.0b013e3182770237, URL https://journals.lww.com/epidem/Fulltext/2013/01000/Effect_of_Air_Pollution_Control_on_Life_Expectancy.4.aspx.

Crutzen, P. J. and M. O. Andreae, 1990: Biomass Burning in the Tropics: Impact on Atmospheric Chemistry and Biogeochemical Cycles. *Science*, **250 (4988)**, 1669–1678, doi: 10.1126/science.250.4988.1669, URL https://science.sciencemag.org/content/250/4988/1669.

Crutzen, P. J., L. E. Heidt, J. P. Krasnec, W. H. Pollock, and W. Seiler, 1979: Biomass burning as a source of atmospheric gases CO, H 2 , N 2 O, NO, CH 3 Cl and COS. *Nature*, **282 (5736)**, 253–256, doi: 10.1038/282253a0, URL https://www.nature.com/articles/282253a0, number: 5736 Publisher: Nature Publishing Group.

Dammers, E., et al., 2019: NH3 emissions from large point sources derived from CrIS and IASI satellite observations. *Atmospheric Chemistry and Physics*, **19 (19)**, 12 261–12 293, doi: https://doi.org/10.5194/acp-19-12261-2019, URL https://www.atmos-chem-phys.net/19/12261/2019/, publisher: Copernicus GmbH.

Darley, E. F., F. R. Burleson, E. H. Mateer, J. T. Middleton, and V. P. Osterli, 1966: Contribution of Burning of Agricultural Wastes to Photochemical Air Pollution. *Journal of the Air Pollution Control Association*, **16 (12)**, 685–690, doi: 10.1080/00022470.1966.10468533, URL https://doi.org/10.1080/00022470.1966.10468533, publisher: Taylor & Francis _eprint: https://doi.org/10.1080/00022470.1966.10468533.

DeCarlo, P. F., et al., 2006: Field-Deployable, High-Resolution, Time-of-Flight Aerosol Mass Spectrometer. *Analytical Chemistry*, **78 (24)**, 8281–8289, doi: 10.1021/ac061249n, URL https://pubs.acs.org/doi/10.1021/ac061249n.

Farmer, D. K., A. Matsunaga, K. S. Docherty, J. D. Surratt, J. H. Seinfeld, P. J. Ziemann, and J. L. Jimenez, 2010: Response of an aerosol mass spectrometer to organonitrates and organosulfates and implications for atmospheric chemistry. *Proceedings of the National Academy of Sciences*, **107 (15)**, 6670–6675, doi: 10.1073/pnas.0912340107, URL https://www.pnas.org/content/107/15/6670, publisher: National Academy of Sciences Section: Research Articles.

Fischer, E. V., et al., 2014: Atmospheric peroxyacetyl nitrate (PAN): a global budget and source attribution. *Atmospheric Chemistry and Physics*, **14 (5)**, 2679–2698, doi: 10.5194/acp-14-2679-2014, URL https://www.atmos-chem-phys.net/14/2679/2014/.

Fountoukis, C. and A. Nenes, 2007: ISORROPIA II: a computationally efficient thermodynamic equilibrium model for K+–Ca2+–Mg2+–NH+4 –Na+–SO24–NO3 –Cl–H2O aerosols. *Atmos. Chem. Phys.*, 21.

Garcia-Hurtado, E., et al., 2014: Atmospheric PM and volatile organic compounds released from Mediterranean shrubland wildfires. *Atmospheric Environment*, **89**, 85–92, doi: 10.1016/j.atmosenv.2014.02.016, URL http://www.sciencedirect.com/science/article/pii/S1352231014001125.

Garofalo, L. A., M. A. Pothier, E. J. T. Levin, T. Campos, S. M. Kreidenweis, and D. K. Farmer, 2019: Emission and Evolution of Submicron Organic Aerosol in Smoke from Wildfires in the Western United States. *ACS Earth and Space Chemistry*, **3 (7)**, 1237–1247, doi: 10.1021/acsearthspacechem.9b00125, URL https://doi.org/10.1021/acsearthspacechem.9b00125.

Gilman, J. B., et al., 2015: Biomass burning emissions and potential air quality impacts of volatile organic compounds and other trace gases from fuels common in the US. *Atmospheric Chemistry and Physics*, **15 (24)**, 13 915–13 938, doi: https://doi.org/10.5194/acp-15-13915-2015, URL https://www.atmos-chem-phys.net/15/13915/2015/acp-15-13915-2015.html.

Glarborg, P., J. A. Miller, B. Ruscic, and S. J. Klippenstein, 2018: Modeling nitrogen chemistry in combustion. *Progress in Energy and Combustion Science*, **67**, 31–68, doi: 10.1016/j.pecs.2018.01.002, URL http://www.sciencedirect.com/science/article/pii/S0360128517301600.

Goode, J. G., R. J. Yokelson, R. A. Susott, and D. E. Ward, 1999: Trace gas emissions from laboratory biomass fires measured by open-path Fourier transform infrared spectroscopy: Fires in grass and surface fuels. *Journal of Geophysical Research: Atmospheres*, **104 (D17)**, 21 237–21 245, doi: 10.1029/1999JD900360, URL https://agupubs.onlinelibrary.wiley.com/doi/abs/10.1029/1999JD900360.

Goode, J. G., R. J. Yokelson, D. E. Ward, R. A. Susott, R. E. Babbitt, M. A. Davies, and W. M. Hao, 2000: Measurements of excess O3, CO2, CO, CH4, C2H4, C2H2, HCN, NO, NH3, HCOOH, CH3COOH, HCHO, and CH3OH in 1997 Alaskan biomass burning plumes by airborne Fourier transform infrared spectroscopy (AFTIR). *Journal of Geophysical Research: Atmospheres*, **105 (D17)**, 22 147–22 166, doi: 10.1029/2000JD900287, URL https://agupubs.onlinelibrary.wiley.com/doi/abs/10.1029/2000JD900287.

Griffith, S. M., et al., 2016: Measurements of hydroxyl and hydroperoxy radicals during CalNex-LA: Model comparisons and radical budgets. *Journal of Geophysical Research: Atmospheres*, **121 (8)**, 4211–4232, doi: 10.1002/2015JD024358, URL http://agupubs.onlinelibrary.wiley.com/doi/abs/10.1002/2015JD024358, _eprint: https://onlinelibrary.wiley.com/doi/pdf/10.1002/2015JD024358.

Grosjean, D., E. L. Williams, and E. Grosjean, 1993: A biogenic precursor of peroxypropionyl nitrate: atmospheric oxidation of cis-3-hexen-1-ol. *Environmental Science & Technology*, **27 (5)**, 979–981, doi: 10.1021/es00042a023, URL https://doi.org/10.1021/es00042a023, publisher: American Chemical Society.

Guo, H., R. Otjes, P. Schlag, A. Kiendler-Scharr, A. Nenes, and R. J. Weber, 2018: Effectiveness of ammonia reduction on control of fine particle nitrate. *Atmospheric Chemistry and Physics*, **18 (16)**, 12 241–12 256, doi: https://doi.org/10.5194/acp-18-12241-2018, URL https://www.atmos-chem-phys.net/18/12241/2018/.

Hansson, K.-M., J. Samuelsson, C. Tullin, and L.-E. Åmand, 2004: Formation of HNCO, HCN, and NH3 from the pyrolysis of bark and nitrogen-containing model compounds. *Combustion and Flame*, **137 (3)**, 265–277, doi: 10.1016/j.combustflame.2004.01.005, URL http://www.sciencedirect.com/science/article/pii/S0010218004000276.

Harris, G., T. E. Kleindienst, and J. N. Pitts, 1981: RATE CONSTANTS FOR THE REACTION OF OH RADICALS WlTH CH$N, C2H&N AND CH2=CH-CN IN THE TEMPERATURE RANGE 298424 K. *CHEMICAL PHYSICS LETTERS*, **80 (3)**, 5.

Hatch, L. E., W. Luo, J. F. Pankow, R. J. Yokelson, C. E. Stockwell, and K. C. Barsanti, 2015: Identification and quantification of gaseous organic compounds emitted from biomass burning using two-dimensional gas chromatography–time-of-flight mass spectrometry. *Atmospheric Chemistry and Physics*, **15 (4)**, 1865–1899, doi: 10.5194/acp-15-1865-2015, URL https://www.atmos-chem-phys.net/15/1865/2015/.

Hecobian, A., et al., 2011: Comparison of chemical characteristics of 495 biomass burning plumes intercepted by the NASA DC-8 aircraft during the ARCTAS/CARB-2008 field campaign. *Atmospheric Chemistry and Physics*, **11 (24)**, 13 325–13 337, doi: https://doi.org/10.5194/acp-11-13325-2011, URL https://www.atmos-chem-phys.net/11/13325/2011/, publisher: Copernicus GmbH.

Hobbs, P. V., et al., 2003: Evolution of gases and particles from a savanna fire in South Africa: EVOLUTION OF GASES AND PARTICLES. *Journal of Geophysical Research: Atmospheres*, **108 (D13)**, n/a–n/a, doi: 10.1029/2002JD002352, URL http://doi.wiley.com/10.1029/2002JD002352.

Holloway, T., H. Levy, and P. Kasibhatla, 2000: Global distribution of carbon monoxide. *Journal of Geophysical Research: Atmospheres*, **105 (D10)**, 12 123–12 147, doi: 10.1029/1999JD901173, URL http://agupubs.onlinelibrary.wiley.com/doi/abs/10.1029/1999JD901173, _eprint: https://onlinelibrary.wiley.com/doi/pdf/10.1029/1999JD901173.

Hoover, K. and L. A. Hanson, 2019: National Interagency Fire Center Wildfire Statistics. 2, doi: https://fas.org/sgp/crs/misc/IF10244.pdf, URL https://fas.org/sgp/crs/misc/IF10244.pdf.

Hornbrook, R. S., J. H. Crawford, G. D. Edwards, O. Goyea, R. L. Mauldin III, J. S. Olson, and C. A. Cantrell, 2011: Measurements of tropospheric HO $_2$ and RO $_2$ by oxygen dilution modulation and chemical ionization mass spectrometry. *Atmospheric Measurement Techniques*, **4 (4)**, 735–756, doi: 10.5194/amt-4-735-2011, URL https://www.atmos-meas-tech.net/4/735/2011/.

Horowitz, A., R. Meller, and G. K. Moortgat, 2001: The UV–VIS absorption cross sections of the -dicarbonyl compounds: pyruvic acid, biacetyl and glyoxal. *Journal of Photochemistry and Photobiology A: Chemistry*, **146 (1)**, 19–27, doi: 10.1016/S1010-6030(01)00601-3, URL http://www.sciencedirect.com/science/article/pii/S1010603001006013.

Jaffe, D. A., W. Hafner, D. Chand, A. Westerling, and D. Spracklen, 2008: Interannual Variations in PM2.5 due to Wildfires in the Western United States. *Environmental Science & Technology*, **42 (8)**, 2812–2818, doi: 10.1021/es702755v, URL https://doi.org/10.1021/es702755v.

Jaffe, D. A. and N. L. Wigder, 2012: Ozone production from wildfires: A critical review. *Atmospheric Environment*, **51**, 1–10, doi: 10.1016/j.atmosenv.2011.11.063, URL http://www.sciencedirect.com/science/article/pii/S1352231011012507.

Jenkin, M. E., S. M. Saunders, and M. J. Pilling, 1997: The tropospheric degradation of volatile organic compounds: a protocol for mechanism development. *Atmospheric Environment*, **31 (1)**, 81–104, doi: 10.1016/S1352-2310(96)00105-7, URL http://www.sciencedirect.com/science/article/pii/S1352231096001057.

Jenkin, M. E., S. M. Saunders, V. Wagner, and M. J. Pilling, 2003: Protocol for the development of the Master Chemical Mechanism, MCM v3 (Part B): tropospheric degradation of aromatic volatile organic compounds. *Atmospheric Chemistry and Physics*, **3 (1)**, 181–193, doi: https://doi.org/10.5194/acp-3-181-2003, URL https://www.atmos-chem-phys.net/3/181/2003/, publisher: Copernicus GmbH.

Kanakidou, M., S. Myriokefalitakis, and K. Tsigaridis, 2018: Aerosols in atmospheric chemistry and biogeochemical cycles of nutrients. *Environmental Research Letters*, **13 (6)**, 063 004, doi: 10.1088/1748-9326/aabcdb, URL https://doi.org/10.1088%2F1748-9326%2Faabcdb, publisher: IOP Publishing.

Kanakidou, M., et al., 2005: Organic aerosol and global climate modelling: a review. *Atmospheric Chemistry and Physics*, **5 (4)**, 1053–1123, doi: https://doi.org/10.5194/acp-5-1053-2005, URL https://www.atmos-chem-phys.net/5/1053/2005/, publisher: Copernicus GmbH.

Karlsson, P. E., et al., 2013: Biomass burning in eastern Europe during spring 2006 caused high deposition of ammonium in northern Fennoscandia. *Environmental Pollution*, **176**, 71–79, doi: 10.1016/j.envpol.2012.12.006, URL http://www.sciencedirect.com/science/article/pii/S0269749112005313.

Keywood, M., et al., 2013: Fire in the Air: Biomass Burning Impacts in a Changing Climate. *Critical Reviews in Environmental Science and Technology*, **43 (1)**, 40–83, doi: 10.1080/10643389.2011.604248, URL https://doi.org/10.1080/10643389.2011.604248, publisher: Taylor & Francis _eprint: https://doi.org/10.1080/10643389.2011.604248.

Kirchner, F., A. Mayer–Figge, F. Zabel, and K. H. Becker, 1999: Thermal stability of Peroxynitrates. *International Journal of Chemical Kinetics*, **31 (2)**, 127–144, doi: 10.1002/(SICI)1097-4601(1999)31:2<127::AID-KIN6>3.0.CO;2-L, URL http://onlinelibrary.wiley.com/doi/abs/10.1002/%28SICI%291097-4601%281999%2931%3A2%3C127%3A%3AAID-KIN6%3E3.0.CO%3B2-L, _eprint: https://onlinelibrary.wiley.com/doi/pdf/10.1002/%28SICI%291097-4601%281999%2931%3A2%3C127%3A%3AAID-KIN6%3E3.0.CO%3B2-L.

Kleinman, L. I., et al., 2008: The time evolution of aerosol composition over the Mexico City plateau. *Atmos. Chem. Phys.*, 17.

Klotz, B., F. Graedler, S. Sørensen, I. Barnes, and K.-H. Becker, 2001: A kinetic study of the atmospheric photolysis of -dicarbonyls. *International Journal of Chemical Kinetics*, **33 (1)**, 9–20, doi: 10.1002/1097-4601(20010101)33:1<9::AID-KIN2>3.0.CO;2-V, URL http://onlinelibrary.wiley.com/doi/abs/10.1002/1097-4601%2820010101%2933%3A1%3C9%3A%3AAID-KIN2%3E3.0.CO%3B2-V, _eprint: https://onlinelibrary.wiley.com/doi/pdf/10.1002/1097-4601%2820010101%2933%3A1%3C9%3A%3AAID-KIN2%3E3.0.CO%3B2-V.

Kolden, C. A., 2019: We're Not Doing Enough Prescribed Fire in the Western United States to Mitigate Wildfire Risk. *Fire*, **2 (2)**, 30, doi: 10.3390/fire2020030, URL https://www.mdpi.com/2571-6255/2/2/30.

Koss, A. R., et al., 2018: Non-methane organic gas emissions from biomass burning: identification, quantification, and emission factors from PTR-ToF during the FIREX 2016 laboratory experiment.

Atmospheric Chemistry and Physics, **18 (5)**, 3299–3319, doi: https://doi.org/10.5194/acp-18-3299-2018, URL https://www.atmos-chem-phys.net/18/3299/2018/.

Kuhlbusch, T. A., J. M. Lobert, P. J. Crutzen, and P. Warneck, 1991: Molecular nitrogen emissions from denitrification during biomass burning. *Nature*, **351 (6322)**, 135–137, doi: 10.1038/351135a0, URL https://www.nature.com/articles/351135a0.

LaFranchi, B. W., et al., 2009: Closing the peroxy acetyl nitrate budget: observations of acyl peroxy nitrates (PAN, PPN, and MPAN) during BEARPEX 2007. *Atmospheric Chemistry and Physics*, **9 (19)**, 7623–7641, doi: 10.5194/acp-9-7623-2009, URL https://www.atmos-chem-phys.net/9/7623/2009/.

Laskin, A., J. Laskin, and S. A. Nizkorodov, 2015: Chemistry of Atmospheric Brown Carbon. *Chemical Reviews*, **115 (10)**, 4335–4382, doi: 10.1021/cr5006167, URL https://doi.org/10.1021/cr5006167, publisher: American Chemical Society.

Lebegue, B., et al., 2016: Comparison of nitrous oxide (N_2O) analyzers for high-precision measurements of atmospheric mole fractions. *Atmospheric Measurement Techniques*, **9 (3)**, 1221–1238, doi: https://doi.org/10.5194/amt-9-1221-2016, URL https://www.atmos-meas-tech.net/9/1221/2016/.

Lee, B. H., F. D. Lopez-Hilfiker, C. Mohr, T. Kurtén, D. R. Worsnop, and J. A. Thornton, 2014: An Iodide-Adduct High-Resolution Time-of-Flight Chemical-Ionization Mass Spectrometer: Application to Atmospheric Inorganic and Organic Compounds. *Environmental Science & Technology*, **48 (11)**, 6309–6317, doi: 10.1021/es500362a, URL https://pubs.acs.org/doi/10.1021/es500362a.

Lee, B. H., et al., 2016: Highly functionalized organic nitrates in the southeast United States: Contribution to secondary organic aerosol and reactive nitrogen budgets. *Proceedings of*

the National Academy of Sciences, **113 (6)**, 1516–1521, doi: 10.1073/pnas.1508108113, URL https://www.pnas.org/content/113/6/1516, publisher: National Academy of Sciences Section: Physical Sciences.

Lee, B. H., et al., 2018: Flight Deployment of a High-Resolution Time-of-Flight Chemical Ionization Mass Spectrometer: Observations of Reactive Halogen and Nitrogen Oxide Species. *Journal of Geophysical Research: Atmospheres*, **123 (14)**, 7670–7686, doi: 10.1029/2017JD028082, URL https://agupubs.onlinelibrary.wiley.com/doi/abs/10.1029/2017JD028082.

Levin, E. J. T., et al., 2010: Biomass burning smoke aerosol properties measured during Fire Laboratory at Missoula Experiments (FLAME). *Journal of Geophysical Research: Atmospheres*, **115 (D18)**, doi: 10.1029/2009JD013601, URL https://agupubs.onlinelibrary.wiley.com/doi/abs/10.1029/2009JD013601, _eprint: https://agupubs.onlinelibrary.wiley.com/doi/pdf/10.1029/2009JD013601.

Li, J., M. Pósfai, P. V. Hobbs, and P. R. Buseck, 2003: Individual aerosol particles from biomass burning in southern Africa: 2, Compositions and aging of inorganic particles. *Journal of Geophysical Research: Atmospheres*, doi: 10.1029/2002JD002310@10.1002/(ISSN)2169-8996.SAF1, URL https://agupubs.onlinelibrary.wiley.com/doi/abs/10.1029/2002JD002310%4010.1002/%28ISSN%292169-8996.SAF1.

Li, Q., D. J. Jacob, I. Bey, R. M. Yantosca, Y. Zhao, Y. Kondo, and J. Notholt, 2000: Atmospheric hydrogen cyanide (HCN): Biomass burning source, ocean sink? *Geophysical Research Letters*, **27 (3)**, 357–360, doi: 10.1029/1999GL010935, URL https://agupubs.onlinelibrary.wiley.com/doi/abs/10.1029/1999GL010935, _eprint: https://agupubs.onlinelibrary.wiley.com/doi/pdf/10.1029/1999GL010935.

Lin, P., P. K. Aiona, Y. Li, M. Shiraiwa, J. Laskin, S. A. Nizkorodov, and A. Laskin, 2016: Molecular Characterization of Brown Carbon in Biomass Burning Aerosol Particles. *Environmental Science & Technology*, **50 (21)**, 11 815–11 824, doi: 10.1021/acs.est.6b03024, URL https://doi.org/10.1021/acs.est.6b03024.

Liu, X., et al., 2016: Agricultural fires in the southeastern U.S. during SEAC4RS: Emissions of trace gases and particles and evolution of ozone, reactive nitrogen, and organic aerosol. *Journal of Geophysical Research: Atmospheres*, **121 (12)**, 7383–7414, doi: 10.1002/2016JD025040, URL https://agupubs.onlinelibrary.wiley.com/doi/abs/10.1002/2016JD025040.

Liu, X., et al., 2017: Airborne measurements of western U.S. wildfire emissions: Comparison with prescribed burning and air quality implications. *Journal of Geophysical Research: Atmospheres*, **122 (11)**, 6108–6129, doi: 10.1002/2016JD026315, URL https://agupubs.onlinelibrary.wiley.com/doi/abs/10.1002/2016JD026315.

Liu, Y., J. Liggio, R. Staebler, and S.-M. Li, 2015: Reactive uptake of ammonia to secondary organic aerosols: kinetics of organonitrogen formation. *Atmospheric Chemistry and Physics*, **15 (23)**, 13 569–13 584, doi: https://doi.org/10.5194/acp-15-13569-2015, URL https://www.atmos-chem-phys.net/15/13569/2015/, publisher: Copernicus GmbH.

Lobert, J. M., D. H. Scharffe, W. M. Hao, and P. J. Crutzen, 1990: Importance of biomass burning in the atmospheric budgets of nitrogen-containing gases. *Nature*, **346 (6284)**, 552–554, doi: 10.1038/346552a0, URL http://www.nature.com/articles/346552a0.

Lobert, J. M. and J. Warnatz, 1993: Emissions from the combustion process in vegetation. *Fire in the Environment: The Ecological, Atmospheric and Climatic Importance of Vegetation Fires, Crutzen, P. J. and Goldhammer, J. G. (Eds.),*, John Wiley and Sons, New York, NY.

Lutsch, E., E. Dammers, S. Conway, and K. Strong, 2016: Long-range transport of NH3, CO, HCN, and C2H6 from the 2014 Canadian Wildfires. *Geophysical Research Letters*, **43 (15)**, 8286–8297, doi: 10.1002/2016GL070114, URL https://agupubs.onlinelibrary.wiley.com/doi/abs/10.1002/2016GL070114.

Madronich, S., 1987: Photodissociation in the atmosphere: 1. Actinic flux and the effects of ground reflections and clouds. *Journal of Geophysical Research: Atmospheres*, **92 (D8)**, 9740–9752, doi: 10.1029/JD092iD08p09740, URL http://agupubs.onlinelibrary.wiley.com/doi/abs/10.1029/JD092iD08p09740, _eprint: https://onlinelibrary.wiley.com/doi/pdf/10.1029/JD092iD08p09740.

Malm, W. C., et al., 2005: Intercomparison and closure calculations using measurements of aerosol species and optical properties during the Yosemite Aerosol Characterization Study. *Journal of Geophysical Research: Atmospheres*, **110 (D14)**, doi: 10.1029/2004JD005494, URL https://agupubs.onlinelibrary.wiley.com/doi/abs/10.1029/2004JD005494, _eprint: https://agupubs.onlinelibrary.wiley.com/doi/pdf/10.1029/2004JD005494.

Marlon, J. R., et al., 2012: Long-term perspective on wildfires in the western USA. *Proceedings of the National Academy of Sciences*, **109 (9)**, E535–E543, doi: 10.1073/pnas.1112839109, URL https://www.pnas.org/content/109/9/E535, publisher: National Academy of Sciences Section: PNAS Plus.

McAllister, S., 2019: The Role of Fuel Bed Geometry and Wind on the Burning Rate of Porous Fuels. *Frontiers in Mechanical Engineering*, **5**, doi: 10.3389/fmech.2019.00011, URL https://www.frontiersin.org/articles/10.3389/fmech.2019.00011/full, publisher: Frontiers.

McClure, C. D. and D. A. Jaffe, 2018: US particulate matter air quality improves except in wildfire-prone areas. *Proceedings of the National Academy of Sciences*, **115 (31)**, 7901–7906,

doi: 10.1073/pnas.1804353115, URL https://www.pnas.org/content/115/31/7901.

McManus, J. B., P. L. Kebabian, and M. S. Zahniser, 1995: Astigmatic mirror multipass absorption cells for long-path-length spectroscopy. *Applied Optics*, **34 (18)**, 3336–3348, doi: 10.1364/AO.34.003336, URL https://www.osapublishing.org/ao/abstract.cfm?uri=ao-34-18-3336.

McManus, J. B., J. H. Shorter, D. D. Nelson, and M. S. Zahniser, 2007: Compact Quantum Cascade Laser Instrument for Rapid, High Sensitivity Measurements of Trace Gases in Air. *2007 IEEE SENSORS*, 1341–1344, doi: 10.1109/ICSENS.2007.4388659, iSSN: 1930-0395.

McManus, J. B., M. S. Zahniser, D. D. N. Jr, J. H. Shorter, S. C. Herndon, E. C. Wood, and R. Wehr, 2010: Application of quantum cascade lasers to high-precision atmospheric trace gas measurements. *Optical Engineering*, **49 (11)**, 111 124, doi: 10.1117/1.3498782, URL https://www.spiedigitallibrary.org/journals/Optical-Engineering/volume-49/issue-11/111124/Application-of-quantum-cascade-lasers-to-high-precision-atmospheric-trace/10.1117/1.3498782.short.

McMeeking, G. R., et al., 2009: Emissions of trace gases and aerosols during the open combustion of biomass in the laboratory. *Journal of Geophysical Research: Atmospheres*, **114 (D19)**, doi: 10.1029/2009JD011836, URL https://agupubs.onlinelibrary.wiley.com/doi/abs/10.1029/2009JD011836.

Moree-Testa, P. and Y. Saint-Jalm, 1981: Determination of -dicarbonyl compounds in cigarette smoke. *Journal of Chromatography A*, **217**, 197–208, doi: 10.1016/S0021-9673(00)88074-7, URL http://www.sciencedirect.com/science/article/pii/S0021967300880747.

Myhre, G., et al., 2013: Anthropogenic and Natural Radiative Forcing. Tech. rep., Cambridge University Press, 82 pp., Cambirdge, United Kingdon and New York, NY, USA.

Müller, M., et al., 2016: In situ measurements and modeling of reactive trace gases in a small biomass burning plume. *Atmospheric Chemistry and Physics*, **16 (6)**, 3813–3824, doi: https://doi.org/10.5194/acp-16-3813-2016, URL https://www.atmos-chem-phys.net/16/3813/2016/, publisher: Copernicus GmbH.

NASA, 2015: Chemical Kinetics and Photochemical Data for Use in Atmospheric Studies Evaluation Number 18. Jet Propulsion Laboratory, URL http://jpldataeval.jpl.nasa.gov.

Obermeyer, G., S. M. Aschmann, R. Atkinson, and J. Arey, 2009: Carbonyl atmospheric reaction products of aromatic hydrocarbons in ambient air. *Atmospheric Environment*, **43 (24)**, 3736–3744, doi: 10.1016/j.atmosenv.2009.04.015, URL http://www.sciencedirect.com/science/article/pii/S1352231009003306.

Ottmar, R. D., D. V. Sandberg, C. L. Riccardi, and S. J. Prichard, 2007: An overview of the Fuel Characteristic Classification System — Quantifying, classifying, and creating fuelbeds for resource planningThis article is one of a selection of papers published in the Special Forum on the Fuel Characteristic Classification System. *Canadian Journal of Forest Research*, **37 (12)**, 2383–2393, doi: 10.1139/X07-077, URL http://www.nrcresearchpress.com/doi/10.1139/X07-077.

O'Dell, K., B. Ford, E. V. Fischer, and J. R. Pierce, 2019: Contribution of Wildland-Fire Smoke to US PM2.5 and Its Influence on Recent Trends. *Environmental Science & Technology*, **53 (4)**, 1797–1804, doi: 10.1021/acs.est.8b05430, URL https://doi.org/10.1021/acs.est.8b05430.

Palm, B. B., X. Liu, J. L. Jimenez, and J. A. Thornton, 2019: Performance of a new coaxial ion–molecule reaction region for low-pressure chemical ionization mass spectrometry with reduced instrument wall interactions. *Atmospheric Measurement Techniques*, **12 (11)**, 5829–5844, doi: https://doi.org/10.5194/amt-12-5829-2019, URL https://www.atmos-meas-tech.net/12/5829/2019/.

Park, R. J., D. J. Jacob, M. Chin, and R. V. Martin, 2003: Sources of carbonaceous aerosols over the United States and implications for natural visibility. *Journal of Geophysical Research: Atmospheres*, **108 (D12)**, doi: 10.1029/2002JD003190, URL https://agupubs.onlinelibrary.wiley.com/doi/abs/10.1029/2002JD003190.

Park, R. J., D. J. Jacob, and J. A. Logan, 2007: Fire and biofuel contributions to annual mean aerosol mass concentrations in the United States. *Atmospheric Environment*, **41 (35)**, 7389–7400, doi: 10.1016/j.atmosenv.2007.05.061, URL http://www.sciencedirect.com/science/article/pii/S1352231007005122.

Paulot, F., D. J. Jacob, R. W. Pinder, J. O. Bash, K. Travis, and D. K. Henze, 2014: Ammonia emissions in the United States, European Union, and China derived by high-resolution inversion of ammonium wet deposition data: Interpretation with a new agricultural emissions inventory (MASAGE_nh3). *Journal of Geophysical Research: Atmospheres*, **119 (7)**, 4343–4364, doi: 10.1002/2013JD021130, URL http://agupubs.onlinelibrary.wiley.com/doi/abs/10.1002/2013JD021130, _eprint: https://onlinelibrary.wiley.com/doi/pdf/10.1002/2013JD021130.

Paulot, F., et al., 2017: Gas-aerosol partitioning of ammonia in biomass burning plumes: Implications for the interpretation of spaceborne observations of ammonia and the radiative forcing of ammonium nitrate. *Geophysical Research Letters*, **44 (15)**, 8084–8093, doi: 10.1002/2017GL074215, URL https://agupubs.onlinelibrary.wiley.com/doi/abs/10.1002/2017GL074215.

Peng, Q., et al., 2020: HONO Emissions from Western U.S. Wildfires Provide Dominant Radical Source in Fresh Wildfire Smoke. *Environmental Science & Technology*, **54 (10)**, 5954–5963, doi: 10.1021/acs.est.0c00126, URL https://doi.org/10.1021/acs.est.0c00126, publisher: American Chemical Society.

Penner, J. E., R. E. Dickinson, and C. A. O'Neill, 1992: Effects of Aerosol from Biomass Burning on the Global Radiation Budget. *Science*, **256 (5062)**, 1432–1434, doi: 10.1126/science.256.5062.1432, URL https://science.sciencemag.org/content/256/5062/1432, publisher: American Association for the Advancement of Science Section: Reports.

Plum, C. N., E. Sanhueza, R. Atkinson, W. P. L. Carter, and J. N. Pitts, 1983: Hydroxyl radical rate constants and photolysis rates of .alpha.-dicarbonyls. *Environmental Science & Technology*, **17 (8)**, 479–484, doi: 10.1021/es00114a008, URL https://doi.org/10.1021/es00114a008, publisher: American Chemical Society.

Pollack, I. B., J. Lindaas, J. R. Roscioli, M. Agnese, W. Permar, L. Hu, and E. V. Fischer, 2019: Evaluation of ambient ammonia measurements from a research aircraft using a closed-path QC-TILDAS operated with active continuous passivation. *Atmospheric Measurement Techniques*, **12 (7)**, 3717–3742, doi: https://doi.org/10.5194/amt-12-3717-2019, URL https://www.atmos-meas-tech.net/12/3717/2019/.

Prenni, A. J., et al., 2014: Gas-phase reactive nitrogen near Grand Teton National Park: Impacts of transport, anthropogenic emissions, and biomass burning. *Atmospheric Environment*, **89**, 749–756, doi: 10.1016/j.atmosenv.2014.03.017, URL http://www.sciencedirect.com/science/article/pii/S1352231014001885.

Rajakumar, B., T. Gierczak, J. E. Flad, A. R. Ravishankara, and J. B. Burkholder, 2008: The CH3CO quantum yield in the 248nm photolysis of acetone, methyl ethyl ketone, and biacetyl. *Journal of Photochemistry and Photobiology A: Chemistry*, **199 (2)**, 336–344, doi: 10.1016/j.jphotochem.2008.06.015,

URL http://www.sciencedirect.com/science/article/pii/S1010603008002918.

Ren, Q. and C. Zhao, 2012: NOx and N2O Precursors from Biomass Pyrolysis: Nitrogen Transformation from Amino Acid. *Environmental Science & Technology*, **46 (7)**, 4236–4240, doi: 10.1021/es204142e, URL https://doi.org/10.1021/es204142e.

Ren, Q. and C. Zhao, 2013a: NOx and N2O Precursors from Biomass Pyrolysis: Role of Cellulose, Hemicellulose and Lignin. *Environmental Science & Technology*, **47 (15)**, 8955–8961, doi: 10.1021/es4017574, URL https://doi.org/10.1021/es4017574.

Ren, Q. and C. Zhao, 2013b: NOx and N2O precursors (NH3 and HCN) from biomass pyrolysis: interaction between amino acid and mineral matter. *Applied Energy*, **112**, 170–174, doi: 10.1016/j.apenergy.2013.05.061, URL http://www.sciencedirect.com/science/article/pii/S0306261913004741.

R'Honi, Y., L. Clarisse, C. Clerbaux, D. Hurtmans, V. Duflot, S. Turquety, Y. Ngadi, and P.-F. Coheur, 2013: Exceptional emissions of NH_3 and HCOOH in the 2010 Russian wildfires. *Atmospheric Chemistry and Physics*, **13 (8)**, 4171–4181, doi: https://doi.org/10.5194/acp-13-4171-2013, URL https://www.atmos-chem-phys.net/13/4171/2013/.

Ridley, B. A. and F. E. Grahek, 1990: A Small, Low Flow, High Sensitivity Reaction Vessel for NO Chemiluminescence Detectors. *Journal of Atmospheric and Oceanic Technology*, **7 (2)**, 307–311, doi: 10.1175/1520-0426(1990)007<0307:ASLFHS>2.0.CO;2, URL https://journals.ametsoc.org/doi/abs/10.1175/1520-0426%281990%29007%3C0307%3AASLFHS%3E2.0.CO%3B2.

Ridley, B. A., F. E. Grahek, and J. G. Walega, 1992: A Small High-Sensitivity, Medium-Response Ozone Detector Suitable for Measurements from Light Aircraft. *Journal of Atmospheric and Oceanic Technology*, **9 (2)**, 142–148, doi: 10.1175/1520-0426(1992)009<0142:ASHSMR>2.0.CO;2, URL

https://journals.ametsoc.org/doi/abs/10.1175/1520-0426%281992%29009%3C0142%3AASHSMR%3E2.0.CO%3B2.

Roberts, J. M., 2007: PAN and Related Compounds. *Volatile Organic Compounds in the Atmosphere*, John Wiley & Sons, Ltd, 221–268, doi: 10.1002/9780470988657.ch6, URL http://onlinelibrary.wiley.com/doi/abs/10.1002/9780470988657.ch6, section: 6 _eprint: https://onlinelibrary.wiley.com/doi/pdf/10.1002/9780470988657.ch6.

Roberts, J. M., et al., 2001: Application of a sequential reaction model to PANs and aldehyde measurements in two urban areas. *Geophysical Research Letters*, **28 (24)**, 4583–4586, doi: 10.1029/2001GL013507, URL https://agupubs.onlinelibrary.wiley.com/doi/abs/10.1029/2001GL013507, _eprint: https://agupubs.onlinelibrary.wiley.com/doi/pdf/10.1029/2001GL013507.

Roberts, J. M., et al., 2010: Measurement of HONO, HNCO, and other inorganic acids by negative-ion proton-transfer chemical-ionization mass spectrometry (NI-PT-CIMS): application to biomass burning emissions. *Atmospheric Measurement Techniques*, **3 (4)**, 981–990, doi: https://doi.org/10.5194/amt-3-981-2010, URL https://www.atmos-meas-tech.net/3/981/2010/.

Roberts, J. M., et al., 2020: The nitrogen budget of laboratory-simulated western U.S. wildfires during the FIREX 2016 FireLab study. preprint, Gases/Laboratory Studies/Troposphere/Chemistry (chemical composition and reactions). doi: 10.5194/acp-2020-66, URL https://www.atmos-chem-phys-discuss.net/acp-2020-66/.

Russo, R. S., Y. Zhou, M. L. White, H. Mao, R. Talbot, and B. C. Sive, 2010: Multi-year (2004–2008) record of nonmethane hydrocarbons and halocarbons in New England: seasonal variations and regional sources. *Atmospheric Chemistry and Physics*, **10 (10)**, 4909–4929, doi: https://doi.org/10.5194/acp-10-4909-2010, URL https://www.atmos-chem-phys.net/10/4909/2010/.

Salvador, C. M., T. T. Ho, C. C. K. Chou, M. J. Chen, W. R. Huang, and S. H. Huang, 2016: Characterization of the organic matter in submicron urban aerosols using a Thermo-Desorption Proton-Transfer-Reaction Time-of-Flight Mass Spectrometer (TD-PTR-TOF-MS). *Atmospheric Environment*, **140**, 565–575, doi: 10.1016/j.atmosenv.2016.06.029, URL http://www.sciencedirect.com/science/article/pii/S1352231016304629.

Sander, S. P., et al., 2006: Chemical kinetics and photochemical data for use in atmospheric studies : evaluation number 15. Technical Report, Pasadena, CA : Jet Propulsion Laboratory, California Institute of Technology. URL https://trs.jpl.nasa.gov/handle/2014/39839, accepted: 2006-10-19T22:11:53Z Journal Abbreviation: Evaluation number 15.

Santín, C., S. H. Doerr, C. M. Preston, and G. González-Rodríguez, 2015: Pyrogenic organic matter production from wildfires: a missing sink in the global carbon cycle. *Global Change Biology*, **21 (4)**, 1621–1633, doi: 10.1111/gcb.12800, URL https://onlinelibrary.wiley.com/doi/abs/10.1111/gcb.12800.

Scharko, N. K., et al., 2019: Gas-phase pyrolysis products emitted by prescribed fires in pine forests with a shrub understory in the southeastern United States. *Atmospheric Chemistry and Physics*, **19 (15)**, 9681–9698, doi: https://doi.org/10.5194/acp-19-9681-2019, URL https://www.atmos-chem-phys.net/19/9681/2019/.

Schauer, J. J., M. J. Kleeman, G. R. Cass, and B. R. T. Simoneit, 2001: Measurement of Emissions from Air Pollution Sources. 3. C1C29 Organic Compounds from Fireplace Combustion of Wood. *Environmental Science & Technology*, **35 (9)**, 1716–1728, doi: 10.1021/es001331e, URL https://doi.org/10.1021/es001331e, publisher: American Chemical Society.

Schoennagel, T., et al., 2017: Adapt to more wildfire in western North American forests as climate changes. *Proceedings of the National Academy of Sciences*, **114 (18)**, 4582–4590, doi: 10.1073/pnas.1617464114, URL https://www.pnas.org/content/114/18/4582.

Schultz, C. A. and C. Moseley, 2019: Collaborations and capacities to transform fire management. *Science*, **366 (6461)**, 38–40, doi: 10.1126/science.aay3727, URL https://science.sciencemag.org/content/366/6461/38.

Sedlacek III, A. J., P. R. Buseck, K. Adachi, T. B. Onasch, S. R. Springston, and L. Kleinman, 2018: Formation and evolution of tar balls from northwestern US wildfires. *Atmospheric Chemistry and Physics*, **18 (15)**, 11 289–11 301, doi: https://doi.org/10.5194/acp-18-11289-2018, URL https://www.atmos-chem-phys.net/18/11289/2018/, publisher: Copernicus GmbH.

Seiler, W. and P. J. Crutzen, 1980: Estimates of gross and net fluxes of carbon between the biosphere and the atmosphere from biomass burning. *Climatic Change*, **2 (3)**, 207–247, doi: 10.1007/BF00137988, URL https://doi.org/10.1007/BF00137988.

Seinfeld, J. H. and S. N. Pandis, 2016: Atmospheric Chemistry and Physics: From Air Pollution to Climate Change, 3rd Edition | Wiley. URL https://www.wiley.com/en-us/Atmospheric+Chemistry+and+Physics%3A+From+Air+Pollution+to+Climate+Change%2C+3rd+Edition-p-9781118947401, library Catalog: www.wiley.com.

Sekimoto, K., S.-M. Li, B. Yuan, A. Koss, M. Coggon, C. Warneke, and J. de Gouw, 2017: Calculation of the sensitivity of proton-transfer-reaction mass spectrometry (PTR-MS) for organic trace gases using molecular properties. *International Journal of Mass Spectrometry*, **421**, 71–94, doi: 10.1016/j.ijms.2017.04.006, URL http://www.sciencedirect.com/science/article/pii/S1387380616302494.

Sekimoto, K., et al., 2018: High- and low-temperature pyrolysis profiles describe volatile organic compound emissions from western US wildfire fuels. *Atmospheric Chemistry and Physics*, **18 (13)**, 9263–9281, doi: 10.5194/acp-18-9263-2018, URL https://www.atmos-chem-phys.net/18/9263/2018/.

Selimovic, V., R. J. Yokelson, C. Warneke, J. M. Roberts, J. d. Gouw, J. Reardon, and D. W. T. Griffith, 2018: Aerosol optical properties and trace gas emissions by PAX and OP-FTIR for laboratory-simulated western US wildfires during FIREX. *Atmospheric Chemistry and Physics*, **18 (4)**, 2929–2948, doi: https://doi.org/10.5194/acp-18-2929-2018, URL https://www.atmos-chem-phys.net/18/2929/2018/.

Shetter, R. E. and M. Müller, 1999: Photolysis frequency measurements using actinic flux spectroradiometry during the PEM-Tropics mission: Instrumentation description and some results. *Journal of Geophysical Research: Atmospheres*, **104 (D5)**, 5647–5661, doi: 10.1029/98JD01381, URL http://agupubs.onlinelibrary.wiley.com/doi/abs/10.1029/98JD01381, _eprint: https://onlinelibrary.wiley.com/doi/pdf/10.1029/98JD01381.

Sillman, S. and J. J. West, 2009: Reactive nitrogen in Mexico City and its relation to ozone-precursor sensitivity: results from photochemical models. *Atmos. Chem. Phys.*, 13.

Singh, H. B., 1987: Reactive nitrogen in the troposphere. *Environmental Science & Technology*, **21 (4)**, 320–327, doi: 10.1021/es00158a001, URL https://doi.org/10.1021/es00158a001, publisher: American Chemical Society.

Singh, H. B. and P. L. Hanst, 1981: Peroxyacetyl nitrate (PAN) in the unpolluted atmosphere: An important reservoir for nitrogen oxides. *Geophysical Research Letters*, **8 (8)**, 941–944, doi: 10.1029/GL008i008p00941, URL http://agupubs.onlinelibrary.wiley.com/doi/abs/10.1029/GL008i008p00941, _eprint: https://onlinelibrary.wiley.com/doi/pdf/10.1029/GL008i008p00941.

Singh, H. B., et al., 1992: Atmospheric measurements of peroxyacetyl nitrate and other organic nitrates at high latitudes: Possible sources and sinks. *Journal of Geophysical Research: Atmospheres*, **97 (D15)**, 16 511–16 522, doi: 10.1029/91JD00889, URL https://agupubs.onlinelibrary.wiley.com/doi/abs/10.1029/91JD00889, _eprint: https://agupubs.onlinelibrary.wiley.com/doi/pdf/10.1029/91JD00889.

Slusher, D. L., L. G. Huey, D. J. Tanner, F. M. Flocke, and J. M. Roberts, 2004: A thermal dissociation–chemical ionization mass spectrometry (TD-CIMS) technique for the simultaneous measurement of peroxyacyl nitrates and dinitrogen pentoxide. *Journal of Geophysical Research: Atmospheres*, **109 (D19)**, doi: 10.1029/2004JD004670, URL https://agupubs.onlinelibrary.wiley.com/doi/abs/10.1029/2004JD004670.

Sokolik, I. N., A. J. Soja, P. J. DeMott, and D. Winker, 2019: Progress and Challenges in Quantifying Wildfire Smoke Emissions, Their Properties, Transport, and Atmospheric Impacts. *Journal of Geophysical Research: Atmospheres*, **124 (23)**, 13 005–13 025, doi: 10.1029/2018JD029878, URL http://agupubs.onlinelibrary.wiley.com/doi/abs/10.1029/2018JD029878, _eprint: https://onlinelibrary.wiley.com/doi/pdf/10.1029/2018JD029878.

Song, C. H., Y. Ma, D. Orsini, Y. P. Kim, and R. J. Weber, 2005: An Investigation into the Ionic Chemical Composition and Mixing State of Biomass Burning Particles Recorded During TRACE-P P3B Flight#10. *Journal of Atmospheric Chemistry*, **51 (1)**, 43–64, doi: 10.1007/s10874-005-5727-9, URL https://doi.org/10.1007/s10874-005-5727-9.

Stelson, A. W. and J. H. Seinfeld, 1982: Relative humidity and temperature dependence of the ammonium nitrate dissociation constant. *Atmospheric Environment (1967)*, **16 (5)**, 983–992, doi: 10.1016/0004-6981(82)90184-6, URL http://www.sciencedirect.com/science/article/pii/0004698182901846.

Stockwell, C. E., P. R. Veres, J. Williams, and R. J. Yokelson, 2015: Characterization of biomass burning emissions from cooking fires, peat, crop residue, and other fuels with high-resolution proton-transfer-reaction time-of-flight mass spectrometry. *Atmospheric Chemistry and Physics*, **15 (2)**, 845–865, doi: https://doi.org/10.5194/acp-15-845-2015, URL https://www.atmos-chem-phys.net/15/845/2015/.

Stockwell, C. E., et al., 2014: Trace gas emissions from combustion of peat, crop residue, domestic biofuels, grasses, and other fuels: configuration and Fourier transform infrared (FTIR) component of the fourth Fire Lab at Missoula Experiment (FLAME-4). *Atmospheric Chemistry and Physics*, **14 (18)**, 9727–9754, doi: https://doi.org/10.5194/acp-14-9727-2014, URL https://www.atmos-chem-phys.net/14/9727/2014/acp-14-9727-2014.html.

Stönner, C., B. Derstroff, T. Klüpfel, J. N. Crowley, and J. Williams, 2017: Glyoxal measurement with a proton transfer reaction time of flight mass spectrometer (PTR-TOF-MS): characterization and calibration. *Journal of Mass Spectrometry*, **52 (1)**, 30–35, doi: 10.1002/jms.3893, URL http://onlinelibrary.wiley.com/doi/abs/10.1002/jms.3893, _eprint: https://onlinelibrary.wiley.com/doi/pdf/10.1002/jms.3893.

Sullivan, A. P., et al., 2019: Biomass Burning Markers and Residential Burning in the WINTER Aircraft Campaign. *Journal of Geophysical Research: Atmospheres*, **124 (3)**, 1846–1861, doi: 10.1029/2017JD028153, URL https://agupubs.onlinelibrary.wiley.com/doi/abs/10.1029/2017JD028153.

Talbot, R. W., A. S. Vijgen, and R. C. Harriss, 1992: Soluble species in the Arctic summer troposphere: Acidic gases, aerosols, and precipitation. *Journal of Geophysical Research: Atmospheres*, **97 (D15)**, 16 531–16 543, doi: 10.1029/91JD00118, URL https://agupubs.onlinelibrary.wiley.com/doi/abs/10.1029/91JD00118, _eprint: https://agupubs.onlinelibrary.wiley.com/doi/pdf/10.1029/91JD00118.

Talukdar, R. K., J. B. Burkholder, A.-M. Schmoltner, J. M. Roberts, R. R. Wilson, and A. R. Ravishankara, 1995: Investigation of the loss processes for peroxyacetyl nitrate in the atmosphere: UV photolysis and reaction with OH. *Journal of Geophysical Research: Atmospheres*, **100 (D7)**, 14 163–14 173, doi: 10.1029/95JD00545, URL http://agupubs.onlinelibrary.wiley.com/doi/abs/10.1029/95JD00545, _eprint: https://onlinelibrary.wiley.com/doi/pdf/10.1029/95JD00545.

Tapia, A., F. Villanueva, M. S. Salgado, B. Cabañas, E. Martínez, and P. Martín, 2011: Atmospheric degradation of 3-methylfuran: kinetic and products study. *Atmospheric Chemistry and Physics*, **11 (7)**, 3227–3241, doi: 10.5194/acp-11-3227-2011, URL https://www.atmos-chem-phys.net/11/3227/2011/.

Trentmann, J., R. J. Yokelson, P. V. Hobbs, T. Winterrath, T. J. Christian, M. O. Andreae, and S. A. Mason, 2005: An analysis of the chemical processes in the smoke plume from a savanna fire. *Journal of Geophysical Research: Atmospheres*, **110 (D12)**, doi: 10.1029/2004JD005628, URL https://agupubs.onlinelibrary.wiley.com/doi/abs/10.1029/2004JD005628.

Tyndall, G. S., R. A. Cox, C. Granier, R. Lesclaux, G. K. Moortgat, M. J. Pilling, A. R. Ravishankara, and T. J. Wallington, 2001: Atmospheric chemistry of small organic peroxy radicals. *Journal of Geophysical Research: Atmospheres*, **106 (D11)**, 12 157–12 182, doi: 10.1029/2000JD900746, URL http://agupubs.onlinelibrary.wiley.com/doi/abs/10.1029/2000JD900746, _eprint: https://onlinelibrary.wiley.com/doi/pdf/10.1029/2000JD900746.

Updyke, K. M., T. B. Nguyen, and S. A. Nizkorodov, 2012: Formation of brown carbon via reactions of ammonia with secondary organic aerosols from biogenic and anthropogenic precursors. *Atmospheric Environment*, **63**, 22–31, doi: 10.1016/j.atmosenv.2012.09.012, URL https://linkinghub.elsevier.com/retrieve/pii/S1352231012008710.

Urbanski, S., 2014: Wildland fire emissions, carbon, and climate: Emission factors. *Forest Ecology and Management*, **317**, 51–60, doi: 10.1016/j.foreco.2013.05.045, URL http:

//www.sciencedirect.com/science/article/pii/S0378112713003447.

Val Martín, M., R. E. Honrath, R. C. Owen, G. Pfister, P. Fialho, and F. Barata, 2006: Significant enhancements of nitrogen oxides, black carbon, and ozone in the North Atlantic lower free troposphere resulting from North American boreal wildfires. *Journal of Geophysical Research: Atmospheres*, **111 (D23)**, doi: 10.1029/2006JD007530, URL http://agupubs.onlinelibrary.wiley.com/doi/abs/10.1029/2006JD007530, _eprint: https://onlinelibrary.wiley.com/doi/pdf/10.1029/2006JD007530.

Westerling, A. L., 2016: Increasing western US forest wildfire activity: sensitivity to changes in the timing of spring. *Philosophical Transactions of the Royal Society B: Biological Sciences*, **371 (1696)**, 20150 178, doi: 10.1098/rstb.2015.0178, URL https://royalsocietypublishing.org/doi/10.1098/rstb.2015.0178, publisher: Royal Society.

Wexler, A. S. and S. L. Clegg, 2002: Atmospheric aerosol models for systems including the ions H+, NH4+, Na+, SO42, NO3, Cl, Br, and H2O. *Journal of Geophysical Research: Atmospheres*, **107 (D14)**, ACH 14–1–ACH 14–14, doi: 10.1029/2001JD000451, URL http://agupubs.onlinelibrary.wiley.com/doi/abs/10.1029/2001JD000451, _eprint: https://onlinelibrary.wiley.com/doi/pdf/10.1029/2001JD000451.

Whitburn, S., M. V. Damme, L. Clarisse, S. Turquety, C. Clerbaux, and P.-F. Coheur, 2016: Doubling of annual ammonia emissions from the peat fires in Indonesia during the 2015 El Niño. *Geophysical Research Letters*, **43 (20)**, 11,007–11,014, doi: 10.1002/2016GL070620, URL https://agupubs.onlinelibrary.wiley.com/doi/abs/10.1002/2016GL070620, _eprint: https://agupubs.onlinelibrary.wiley.com/doi/pdf/10.1002/2016GL070620.

Whitburn, S., et al., 2015: Ammonia emissions in tropical biomass burning regions: Comparison between satellite-derived emissions and bottom-up fire inventories. *Atmospheric Environment*, **121**, 42–54, doi: 10.1016/j.atmosenv.2015.03.015, URL http://www.sciencedirect.com/science/

article/pii/S1352231015002332.

Williams, A. P., J. T. Abatzoglou, A. Gershunov, J. Guzman-Morales, D. A. Bishop, J. K. Balch, and D. P. Lettenmaier, 2019: Observed Impacts of Anthropogenic Climate Change on Wildfire in California. *Earth's Future*, **7 (8)**, 892–910, doi: 10.1029/2019EF001210, URL https://agupubs.onlinelibrary.wiley.com/doi/abs/10.1029/2019EF001210.

Williams, J., et al., 1997: Regional ozone from biogenic hydrocarbons deduced from airborne measurements of PAN, PPN, and MPAN. *Geophysical Research Letters*, **24 (9)**, 1099–1102, doi: 10.1029/97GL00548, URL http://agupubs.onlinelibrary.wiley.com/doi/abs/10.1029/97GL00548, _eprint: https://onlinelibrary.wiley.com/doi/pdf/10.1029/97GL00548.

Wofsy, S. C., et al., 1992: Atmospheric chemistry in the Arctic and subarctic: Influence of natural fires, industrial emissions, and stratospheric inputs. *Journal of Geophysical Research: Atmospheres*, **97 (D15)**, 16 731–16 746, doi: 10.1029/92JD00622, URL https://agupubs.onlinelibrary.wiley.com/doi/abs/10.1029/92JD00622, _eprint: https://agupubs.onlinelibrary.wiley.com/doi/pdf/10.1029/92JD00622.

Xue, L., et al., 2014: On the use of an explicit chemical mechanism to dissect peroxy acetyl nitrate formation. *Environmental Pollution*, **195**, 39–47, doi: 10.1016/j.envpol.2014.08.005, URL http://www.sciencedirect.com/science/article/pii/S0269749114003443.

Yokelson, R. J., M. O. Andreae, and S. K. Akagi, 2013a: Pitfalls with the use of enhancement ratios or normalized excess mixing ratios measured in plumes to characterize pollution sources and aging. *Atmospheric Measurement Techniques*, **6 (8)**, 2155–2158, doi: https://doi.org/10.5194/amt-6-2155-2013, URL https://www.atmos-meas-tech.net/6/2155/2013/.

Yokelson, R. J., D. W. T. Griffith, and D. E. Ward, 1996: Open-path Fourier transform infrared studies of large-scale laboratory biomass fires. *Journal of Geophysical Research: Atmospheres*, **101 (D15)**, 21 067–21 080, doi: 10.1029/96JD01800, URL https://agupubs.onlinelibrary.wiley.com/doi/abs/10.1029/96JD01800.

Yokelson, R. J., R. Susott, D. E. Ward, J. Reardon, and D. W. T. Griffith, 1997: Emissions from smoldering combustion of biomass measured by open-path Fourier transform infrared spectroscopy. *Journal of Geophysical Research: Atmospheres*, **102 (D15)**, 18 865–18 877, doi: 10.1029/97JD00852, URL https://agupubs.onlinelibrary.wiley.com/doi/abs/10.1029/97JD00852.

Yokelson, R. J., et al., 1999: Emissions of formaldehyde, acetic acid, methanol, and other trace gases from biomass fires in North Carolina measured by airborne Fourier transform infrared spectroscopy. *Journal of Geophysical Research: Atmospheres*, **104 (D23)**, 30 109–30 125, doi: 10.1029/1999JD900817, URL https://agupubs.onlinelibrary.wiley.com/doi/abs/10.1029/1999JD900817.

Yokelson, R. J., et al., 2009: Emissions from biomass burning in the Yucatan. *Atmospheric Chemistry and Physics*, **9 (15)**, 5785–5812, doi: https://doi.org/10.5194/acp-9-5785-2009, URL https://www.atmos-chem-phys.net/9/5785/2009/.

Yokelson, R. J., et al., 2013b: Coupling field and laboratory measurements to estimate the emission factors of identified and unidentified trace gases for prescribed fires. *Atmospheric Chemistry and Physics*, **13 (1)**, 89–116, doi: https://doi.org/10.5194/acp-13-89-2013, URL https://www.atmos-chem-phys.net/13/89/2013/acp-13-89-2013.html.

Yuan, B., A. R. Koss, C. Warneke, M. Coggon, K. Sekimoto, and J. A. de Gouw, 2017: Proton-Transfer-Reaction Mass Spectrometry: Applications in Atmospheric Sciences. *Chemical Reviews*, **117 (21)**, 13 187–13 229, doi: 10.1021/acs.chemrev.7b00325, URL https://pubs.acs.org/doi/10.1021/acs.chemrev.7b00325.

Yuan, J., et al., 2018: PAN–Precursor Relationship and Process Analysis of PAN Variations in the Pearl River Delta Region. *Atmosphere*, **9 (10)**, 372, doi: 10.3390/atmos9100372, URL http://www.mdpi.com/2073-4433/9/10/372.

Zahniser, M. S., et al., 1995: Measurement of trace gas fluxes using tunable diode laser spectroscopy. *Philosophical Transactions of the Royal Society of London. Series A: Physical and Engineering Sciences*, **351 (1696)**, 371–382, doi: 10.1098/rsta.1995.0040, URL https://royalsocietypublishing.org/doi/10.1098/rsta.1995.0040.

Zheng, W., F. M. Flocke, G. S. Tyndall, A. Swanson, J. J. Orlando, J. M. Roberts, L. G. Huey, and D. J. Tanner, 2011: Characterization of a thermal decomposition chemical ionization mass spectrometer for the measurement of peroxy acyl nitrates (PANs) in the atmosphere. *Atmospheric Chemistry and Physics*, **11 (13)**, 6529–6547, doi: https://doi.org/10.5194/acp-11-6529-2011, URL https://www.atmos-chem-phys.net/11/6529/2011/.

Zhou, Y., D. Shively, H. Mao, R. S. Russo, B. Pape, R. N. Mower, R. Talbot, and B. C. Sive, 2010: Air Toxic Emissions from Snowmobiles in Yellowstone National Park. *Environmental Science & Technology*, **44 (1)**, 222–228, doi: 10.1021/es9018578, URL https://doi.org/10.1021/es9018578.

APPENDIX

SUPPLEMENTAL INFORMATION FOR CHAPTERS

A1 SUPPLEMENTAL INFORMATION FOR CHAPTER 3

TABLE A1. Species with missing measurements for each set of emission transects used in the Chapter 3 analysis.

Fire ID	missing measurements
Bear Trap Fire RF09 a	
Bear Trap Fire RF09 b	N_2O
Beaver Creek Fire RF11	
Carr Fire RF02 a	PAN, PPN
Carr Fire RF02 b	N_2O, PAN, PPN, PILS NH_4, PILS NO_3, HONO
Donnell Fire RF07	
Goldstone Fire RF10	N_2O
Kiwah Fire RF06 a	
Kiwah Fire RF06 b	N_2O, PILS NH_4
Monument Fire RF10	N_2O, PILS NH_4
Rabbit Foot Fire RF06	
Rabbit Foot Fire RF10	N_2O
Rabbit Foot Fire RF11	N_2O
Rattlesnake Creek Fire RF01	N_2O, PAN, PPN, NO, NO_2
Red Feather Lakes Rx Fire RF18 a	N_2O, HCN, HNCO, HNO_3, HONO, ΣONs, PILS NH_4, PILS NO_3
Red Feather Lakes Rx Fire RF18 b	N_2O, HCN, HNCO, HNO_3, HONO, ΣONs, PILS NH_4, PILS NO_3
Sharps Fire RF04 a	
Sharps Fire RF04 b	
Silver Creek Fire RF19	N_2O, HCN, HNCO, HNO_3, HONO, ΣONs, PILS NH_4, PILS NO_3
South Sugarloaf Fire RF15 a	CH_3CN, ΣNVOCs
South Sugarloaf Fire RF15 b	CH_3CN, ΣNVOCs
South Sugarloaf Fire RF15 c	CH_3CN, ΣNVOCs
South Sugarloaf Fire RF15 d	CH_3CN, ΣNVOCs
Taylor Creek Fire RF03	
Wigwam Fire RF10	N_2O, PILS NH_4, PILS NO_3

TABLE A2. Fire location and fuel types for all fires used in the Chapter 3 analysis.

Fire ID	Lat, Long	Fuels present
Bear Trap Fire RF09 a - b	39.29312, -109.87434	pinyon, douglas fir, engelmann spruce, bigtooth maple, white fir, ponderosa pine, gambel oak, juniper
Beaver Creek Fire RF11	45.93701, -113.51476	lodgepole pine, whitebark pine, subalpine fir, engelmann spruce
Carr Fire RF02 a - b	40.63087, -122.5196	jeffrey pine, ponderosa pine, live oak, blue oak, black oak, douglas fir, wheatgrass, cheatgrass, chamise, knobcone pine, scrub oak, white fir, red fir
Donnell Fire RF07	38.36457, -119.88161	red fir, douglas fir, ponderosa pine, jeffrey pine, sugar pine, tanoak
Goldstone Fire RF10	45.10841, -113.56241	lodgepole pine, douglas fir, ponderosa pine
Kiwah Fire RF06 a - b	44.85122, -115.24404	douglas fir, ponderosa pine, lodgepole pine, willow, sagebrush, sedge, grassland
Monument Fire RF10	44.99973, -111.82156	whitebark pine, subalpine fir, douglas fir, ponderosa pine, engelmann spruce
Rabbit Foot Fire RF06	44.85753, -114.26653	ponderosa pine, subalpine fir, whitebark pine, douglas fir
Rabbit Foot Fire RF10	44.85753, -114.26653	urban, whitebark pine, subalpine fir, douglas fir, ponderosa pine
Rabbit Foot Fire RF11	44.85753, -114.26653	douglas fir, ponderosa pine, sagebrush, whitebark pine, subalpine fir, quaking aspen, engelmann spruce
Rattlesnake Creek Fire RF01	45.27518, -116.36568	ponderosa pine, wheatgrass, douglas fir

TABLE A2. Fire location and fuel types for all fires used in the Chapter 3 analysis.

Fire ID	Lat, Long	Fuels present
Red Feather Lakes Rx Fire RF18 a - b	40.852, -105.576	ponderosa pine, douglas fir, ceanothus, gambel oak
Sharps Fire RF04 a - b	43.58734, -114.1623	sagebrush
Silver Creek Fire RF19	40.22616, -106.60233	quaking aspen, engelmann spruce, subalpine fir, lodgepole pine, whitebark pine
South Sugarloaf Fire RF15 a - d	41.77587, -115.78555	sagebrush, quaking aspen, subalpine fir, douglas fir, engelmann spruce, lodgepole pine
Taylor Creek Fire RF03	42.46705, -123.68992	douglas fir, jeffrey pine, ponderosa pine, tanoak, black oak, madrone
Wigwam Fire RF10	45.13977, -111.89273	douglas fir, ponderosa pine, lodgepole pine, subalpine fir, whitebark pine, engelmann spruce

TABLE A3. Number of emission transects, sampling period, mean altitude of sampling, and mean estimated physical age of the emission transects shown here for all fires used in the Chapter 3 analysis.

Fire ID	number of transects	Start of sampling (UTC)	End of sampling (UTC)	mean Alt (m)	mean Age (min)
Bear Trap Fire RF09 a	3	2018-08-09 21:22:00	2018-08-09 21:37:43	4532	54
Bear Trap Fire RF09 b	1	2018-08-09 23:00:23	2018-08-09 23:05:15	4555	62
Beaver Creek Fire RF11	1	2018-08-15 21:54:45	2018-08-15 21:56:26	4557	58
Carr Fire RF02 a	2	2018-07-26 21:52:10	2018-07-26 22:00:05	3842	67
Carr Fire RF02 b	1	2018-07-26 22:27:35	2018-07-26 22:30:31	3993	62
Donnell Fire RF07	2	2018-08-07 00:22:51	2018-08-07 00:53:43	4534	79
Goldstone Fire RF10	2	2018-08-13 22:07:21	2018-08-13 22:22:29	4561	38
Kiwah Fire RF06 a	4	2018-08-04 00:59:51	2018-08-04 01:17:27	4015	56
Kiwah Fire RF06 b	1	2018-08-04 01:54:40	2018-08-04 01:57:47	4280	70
Monument Fire RF10	1	2018-08-13 22:50:39	2018-08-13 22:52:53	4548	30
Rabbit Foot Fire RF06	3	2018-08-04 01:31:41	2018-08-04 01:45:35	4279	41
Rabbit Foot Fire RF10	3	2018-08-13 21:42:57	2018-08-13 22:05:01	4562	53
Rabbit Foot Fire RF11	4	2018-08-15 20:42:51	2018-08-15 21:33:03	4395	63
Rattlesnake Creek Fire RF01	2	2018-07-24 19:45:00	2018-07-24 20:06:47	3228	71
Red Feather Lakes Rx Fire RF18 a	4	2018-09-10 20:10:51	2018-09-10 20:24:16	3646	31
Red Feather Lakes Rx Fire RF18 b	3	2018-09-10 22:24:54	2018-09-10 22:36:48	4010	39
Sharps Fire RF04 a	2	2018-07-31 20:39:13	2018-07-31 20:55:27	5116	54
Sharps Fire RF04 b	1	2018-08-01 01:03:33	2018-08-01 01:09:05	5132	79
Silver Creek Fire RF19	2	2018-09-13 21:07:16	2018-09-13 21:19:06	5183	26
South Sugarloaf Fire RF15 a	2	2018-08-26 20:08:32	2018-08-26 20:26:07	4244	48
South Sugarloaf Fire RF15 b	2	2018-08-26 20:35:49	2018-08-26 20:57:47	4563	67
South Sugarloaf Fire RF15 c	1	2018-08-26 22:00:13	2018-08-26 22:06:28	4577	73
South Sugarloaf Fire RF15 d	4	2018-08-27 00:53:15	2018-08-27 01:33:56	4475	48
Taylor Creek Fire RF03	4	2018-07-30 22:47:28	2018-07-30 23:03:00	3345	29
Wigwam Fire RF10	2	2018-08-13 22:48:42	2018-08-13 23:02:10	4547	38

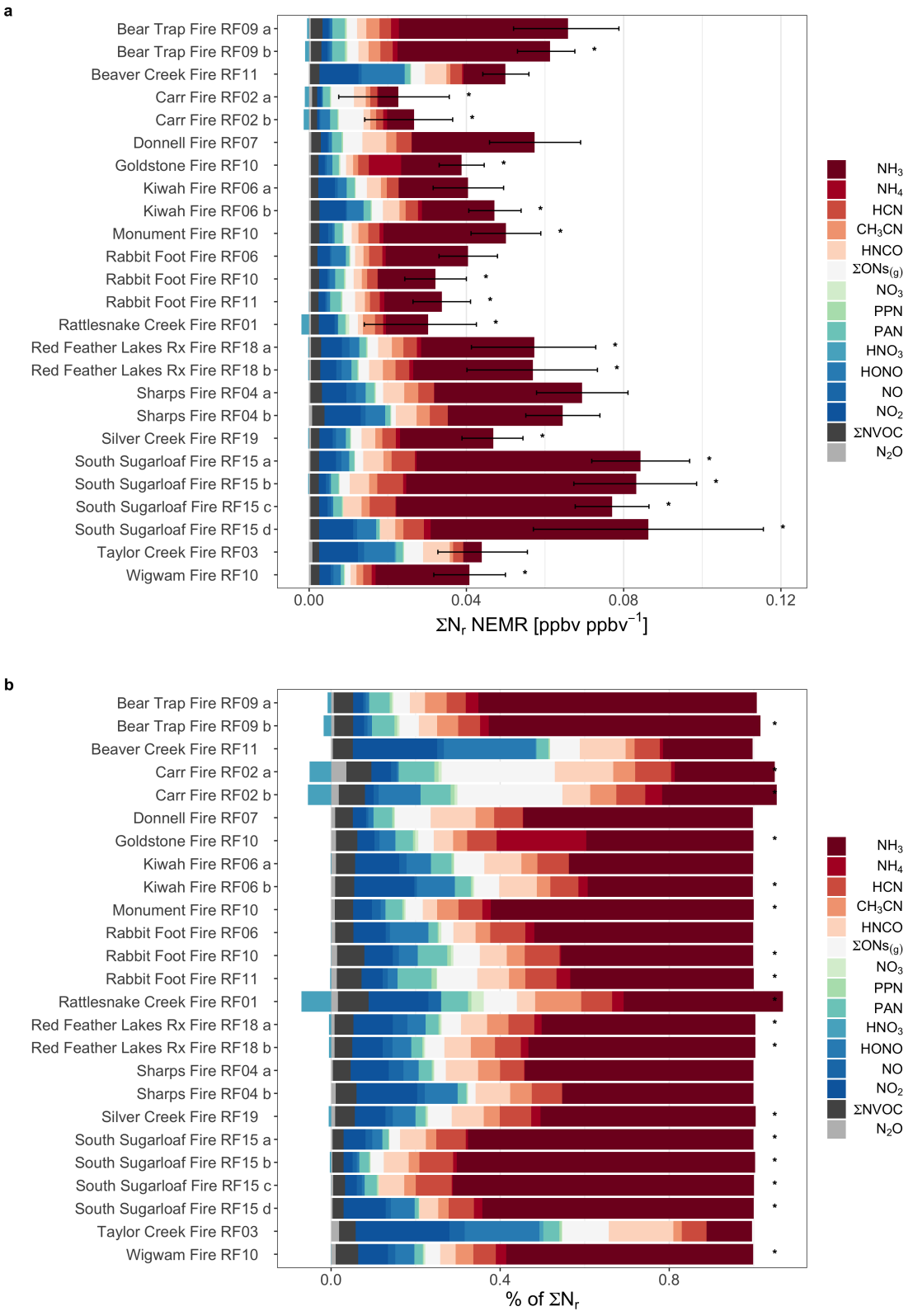
a
Bear Trap Fire RF09 a
Bear Trap Fire RF09 b
Beaver Creek Fire RF11
Carr Fire RF02 a
Carr Fire RF02 b
Donnell Fire RF07
Goldstone Fire RF10
Kiwah Fire RF06 a
Kiwah Fire RF06 b
Monument Fire RF10
Rabbit Foot Fire RF06
Rabbit Foot Fire RF10
Rabbit Foot Fire RF11
Rattlesnake Creek Fire RF01
Red Feather Lakes Rx Fire RF18 a
Red Feather Lakes Rx Fire RF18 b
Sharps Fire RF04 a
Sharps Fire RF04 b
Silver Creek Fire RF19
South Sugarloaf Fire RF15 a
South Sugarloaf Fire RF15 b
South Sugarloaf Fire RF15 c
South Sugarloaf Fire RF15 d
Taylor Creek Fire RF03
Wigwam Fire RF10
0.00
0.04
0.08
0.12
ΣNr NEMR [ppbv ppbv−1]
NH3
NH4
HCN
CH3CN
HNCO
ΣONs(g)
NO3
PPN
PAN
HNO3
HONO
NO
NO2
ΣNVOC
N2O
b
0.0
0.4
0.8
% of ΣNr

FIG. A1. a) Normalized excess mixing ratios (NEMRs) of measured N_r species for emission transects of WE-CAN fires with NO_3 and NH_4 estimates from PILS in place of AMS. Asterisks indicate one or more NEMR estimates are missing and were filled using the mean NEMR for that species across the rest of the emission transects. b) Fractional contribution to total measured reactive nitrogen (ΣN_r) measured in young smoke plumes during WE-CAN. Sums greater than one during some emission transects reflect small negative NEMRs for HNO_3 as described in the text. $p$$NH_4$ and $p$$NO_3$ data are from the AMS.

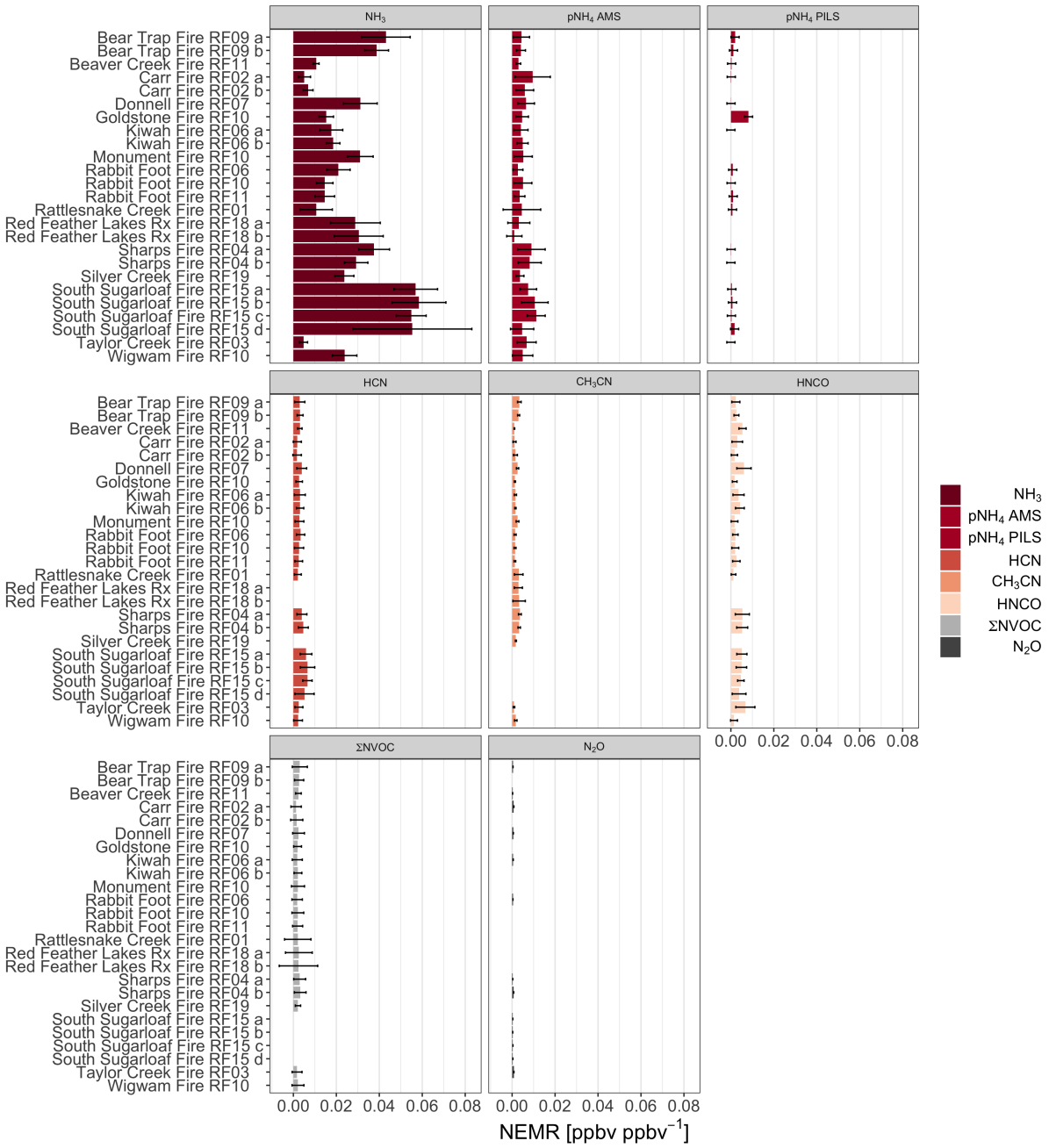

FIG. A2. Normalized excess mixing ratios (NEMRs) of measured reduced N_r species for emission passes of WE-CAN fires, plotted by measured species. While not all NVOCs in ΣNVOCs are reduced, this quantity if also plotted here.

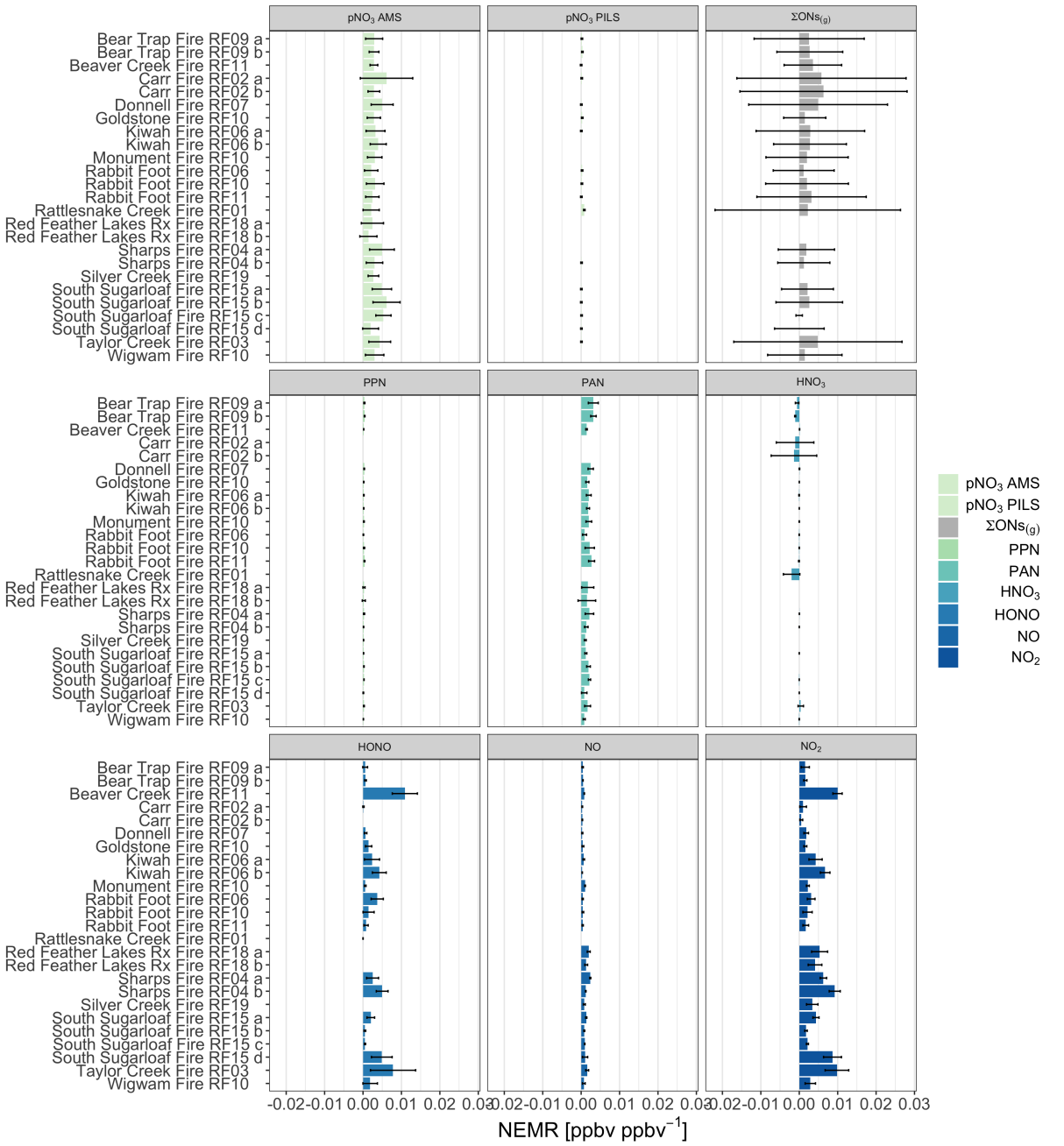

FIG. A3. Normalized excess mixing ratios (NEMRs) of measured oxidized N_r species for emission passes of WE-CAN fires, plotted by measured species.

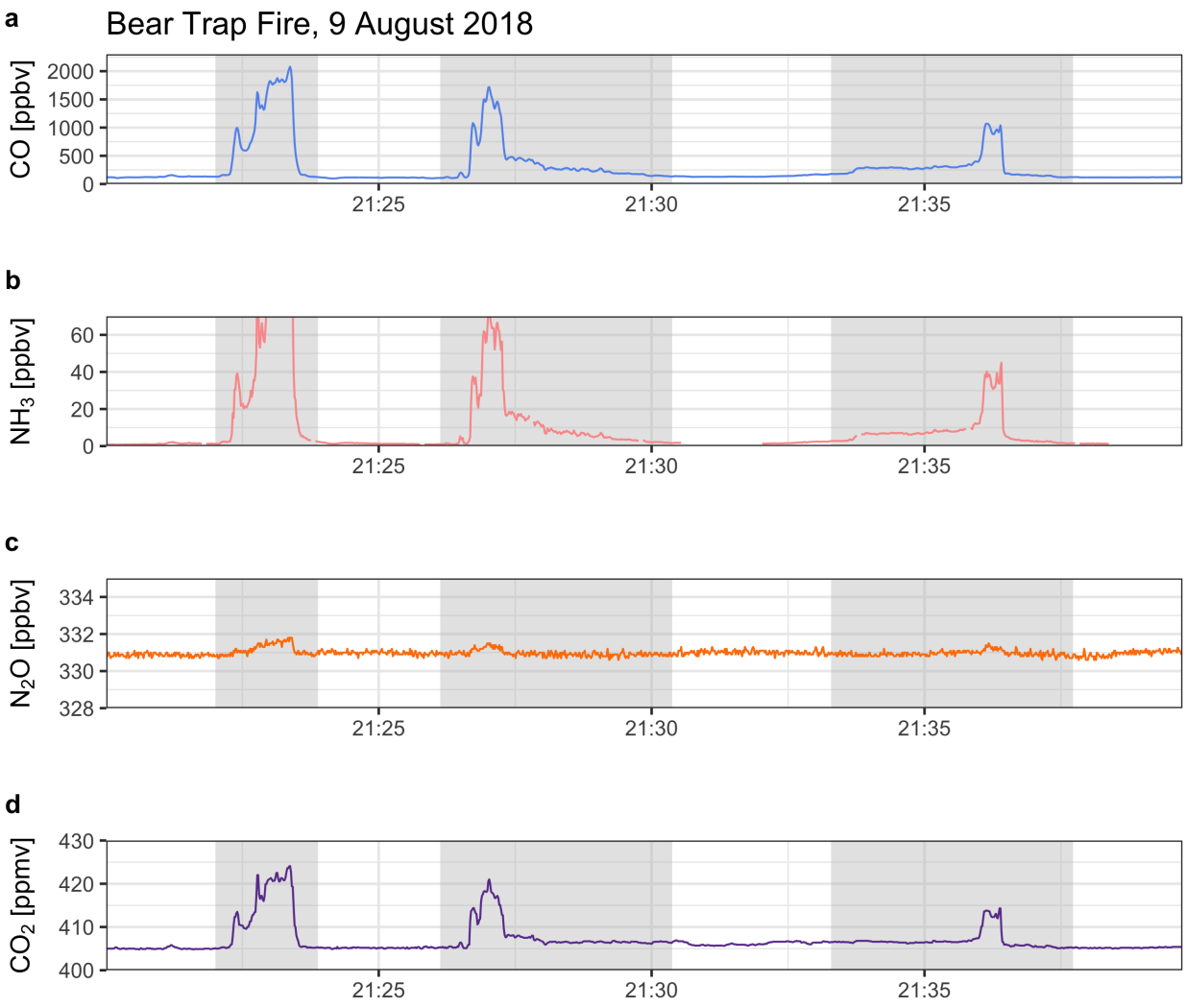

FIG. A4. Timeseries of a) CO, b) NH_3, c) N_2O, and d) CO_2 for the Bear Trap Fire, RF09. Grey shading represents emission transects.

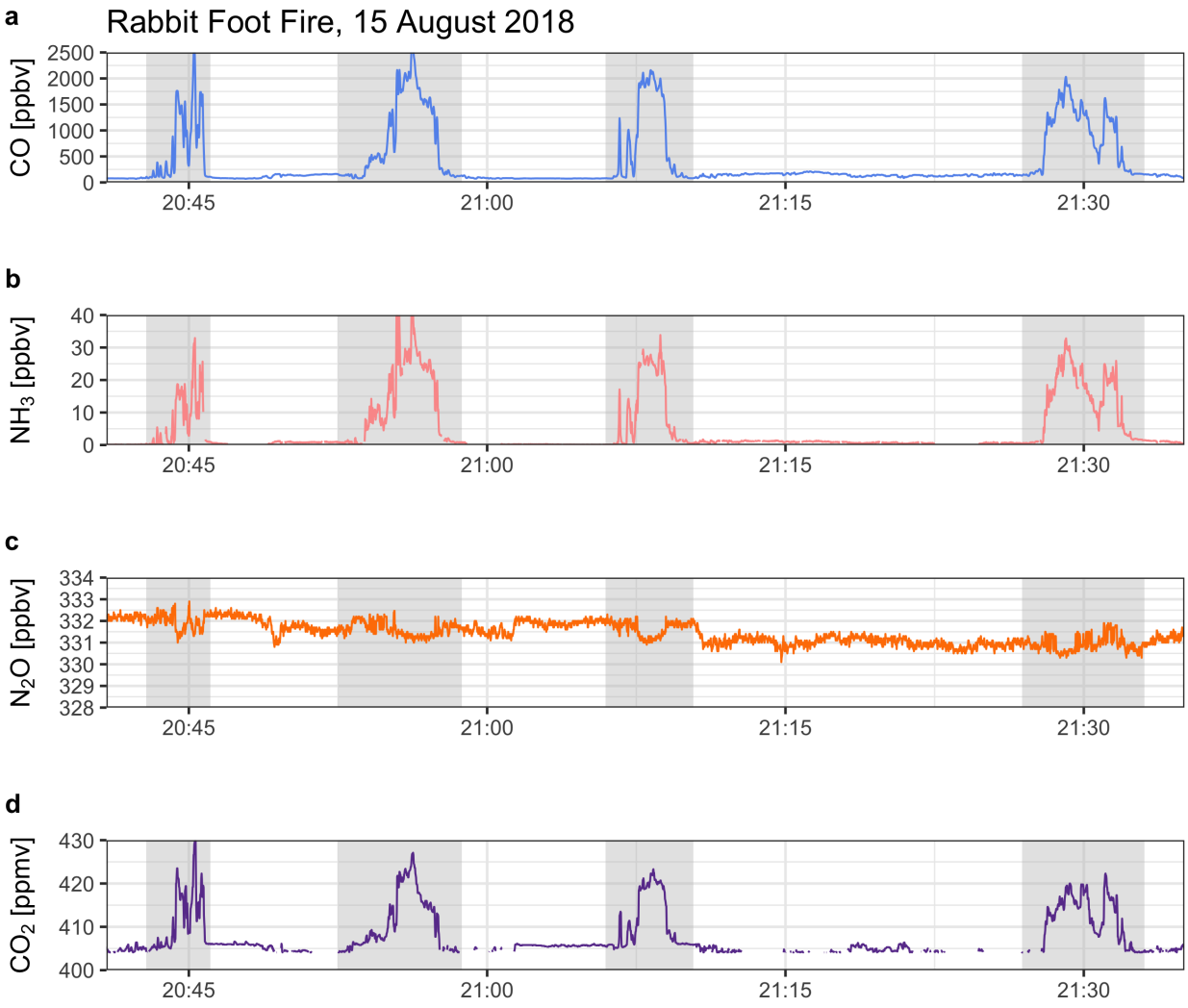

FIG. A5. Timeseries of a) CO, b) NH_3, c) N_2O, and d) CO_2 for the Rabbit Foot Fire, RF11. Grey shading represents emission transects.

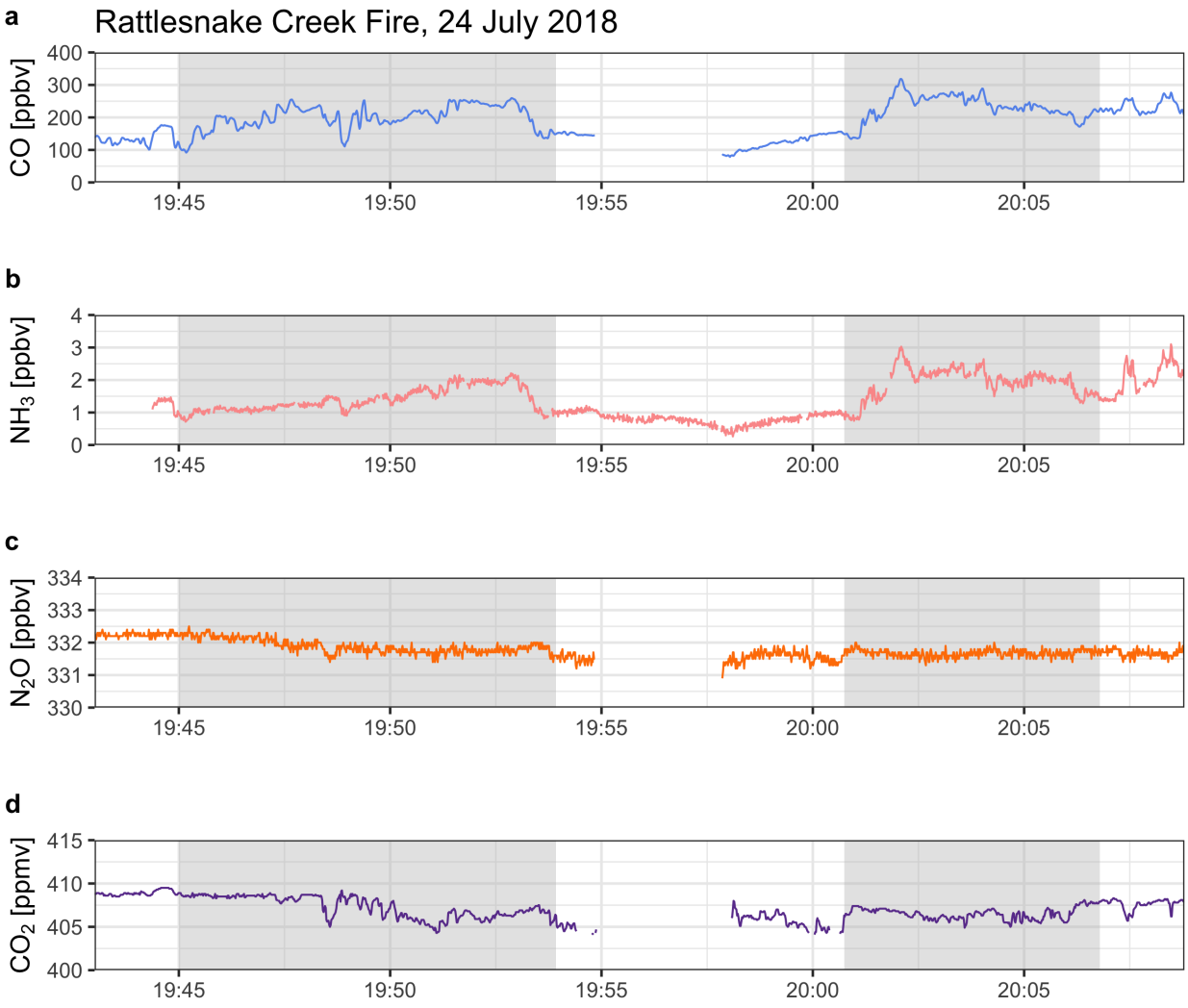

FIG. A6. Timeseries of a) CO, b) NH_3, c) N_2O, and d) CO_2 for the Rattlesnake Creek Fire, RF01. Grey shading represents emission transects.

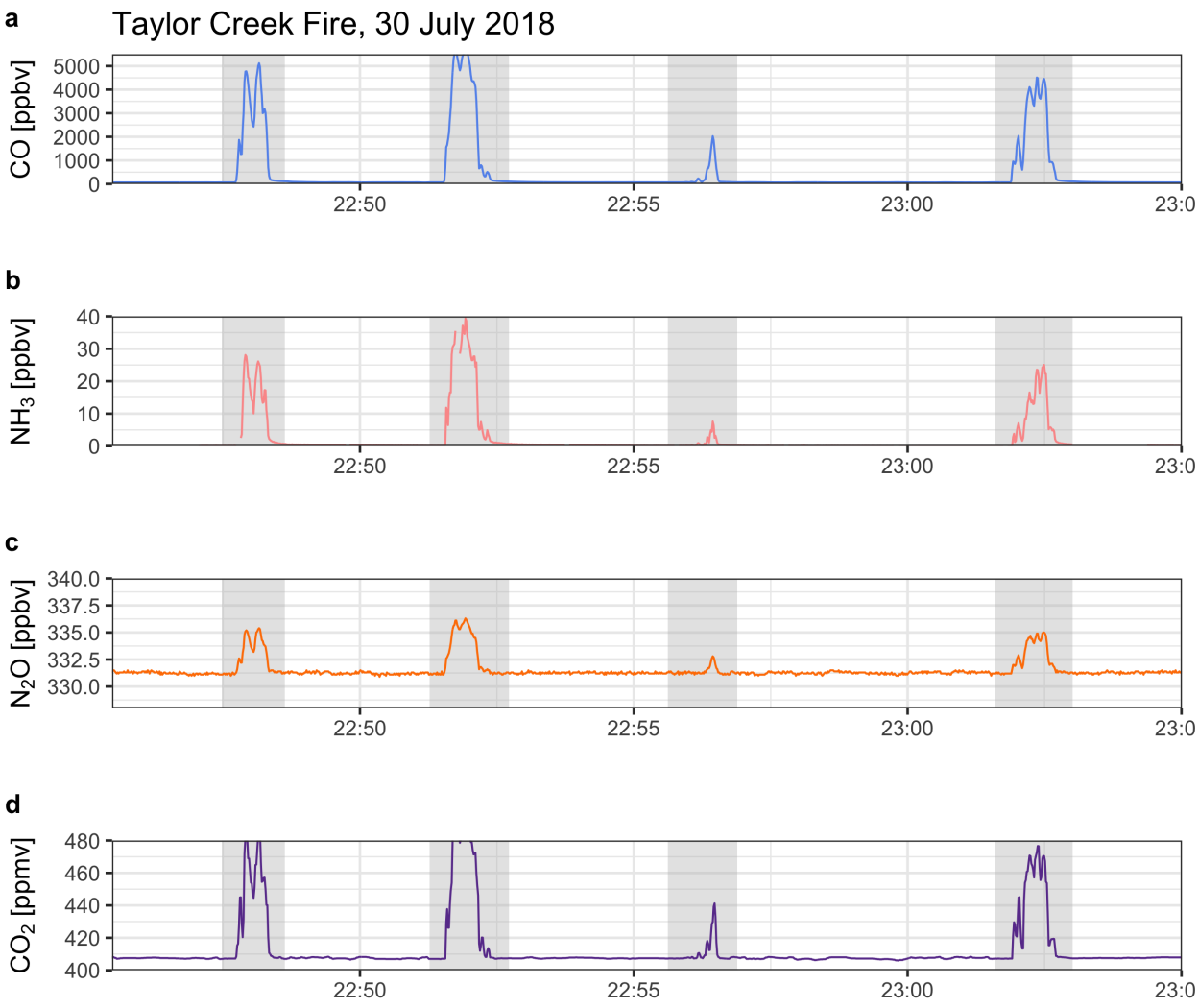

FIG. A7. Timeseries of a) CO, b) NH_3, c) N_2O, and d) CO_2 for the Taylor Creek Fire, RF03. Grey shading represents emission transects.

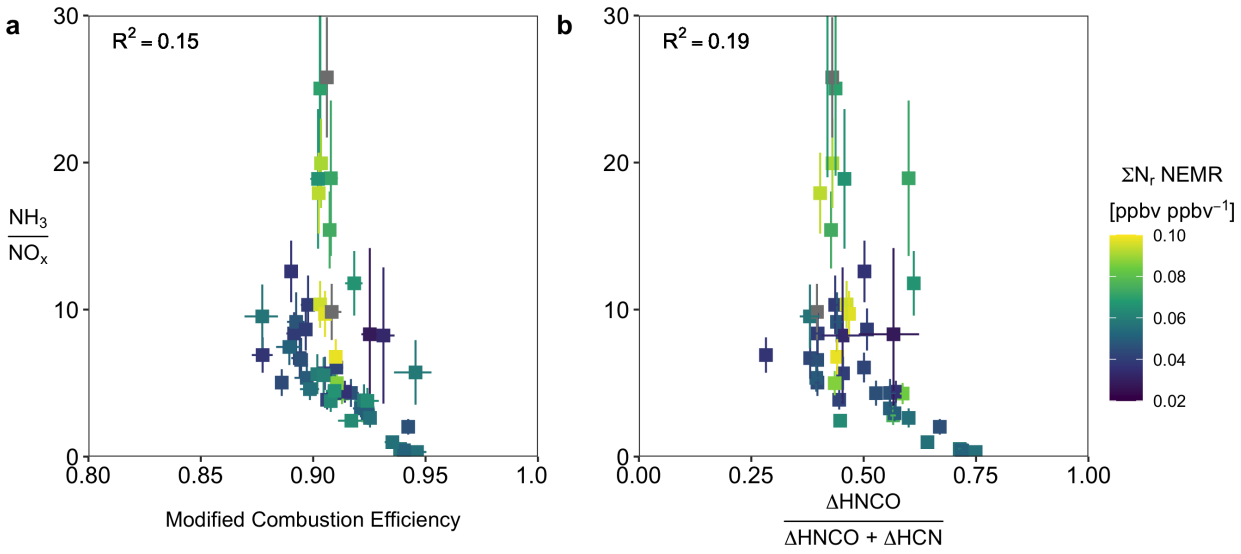

FIG. A8. Relationships between the ratio of NH_3 to NO_x with, a) MCE, and b) the fraction of HCN + HNCO that exists as HNCO.

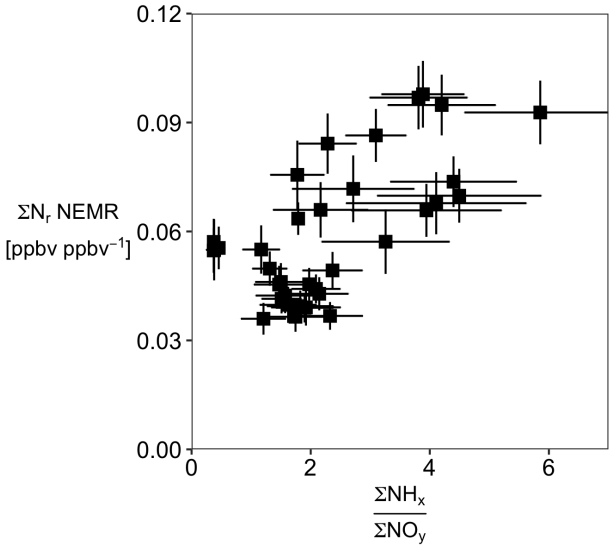

FIG. A9. Relationship between the ratio of $\Sigma NH_x/\Sigma NO_y$ with total measured ΣN_r.

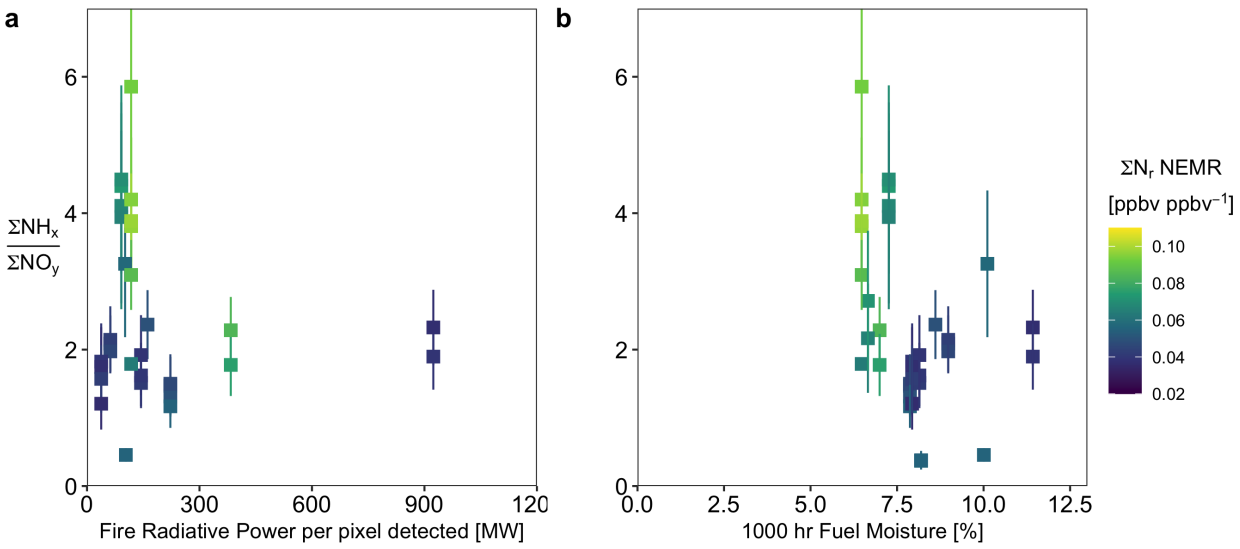

FIG. A10. Relationships between the ratio of ΣNH_x [$= NH_3 + pNH_4$] to ΣNO_y with, a) fire radiative power from MODIS, and b) 1000hr fuel moisture estimates at the time of burn from GRIDMET.

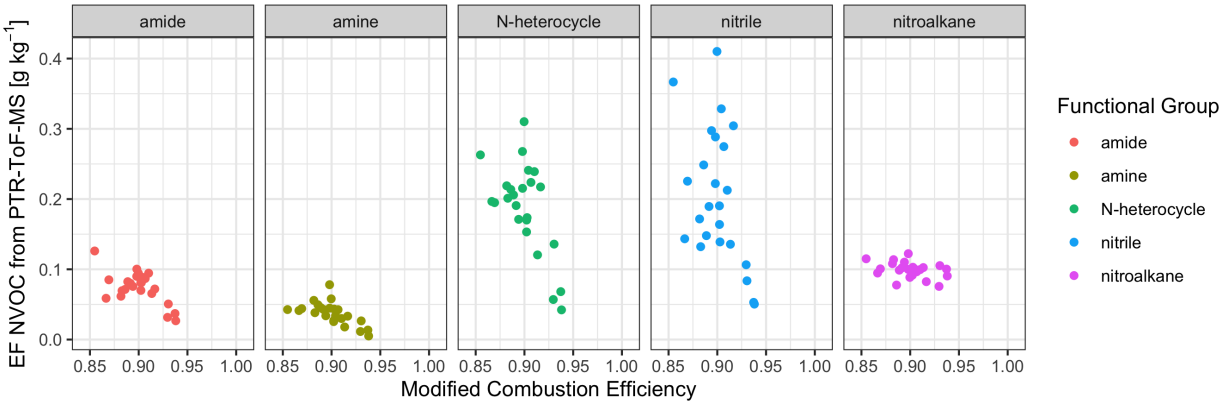

FIG. A11. Comparison of the relationship between NVOC EFs and MCE.

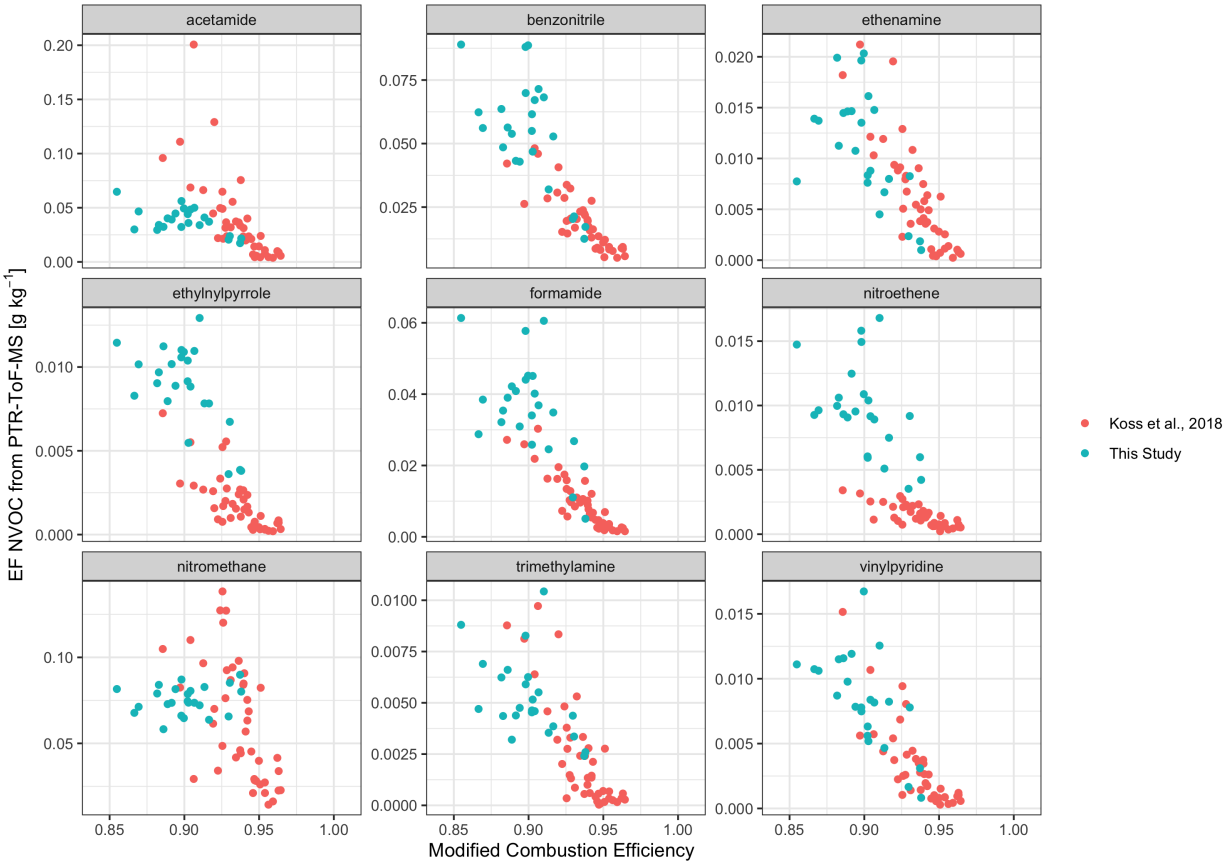

FIG. A12. Comparison of the relationship between NVOC EFs and MCE from this study with those from Koss et al. (2018) for 9 identified species in common.

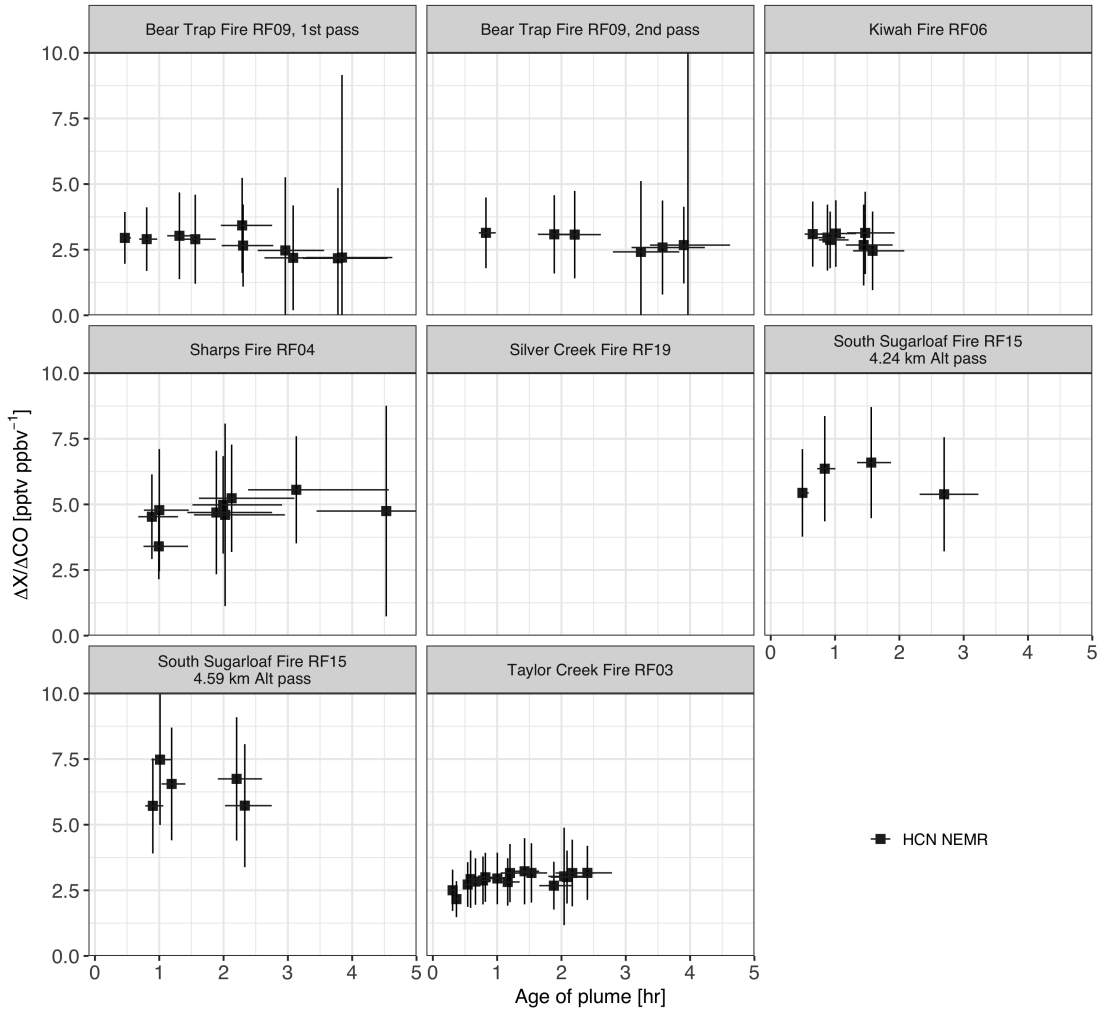

FIG. A13. Evolution of HCN NEMRs with estimated physical plume age. HCN observations were not collected during the Silver Creek Fire sampling. Error bars are the 1σ standard deviations of the calculated NEMRs and the estimated physical age.

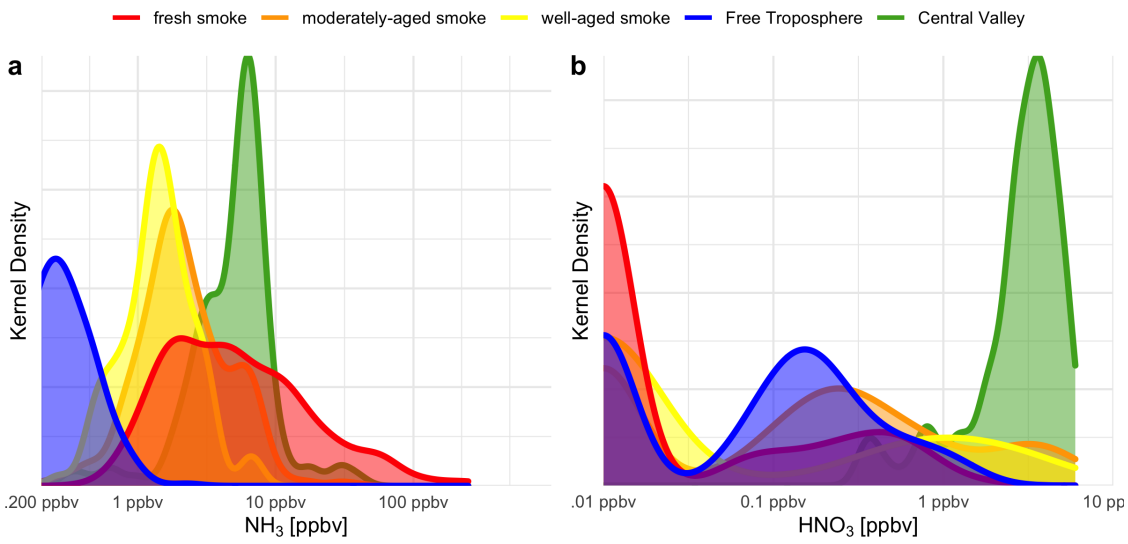

FIG. A14. Kernel density (histogram) plots for subsets of the NH_3 and HNO_3 mixing ratio measurements. All data have been averaged to the TOGA timebase before compilation and plotting. Fresh smoke, medium smoke, and old smoke correspond to data labeled according to the estimated chemical age described in Section 2.2.5. Free troposphere data are measurements identified as not smoke-influenced and >3 km above sea level (asl) in altitude. Central Valley data consist of observations measured below 3 km asl during research flight RF08, 8 August 2018, which included missed approaches in the California Central Valley. These data contain both smoke and anthropogenic emission influence.

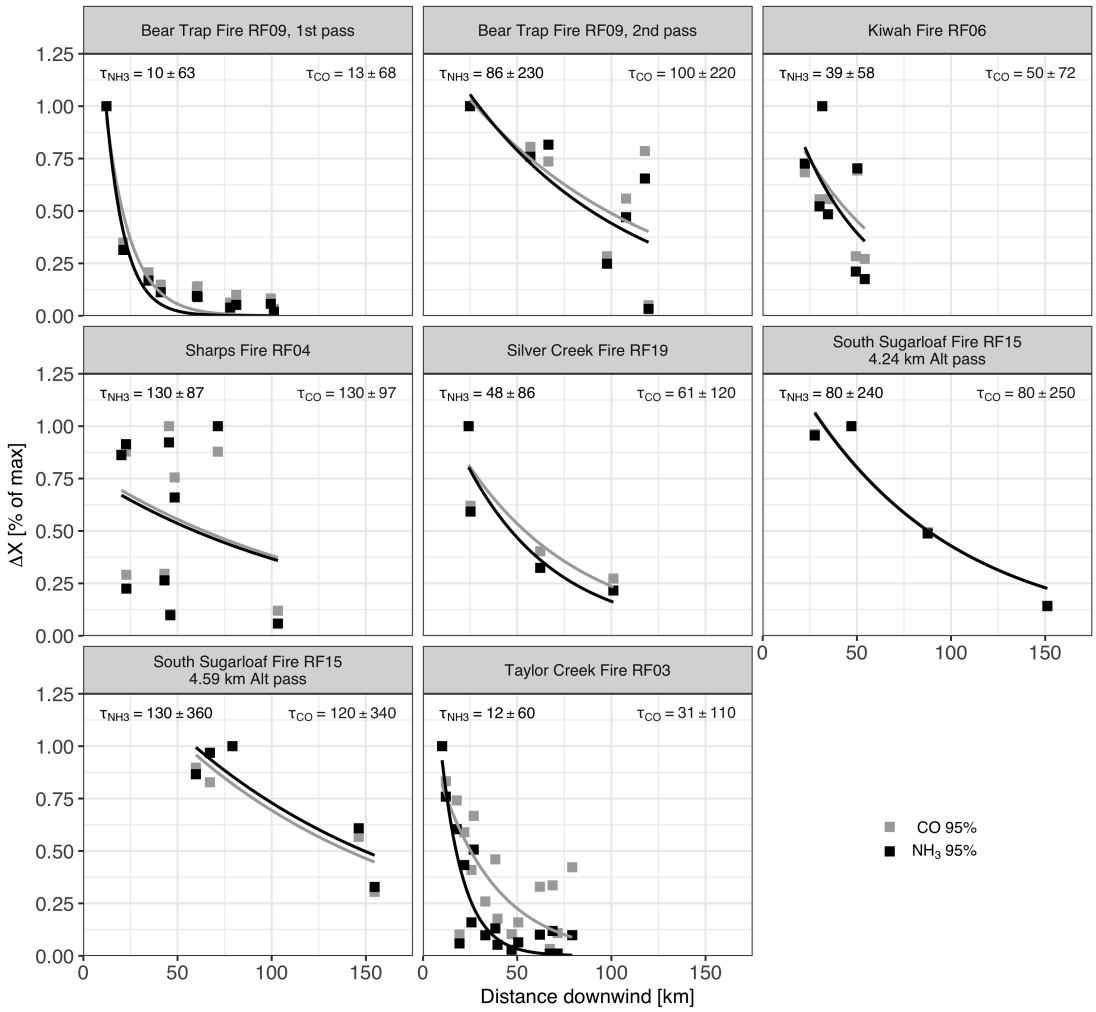

FIG. A15. Evolution of NH_3 and CO mixing ratios with estimated distance from the fire source. Plotted are the mean mixing ratios of NH_3 in black and CO in grey for each plume transect, minus the estimated background and normalized by the highest mixing ratio from all transects in that pseudo-Lagrangian sampling pattern (usually the youngest plume pass) against the distance downwind of the fire. τ_{NH3} and τ_{CO} represent the estimated e-folding loss distance with respect to dilution + chemical losses with 1σ standard deviation in kilometers, calculated for a first-order exponential decay to zero.

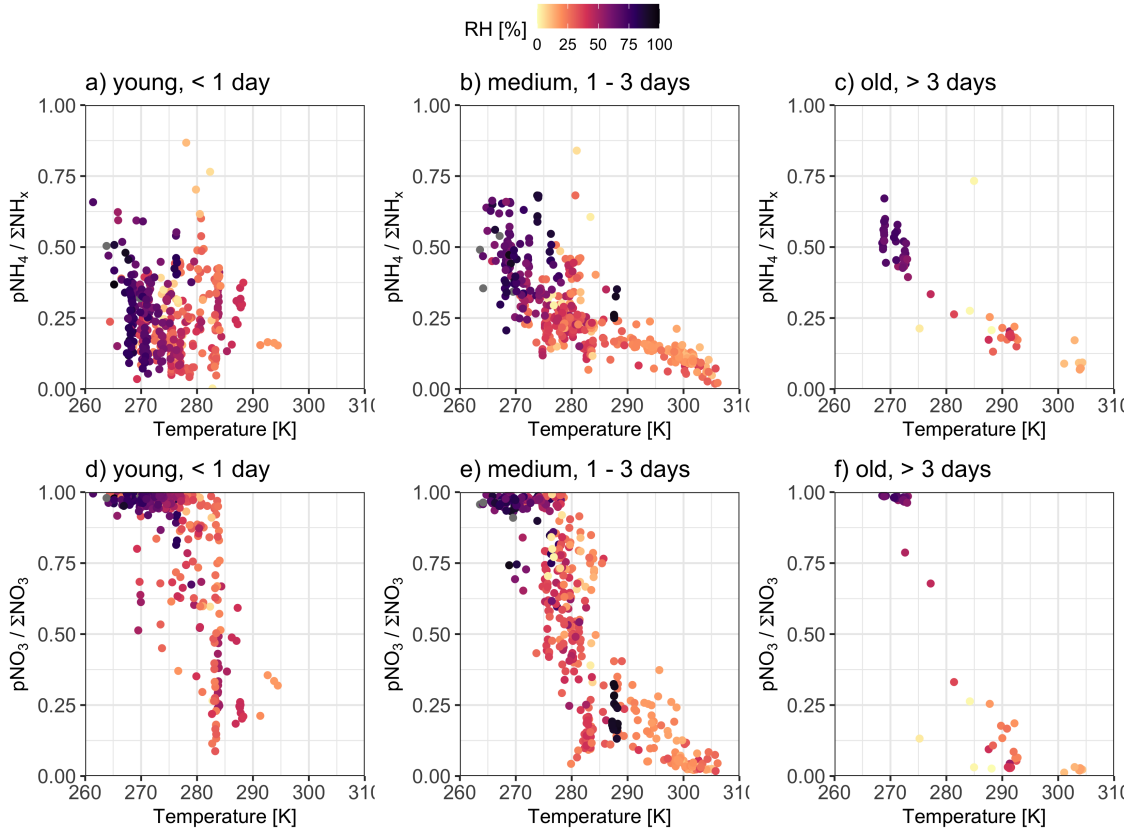

FIG. A16. (a-c) Measured $p\mathrm{NH}_4$ fraction ($p\mathrm{NH}_4/\Sigma\mathrm{NH}_x$) as a function of temperature, binned by young, medium, and old smoke, as defined by chemical age estimates from O'Dell et al. (in preparation). (d-f) Measured $p\mathrm{NO}_3$ fraction ($p\mathrm{NO}_3/\Sigma\mathrm{NO}_3$; $\Sigma\mathrm{NO}_3 = p\mathrm{NO}_3 + \mathrm{HNO}_3$) as a function of temperature, binned by the same chemical age estimates. Observations are averaged to the timebase of the TOGA instrument (approximately 30-second samples every 100 seconds) and colored by the observed relative humidity. Data points include only the observations collected > 2 km above sea level in order to limit ground-based emission influence, and are not background-corrected.

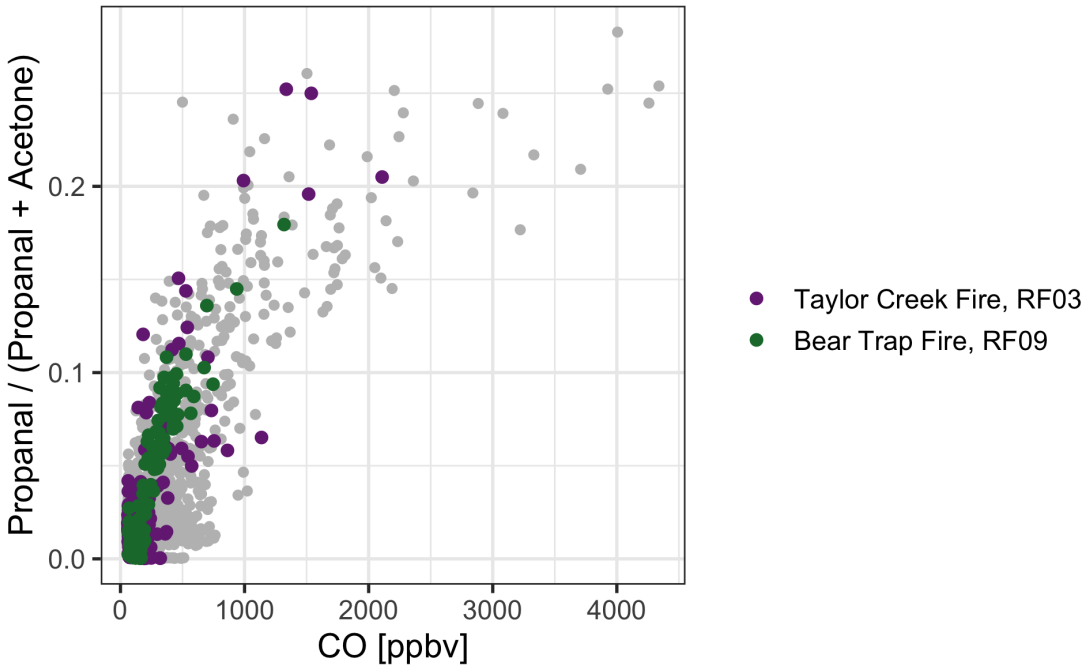

FIG. A17. Propanal fraction of the sum of individual propanal and acetone measurements by TOGA. All measurements in smoke are plotted in grey, and measurements from two fires, Taylor Creek and Bear Trap and colored purple and green respectively.